Training-to-Beat bioreactor for investigating Engineered Cardiac Tissues: design, development & validation

POLITECNICO DI TORINO

SCUOLA INTERPOLITECNICA DI DOTTORATO

Doctoral Program in Biomedical Engineering – XXVIII cycle

Final Dissertation

Training-to-Beat Bioreactor for Investigating Engineered Cardiac Tissues: Design, Development & Validation

Giuseppe Pisani

Tutor

prof. Cristina Bignardi
prof. Umberto Morbiducci
Dr. Diana Massai

Co-ordinator of the Research Doctorate Course

prof. Cristina Bignardi

April 4th, 2016

Abstract

In last the decades, advances relevant to the generation of 3D Engineered Cardiac Tissues (ECTs) have been made. In reason of this, ECTs are now considered a great promise for *in vitro* studies of cardiac development, disease and, eventually, for strategies for the repair of the structure and function of the injured myocardium.

Among the several physical stimuli which have been exploited to improve the functionality and maturation of ECTs, a preeminent role has been ascribed to mechanical stimulation. Appropriate mechanical stimulation can be recreated and maintained within bioreactors, which are devices/platforms devoted to mimic the physiological milieu in a monitored/controlled culture environment, where the engineered constructs can be properly stimulated.

One main limitation of the bioreactor-based strategy for cardiac tissue engineering applications is that the devices which are currently

used are meant to passively apply to ECTs a stimulus predefined by the user, regardless of their level of maturation along the duration of the *in vitro* culture.

In this scenario, and trying to overcome current limitations, a novel bioreactor design has been conceived for the investigation of 3D ECTs with a biomimetic approach. Technically, the here proposed bioreactor is capable (1) to apply native-like or pathologic mechanical stimuli (cyclic strain) by means of a reliable linear actuator operating in a wide range of strains and frequencies, and (2) to monitor in real-time both chemo-physical parameters (e.g. oxygen tension, pH) of the milieu and the mechanical stiffness of ECTs by means of dedicated sensors, eventually adapting the stimulation to the actual stage of maturation of the constructs.

As a proof of concept, a first experimental campaign has been carried out with a double aim: (1) to verify the bioreactor feasibility in delivering mechanical cyclical stimulation to 3D fibrin-based, ring shaped Engineered Cardiac Tissues (ECTs); (2) to assess the effect of cyclic strain on tissue maturation, contractility and modification on its mechanical properties.

In detail, the bioreactor platform has been preliminarily tested to verify protocols for hold on, sterilization, and control of the delivered mechanical stimuli. Firstly, the suitability of the bioreactor platform in culturing *ad-hoc* designed constructs, in terms of ease of use and capability in setting the stimulation parameters, has been tested. Then, the observed maturation of ring shaped ECTs subject to sinusoidal

cyclic strain within the bioreactor has confirmed the potency of the proposed approach and the instrumental role of mechanical stimulation in ECTs maturation and in the development of an adult-like cardiac phenotype responsive to electrical excitation.

Even if further validation steps are required before the implementation of culture strategy fully adaptive in terms of mechanical stimuli applied to the engineered cardiac constructs, the developed bioreactor represents a valuable proof of concept for, in its most advanced operational mode, biomimetic culturing of engineered cardiac constructs.

Contents

Chapter 1

Introduction

1.1 Clinical motivations and perspectives

Myocardial infarction (MI) and heart failure are the leading causes of mortality all over the world (Roger, et al. 2012). Cardiac function deteriorates along with the pathological progression of MI, and in the end stage, arrhythmias, mitral regurgitation, and heart failure can occur and become fatal (De Celle, et al. 2004, Cleutjens, Blankesteijn and J.F. 1999). At the state of the art, when we are in presence of a failing heart, the only effective therapy is still heart transplantation, which is limited by low supply of matching hearts for the constantly increasing number of patients. Ergo, it is imperative to dedicate efforts in developing effective methods for regenerating damaged myocardium (Parsa, Ronaldson and Vunjak-Novakovic 2016).

Among the novel approaches, cardiac repair has been exploited by means of stem cell therapy, and cardiac tissue engineering (TE) strategies (Alrefai, et al. 2015). Numerous clinical trials addressing the transplantation of various adult stem cell populations for cardiac regeneration have been performed in the last few years (Doppler, et al. 2013). It has been demonstrated that mobilization of endogenous stem cells or exogenous administration of a number of stem cell populations to injured tissues has resulted in structural regeneration of tissue as well as functional improvement (Baraniak and McDevitt 2010). Adult stem cell populations are selected on the base of their potential to proliferate, migrate and the ability to trans-differentiate into various mature cell types. Besides the direct trans-differentiation into cardiomyocytes, stem cells can also orchestrate different regenerative mechanisms such as the stimulation of resident endogenous myocardial stem cells and paracrine actions (Doppler, et al. 2013). However, significant drawbacks could weaken the potential of current stem cell therapeutic cardiac strategies. Some of the major limitations are related to the: (i) "true" regenerative potential of the various cell sources as well as clinical safety (Doppler, et al. 2013), (ii) low survival rate of the injected cells (Zhang, et al. 2001)and, (iii) low engraftment or wash out from the injection site (Reffelmann and Kloner 2003). Some authors suggested that functional engraftment and survival of transplanted cells might be overcome by tissue-engineering techniques (Doppler, et al. 2013).

In the past decades, cardiac TE has attracted significant interest because of the great promise of generating functional tissue constructs to be used as 3D models for *in vitro* studies of cardiac development and

disease and eventually for repairing the structure and function of injured myocardium (Wang, et al. 2013, Vunjak-Novakovic, Tandon, et al. 2010). Current cardiac TE methods take advantage from the endogenous capacity of (immature) cardiac cells to beat spontaneously and to form 3D functional syncytia (Moscona 1959, Kelm, et al. 2004) and use engineering techniques to make 3D constructs of different size and geometry. However, to capitalize the full biological potential of the cells, the *in vitro* systems need to recapitulate several aspects of the native tissue milieu (Vunjak-Novakovic, et al. 2014).

1.2 Significant highlights of the cardiac muscle

The contractile myocardium is a highly differentiated tissue, with a thickness of around ˜1 cm in humans and an asymmetrical and helical architecture (Akhyari, et al. 2008 , Vu and Kofidis 2012). Mainly, cardiac tissue is composed by tightly packed, elongated and rod shaped cardiomyocytes (CMs), together with fibroblasts (FBs), endothelial cells (ECs) and smooth muscle cells (SMCs). Contractile apparatus of CMs consists of sarcomeres arranged in parallel myofibrils highly metabolically active. A dense vasculature and extracellular matrix (ECM), rich of collagen and laminin, wraps and supports the cell network. When specialized pacemaker cells triggers the excitation, electrical signals propagate through a 3D syncytium formed by CMs. Mechanical stability during contraction and propagation of the signal is guaranteed by specialized junctions between cells, adherent and gap junctions. Excitation of CMs causes an increase in the amount of

cytoplasmic calcium, which triggers mechanical contraction and, as a result, pumps the blood forward (Odendra, et al. 2011).

As a whole, the heart can be considered as a dynamic electromechanical system where the myocardial tissue experiences mechanical stretch during diastole and produces active contraction during systole, in a metabolic demanding manner. The wide range of physical activities and pathological conditions which the myocardium is called to respond, requires high resilience, durability, mechanical efficiency and adaptiveness of its structures (Bouten, et al. 2011). In detail, within the left ventricle, along a normal cardiac cycle, pressure range between 10 and 120 mmHg while the volume change between 40 and 130 ml (Bouten, et al. 2011). Local mechanical loads can reach 50 kPa (Bouten, et al. 2011) with 22.9% and 59.2% longitudinal and radial systolic mean strains, respectively (Kuznetsova, et al. 2008). Young's modulus at end-diastole is reported to range between 200 and 500 KPa (Jawad, et al. 2007), while active contraction forces of myocardial strips isolated from native human ventricles are reported to range between 14.5 ± 4.4 and 22.8 ± 1.4 mN/mm^2 for healthy donors (Holubarsch, et al. 1998).

As regards to the electrical properties, signals of 1-2 ms in duration (Tandon, et al. 2009) excite the cardiac cells, at a resting rate of 1-1.7 Hz and propagate within the tissue (extracellular fluid conductivity, 3-12 mS/cm (Durand 2000)), inducing in the tissue an endogenous electrical field reported to be in the 0.1-10 V/cm interval (Tandon, et al. 2009).

1.3 Mimicking in vitro the native tissue formation

In vivo, the processes of cell differentiation during embryogenesis and adult tissue remodeling are orchestrated by cascades of regulatory factors interacting at multiple levels, in space and time. (Grayson, et al. 2009). Indeed, as first step, undifferentiated (stem) cells first differentiate into specific cell lineages (bone, muscle, nerves and blood vessels) and then undergo functional assembly into tissue structures (Grayson, et al. 2009). Mainly, four groups of factors have been identified to be instrumental for both phases: (i) a structural template for cell attachment and tissue formation, (ii) a physiological milieu, (iii) suitable levels of nutrients, oxygen and metabolites, and (iv) physical regulatory signals (Grayson, et al. 2009, Radisic, Park and Gerecht, et al. 2007).

According to this biomimetic approach, and given the structural and functional complexity of cardiac tissues, two fundamental requisites need to be satisfied for the production of organized and functional cardiac engineered constructs in vitro. Firstly a scaffold, i.e. an anchoring structure presenting native-like tissue mechanical properties and acting as a structural and logistic template for the cells should be used. Consequently, to address the maturation of the cultured construct in a mature-like phenotype, the most relevant physiologic conditions should be reestablished in terms of biophysical regulatory signals such as perfusion (Radisic, Marsano, et al. 2008), electrical (Tandon, et al. 2009) and mechanical stimulation (Fink, et al. 2000, Zimmermann, Schneiderbanger, et al. 2002, Birla, Huang and Dennis 2007).

A suitable dynamic environment is essential in replicating these physiological conditions, and can be recreated and maintained within bioreactors, specialized devices that attempt to mimic the physiological milieu monitoring and controlling the culture environment eventually stimulating the construct (Massai, et al. 2013). Indeed, a bioreactor is designed to perform one or more of the following tasks: (i) maintain efficient mass transfer between the cultured cells/constructs and the culture medium (e.g. temperature, pH, osmolality, levels of oxygen, nutrients, metabolites and regulatory molecules), (ii) establish spatially uniform, physiologically high cell concentration within the scaffold , and (iii) apply physical signals relevant for cardiac development and function (e.g. hydrodynamic shear, mechanical, electrical, or combined electromechanical stimuli) (Radisic, Park and Gerecht, et al. 2007).

It has been already shown, that the monitoring and controlling of the physicochemical environment in combination with the delivering of native-like physical stimuli eventually adapted to the tissue maturation, carried out with bioreactor-based platform, allow to obtain engineered constructs with improved morphological and functional properties (Carrier, et al. 1999, Korossis, et al. 2005, Bilodeau and Mantovani 2006). Furthermore, several studies have shown that the use of bioreactors as closed, standardized, and automated systems guarantees more reproducibility and lower contamination risk than the manual production processes as well as being sustainable both clinically and economically (Archer and Williams 2005, Pörtner, et al. 2005 , Martin, Smith and Wendt 2009, Olmer, et al. 2012).

1.4 Biomimetic approach to cardiac tissue engineering: scaffolds, biophysical stimulation and bioreactors

For an effective in vitro biomimetic tissue generation strategy, a synergistic combination of cells, scaffolds and culture conditions within tailored bioreactors is needed (Vunjak-Novakovic, Tandon, et al. 2010). The aim is to obtain cardiac engineered constructs, which are close to the native tissue in morphology and function, thus offering new perspectives to basic cardiac research and tissue replacement therapy. Among the different biophysical conditioning, herein we focus on the mechanical stimulation. Indeed, the heart starts functioning early in development and, thus, much of the growth and reorganization that occurs in utero is in the presence of changing mechanical stimuli. Furthermore, alterations in the cardiac function due to disease usually are correlated to alterations in the mechanical function of the organ, which alters the mechanical load on CMs. For these reasons, several studies have been addressed to assess the effects of various mechanical stimuli on CMs in vitro (Stoppel, Kaplan and Black 2016). Different typologies of scaffold and biophysical stimulations have been exploited so far (Massai, et al. 2013, Vunjak-Novakovic, Tandon, et al. 2010, Hirt, Hansen and Eshenhagen 2014), but a comprehensive review is beyond the scope if this introduction. However, a brief introduction on the scaffold being currently used is presented and an excursus of some main findings concerning the delivering of mechanical stimuli by means of bioreactors is reported.

1.4.1 Scaffolds

An ideal scaffold should mimic the native heart matrix properties, and actively interact with the cells at different scales: from "molecular", (incorporating ligands and growth factors) through "cellular" (migration, cell–cell contacts, and stiffness), to the tissue scale (Young Modulus) (Langer and Tirrell 2004, Lutolf and Hubbell 2005, Tibbitt and Anseth 2009). Furthermore, a tunable degradation of the material is essential to adapt the structural support of the scaffold with the developing tissue (Jockenhoevel and Flanagan, 2011). Among the several ways that have been followed, four main approaches stand out: (1) the use of prefabricated matrices, such as collagen and gelatine sponges (Li, et al. 1999, Radisic, Park and Shing, et al. 2004, Zhang, et al. 2015), (2) decellularized heart tissue (Ott, et al. 2008, Wang, et al. 2013), (3) cell sheets (Shimizu, et al. 2002, Matsuura, et al. 2013) and, (4) hydrogel techniques (Eschenhagen, et al. 1997 , Hansen, et al. 2010, Williams, et al. 2015) Regardless of the approach, the biomechanical properties of the employed scaffold should mimic the hierarchical structure and mechanical properties of the native heart matrix. That serves as informational template for regulating the cell-cell and cell-substrate interaction eventually addressing the cell behavior. Moreover, during culture, cells need to remodel the initial matrix gradually replacing it with its own matrix. Biomaterials used for scaffold production could include biological molecules (e.g., alginate, collagen, fibrin, and hyaluronan) and/or synthetic polymers (e.g., polylactic and polyglycolic acids and their copolymers, polycaprolactone), where a specific biomimetic architecture is approached to promote the differentiation and

functional organization of the seeded cells (Govoni, C., et al. 2013). Recently, fibrin (gel) is becoming largely used as scaffold candidate by virtue of its "physiological role" in tissue formation. Indeed a successful tissue engineering strategy should mimic the tissue regeneration process which is nearly related to haemostasis (Jockenhoevel and Flanagan, 2011). Numerous advantages have been highlighted for the use of fibrin. Starting with a compound of cells suspended within the fibrinogen solution, the fibrin gel scaffolds grant high seeding efficiency and homogenous cell distribution by gelation entrapment, eventually minimizing loss of cells. (Jockenhoevel, Zund, et al. 2001). Polymerization and degradation of the fibrin gel is manageable and can be tuned to the tissue development by using the protease inhibitors, such as aprotinin and tranexamic acid (Cholewinski, et al. 2009). The fibrin gel allows also to covalently embed grow factors and modulate their release (Wirz, et al. 2011). Noteworthy the compact cell-seeded structure that results from gelation provides an adequate hardiness for mechanical loading (Mol, et al. 2005).

Improved cardiac tissue structure and higher force development have been observed in fibrin based engineered constructs that were exposed to cyclic stretch by motorized stretching devices (Birla, Huang and Dennis 2007, Morgan and Black III 2014, Salazar, et al. 2015) or those cultured in auxotonic conditions (Hansen, et al. 2010).

1.4.2 Mechanical stimulation and bioreactors

Individually delivered or coupled mechanical and electrical conditioning have been identified as key treatments for biomimetic culture (Stoppel, Kaplan and Black 2016). Investigations carried out in the last decade shown their crucial role during cardiac development, in supporting cell differentiation and self-assembling and for further cardiomyocyte maturation, promoting the overall structure organization and, thus, the functionality of the engineered constructs. (Eschenhagen, et al. 1997 , Zimmermann, Schneiderbanger, et al. 2002, Isenberg and Tranquillo 2003, Radisic, Park and Shing, et al. 2004, Feng, et al. 2005 , Zimmermann, et al. 2006, Wang, et al. 2013, Morgan and Black III 2014, Godier-Furnémont, et al. 2015.) Dealing with the mechanical stimulation, different load conditions on engineered cardiac constructs have been investigated so far. To simulate isometric contraction, the static load condition has been for first approached showing to have influence in the tissue organization and contractile activity under pacing (Eschenhagen, et al. 1997). Subsequently, the phasic stretching (quasi-isotonic contraction), as alternative load mode, has been exploited by means of commercial or custom-made motorized devices within a range of strain of 10-20% and a range of frequencies of 1-2Hz. If compared with static controls, constructs that were exposed to phasic stretch by motorized stretching devices showed: (i) improved tissue maturation and enhanced expression of junctional proteins as well as matrix fiber reorganization (Fink, et al. 2000 , Zimmermann, Schneiderbanger, et al. 2002, Feng, et al. 2005 , Kensah, et al. 2011, Salazar, et al. 2015, Morgan and Black III 2014) and, (ii) increase in the active, systolic force (also

referred to as twitch tension [TT]) and recapitulation of the Frank-Starling mechanism (Zimmermann, Schneiderbanger, et al. 2002, Tulloch, et al. 2011). A third way to load the engineered tissues was suspending them between resilient mounts to facilitate the so-called auxotonic contraction. This flexible loading approach seems to resemble the physiologic contraction cycle quite closely and showed to improve the tissue maturation as well as the systolic force (Zimmermann, et al. 2006, Hansen, et al. 2010, Schaaf, et al. 2014). However, its application is weaken by the fact that, as far as the constructs develop their contractile properties, a variable load against which to exert contraction should be tuned consequently (W. Zimmermann, 2013).

From the very first simple stretching devices, used to delivered uniaxial stimulation (Fink, et al. 2000 , Zimmermann, Schneiderbanger, et al. 2002), the engineering design of the bioreactors has been improved, initially, ameliorating the instrumentation to control the stimulation protocols and making them compatible with several tissue constructs (Birla, Huang and Dennis 2007). Furthermore, some stretching devices started to integrate the electrical stimulation to deliver combined stimulation patterns (Stoppel, Kaplan and Black 2016, Wang, et al. 2013). Nevertheless, to assess the effects of mechanical stretch, neo constructs needed still to be transferred within a measurement device (e.g. a standard test instrument or an organ bath chamber), making force measurement (active and passive) predominantly used as end-point analysis (Kensah, et al. 2011). In 2011, Kensah and coworkers developed a bioreactor-based platform, incorporating mechanical stimulation and direct real-time contraction force measurement (Kensah, et al. 2011).

The device was also designed for including additional functions, such as electric pacing and culture medium perfusion and the possibility of (fluorescence) microscopic assessment during continuous cultivation (Kensah, et al. 2011). Following this configuration, a number of distinct bioreactors have been devised to incorporate one or more of the mentioned stimulations or the assessment of physical characteristics (Govoni, Lotti, et al. 2014, Salazar, et al. 2015). Yet, even if widely recognized that the engineering design of the bioreactors should permit to recapitulate as close as possible the physiological stimuli experienced in vivo, the ideal culture platform is still at the horizon (Liaw and Zimmermann 2016, Salazar, et al. 2015). Indeed, bioreactors for culturing engineered cardiac tissues have been limited by several factors:

- the mechanical stimulation pattern is limited in terms of waveforms, frequency and duty cycle duration, bounding the possibility to mimic the wide range of conditions experienced by the heart tissue in vivo (Birla, Huang and Dennis 2007)
- measurement of mechanical properties of tissue engineered constructs typically require interruption of the cultivation process and therefore provide only end-point measurements of the respective samples (Fink, et al. 2000)
- physical and functional properties (e.g. mechanical stiffness, active force) of engineered constructs (Kensah, et al. 2011) are never monitored in combination with physicochemical parameters

- systems are not able to adapt the stimulation to the actual maturation stage of the construct; strain/load cannot be adjusted on the basis of the measured force exerted by the construct (W. Zimmermann, 2013)

1.5 Research outline

In order to overcome some limitation of the bioreactors currently used in the generation and characterization of thick-relevant engineered cardiac tissues, the design and the development of a novel advanced bioreactor is proposed in this work.

In its most advanced operational mode, the bioreactor is capable to: (i) apply native-like or pathologic stimuli (cyclic strain) (ii) monitor in real-time both the milieu parameters (e.g. oxygen tension, pH) and the developing mechanical stiffness of mm-scale engineered cardiac tissues. Towards the final validation of the bioreactor performances, the effects of the cyclic strain imparted by the device on cardiac tissue models has been assessed by the development of on-purpose fibrin-based engineered cardiac tissues, characterized by a novel mixture composition devised for this application. In detail, chapters are organized as follow.

Chapter II – Design and implementation of a cyclic strain-based bioreactor to train engineered cardiac tissues.

In this chapter, the engineering design and the development of a novel advanced bioreactor is illustrated. The system has been developed to deliver native-like or pathologic stimuli (cyclic strain) to engineered cardiac constructs in a wide range of strains and frequencies by means

of a reliable linear actuator. The bioreactor is also equipped with a system of sensors to monitor in real-time the evolution of (1) the culture parameters, related to the metabolic behavior of the tissues, and (2) the physical response of the mechanically stimulated constructs along the culture in a non-destructive manner. Finally, a monitoring and control unit oversees the mechanical stimulation and the acquisition of the signals from the sensors, allowing the communications from and toward the user thanks to a dedicated purpose-built software. The architectural design and the constitutive mechanical, electronic and software subsystems are presented in detail. A preliminary validation in house is reported.

Chapter III - Effects of cyclic strain on maturation, contractility and mechanical properties of Engineered Cardiac Tissues. A proof of concept.

In this chapter, fibrin-based, ring shaped Engineered Cardiac Tissues were generated and cultured within the bioreactor. The effects of cyclic strain on the maturation, alignment, modification of the extracellular matrix and on the elastic and functional properties of ECTs was evaluated by means of histologic assessments, mechanical testing and response to external electrical pacing along the culture.

Chapter IV - Conclusions and Future Perspectives.

In this chapter, concluding observations of each section are summarized. Suggestions on future perspectives based on the obtained results and ongoing assessments are provided.

References

Akhyari, P., Kamiya, H., A. Haverich, M. Karck, and A. Lichtenberg. "Myocardial tissue engineering: the extracellular matrix." *Eur J Cardiothorac Surg* 34, no. 2 (2008): 229-41.

Alrefai, M.T., D. Murali, Paul A., K.M. Ridwan, J.M. Connell, and Shum-Tim D. "Cardiac tissue engineering and regeneration using cell-based therapy." *Stem Cells Cloning*, 2015: 81–101.

Archer, R., and D.J. Williams. "Why tissue engineering needs process engineering." *Nature Biotechnology* 11, no. 23 (2005): 1353-1355.

Baraniak, P.R., and T.C. McDevitt. "Stem cell paracrine actions and tissue regeneration." *Regen Med* 5, no. 1 (2010): 121–143.

Bilodeau, K., and D. Mantovani. "Bioreactors for tissue engineering: focus on mechanical constraints. A comparative review." *Tissue Engineering* 12, no. 8 (2006): 2367-2383.

Birla, R.K., Y.C. Huang, and R.G. Dennis. "Development of a novel bioreactor for the mechanical loading of tissue-engineered heart muscle." *Tissue Engineering* 13, no. 9 (2007): 2239-48.

Bouten, C.V., P.Y. Dankers, A. Driessen-Mol, S. Pedron, and A.M.: Baaijens, F.P. Brizard. "Substrates for cardiovascular tissue engineering." *Adv Drug Deliv Rev* 63, no. 4-5 (2011): 221-41.

Carrier, R.L., et al. "Cardiac tissue engineering: cell seeding, cultivation parameters, and tissue construct characterization." *Biotechnol Bioeng* 64, no. 5 (1999): 580-9.

Cholewinski, E., M. Dietrich, T. C. Flanagan, T. Schmitz-Rode, and S. Jockenhoevel. "Tranexamic acid- an alternative to aprotinin in fibrin-based cardiovascular tissue engineering." *Tissue Engineering Part A*, 2009.

Cleutjens, J.P., W.M. Daemen M.J. Blankesteijn, and Smits J.F. "The infarcted myocardium: simply dead tissue, or a lively target for therapeutic interventions." *Cardiovasc Res* 44, no. 2 (1999): 232-41.

De Celle, T., J.P. Cleutjens, W.M. Blankesteijn, J.J. Debets, J.F. Smits, and B.J. Janssen. "Long-term structural and functional consequences of cardiac ischaemia-reperfusion injury in vivo in mice." *Exp Physiol* 89, no. 5 (2004): 605-15.

Doppler, S.A., M-A. Deutsch, R. Lange, and M. Krane. "Cardiac regeneration: current therapies—future concepts." *J Thorac Dis*, no. 5 (2013): 683–697.

Durand, D. M. "Electric Stimulation of Excitable Tissue." Chap. 17 in *The Biomedical Engineering Handbook*. Joseph D. Bronzino, 2000.

Eschenhagen, T., et al. "Three-dimensional reconstitution of embryonic cardiomyocytes in a collagen matrix: a new heart muscle model system." *FASEB J* 11, no. 8 (1997): 683-94.

Feng, Z., T. Matsumoto, Y. Nomura, and T. Nakamura. "An electro-tensile bioreactor for 3-D culturing of cardiomyocytes - a bioreactor system that simulates the myocardium's electrical and mechanical response in vivo." *IEEE Eng Med Biol* 24, no. 4 (2005): 73-9.

Fink, C., S. Ergün, D. Kralisch, U. Remmers, J. Weil, and T. Eschenhagen. "Chronic stretch of engineered heart tissue induces hypertrophy and functional improvement." *FASEB J* 14, no. 5 (2000): 669-79.

Godier-Furnémont, A.F., et al. "Physiologic force-frequency response in engineered heart muscle by electromechanical stimulation." *Biomaterials* 60 (2015.): 82-91.

Govoni, M., et al. "An innovative stand-alone bioreactor for the highly reproducible transfer of cyclic mechanical stretch to stem cells cultured in a 3D scaffold." *J Tissue Eng Regen Med* 8, no. 10 (2014): 787-93.

Govoni, M., Muscari C., C. Guarnieri, and E. Giordano. "Mechanostimulation Protocols for Cardiac Tissue Engineering." 2013.

Grayson, W.L., T.P. Martens, G.M. Eng, M. Radisic, and G. Vunjak-Novakovic. "Biomimetic Approach to Tissue Engineering." *Semin Cell Dev Biol* 20, no. 6 (2009): 665–673.

Hansen, A., et al. "Development of a drug screening platform based on engineered heart tissue." *Circ Res* 107, no. 1 (2010): 35-44.

Hirt, M.N., A. Hansen, and T. Eshenhagen. "Cardiac Tissue Engineering: State of the Art." *Circulation Research* 114, no. 2 (2014): 354-67.

Holubarsch, C., et al. "Shortening versus isometric contractions in isolated human failing and non-failing left ventricular myocardium: dependency of external work and force on muscle length, heart rate and inotropic stimulation." *Cardiovasc Res* 37, no. 1 (1998): 46-57.

Isenberg, B.C., and R.T. Tranquillo. "Long-term cyclic distention enhances the mechanical properties of collagen-based media-equivalents." *Ann Biomed Eng* 31, no. 8 (2003): 937-49.

Jawad, H., N.N. Ali, A.R. Lyon, Q.Z. Chen, S.E. Harding, e A.R. Boccaccini. «Myocardial tissue engineering: a review.¸ *J Tissue Eng Regen Med* 1, n. 5 (2007): 327-42.

Jockenhoevel, S., and T.C. Flanagan. "Cardiovascular Tissue Engineering Based on Fibrin-Gel-Scaffolds." In *Tissue Engineering for Tissue and Organ Regeneration*. Daniel Eberli, 2011.

Jockenhoevel, S., et al. "Fibrin gel-advantages of a new scaffold in cardiovascular tissue engineering." *Eur J Cardiothorac Surg* 19, no. 4 (2001): 424-30.

Kelm, J.M., E. Ehler, L.K. Nielsen, S. Schlatter, J.C. Perriard, and M. Fussenegger. "Design of artificial myocardial microtissues." *Tissue Eng* 10, no. 1-2 (2004): 201-14.

Kensah, G., et al. "A novel miniaturized multimodal bioreactor for continuous in situ assessment of bioartificial cardiac tissue during stimulation and maturation." *Tissue Eng Part C* 17, no. 4 (2011): 463-73.

Korossis, SA., F. Bolland, JN. Kearney, J. Fisher, and E. Ingham. *Bioreactors in Tissue Engineering.* Vol. 2, in *Topics in Tissue Engineering*. N. Ashammakhi & R.L. Reis, 2005.

Kuznetsova, T., et al. "Left ventricular strain and strain rate in a general population." *Eur Heart J* 29, no. 16 (2008): 2014-23.

Langer, R., and D.A. Tirrell. "Designing materials for biology and medicine." *Nature* 428 (2004): 487-492.

Li, R.K., Z.Q. Jia, R.D. Weisel, D.A. Mickle, A. Choi, and T.M. Yau. "Survival and Function of Bioengineered Cardiac Grafts." *Circulation* 100, no. II (1999): II63-II69.

Liaw, N.Y., and W.H. Zimmermann. "Mechanical stimulation in the engineering of heart muscle." *Adv Drug Deliv Rev.*, 2016.

Lu, L., et al. "Design and validation of a bioreactor for simulating the cardiac niche: a system incorporating cyclic stretch, electrical stimulation, and constant perfusion." *Tissue Eng Part A* 19, no. 3-4 (2013): 403-14.

Lutolf, M.P., and J.A. Hubbell. "Synthetic biomaterials as instructive extracellular microenvironments for morphogenesis in tissue engineering." *Nat Biotechnol* 23, no. 1 (2005): 47-55.

Martin, I., T. Smith, and D. Wendt. "Bioreactor-based roadmap for the translation of tissue engineering strategies into clinical products." *Trends Biotechnol* 27, no. 9 (2009): 495-502.

Massai, D., et al. "Bioreactors as engineering support to treat cardiac muscle and vascular disease." *Journal of Healthcare Engineering* 3, no. 4 (2013): 329-70.

Matsuura, K., Y. Haraguchi, T. Shimizu, and T. Okano. "Cell sheet transplantation for heart tissue repair." *J Control Release* 169, no. 3 (2013).

Mol, A., et al. "Fibrin as a cell carrier in cardiovascular tissue engineering applications." *Biomaterials* 26, no. 16 (2005): 3113-21.

Morgan, K.Y., and L.D. Black III. *Creation of Bioreactor for the Apllication of Variable Amplitude Mechanical Stimulation of Fibrin Gel-Based Engineered Cardiac Tissue.* Vol. 1181, in *Cardiac Tissue Engineering: Methods and Protocols, Methods in Molecular Biology*. Milica Radisic and Lauren D. Black III, 2014.

Moscona, A.A. "Tissues from dissociated cells." *Sci Am* 200 (1959): 132-134.

Odendra, D., L. Chiu, L. Reis, F. Rask, K. Chiang, and M. Radisic. "Biomaterials for Tissue Engineering Applications. A review of the Past and Future Trends." Chap. 15 in *Cardiac Tissue Engineering*. Burdick, JA; Mauck, RL, 2011.

Olmer, R., et al. "Suspension culture of human pluripotent stem cells in controlled, stirred bioreactors." *Tissue Eng Part C Methods* 18, no. 10 (2012): 772-84.

Ott, H.C., et al. «Perfusion-decellularized matrix: using nature's platform to engineer a bioartificial heart.¸ *Nature Medicine* 14 (2008): 213 - 221.

Parsa, H, K. Ronaldson, and G. Vunjak-Novakovic. "Bioengineering methods for myocardial regeneration." *Adv Drug Deliv Rev* 96 (2016): 195-202.

Pörtner, R., S. Nagel-Heyer, C. Goepfert, P. Adamietz, and N.M. Meenen. "Bioreactor design for tissue engineering." *J Biosci Bioeng* 100, no. 3 (2005): 235-45.

Radisic, M., A. Marsano, R. Maidhof, Y. Wang, and G. Vunjak-Novakovic. "Cardiac tissue engineering using perfusion bioreactor systems." *Nat Protoc* 3, no. 4 (2008): 719-38.

Radisic, M., et al. "Functional assembly of engineered myocardium by electrical stimulation of cardiac myocytes cultured on scaffolds." *PNAS* 101, no. 52 (2004): 18129–18134.

Radisic, M., H. Park, S. Gerecht, C. Cannizzaro, R. Langer, and G. Vunjak-Novakovic. "Biomimetic approach to cardiac tissue engineering." *Philos Trans R Soc Lond B Biol Sci* 362, no. 1484 (2007): 1357–1368.

Reffelmann, T., and R.A. Kloner. "Cellular cardiomyoplasty-cardiomyocytes, skeletal myoblasts, or stem cells for regenerating myocardium and treatment of heart failure?" *Cardiovasc Res* 58, no. 2 (2003): 358-68.

Roger, V.L., et al. "Heart disease and stroke statistics--2012 update: a report from the American Heart Association." *Circulation* 125, no. 1 (2012).

Salazar, B.H., A.T. Cashion, R.G. Dennis, and R.K. Birla. "Development of a Cyclic Strain Bioreactor for Mechanical Enhancement and Assessment of Bioengineered Myocardial Constructs." *Cardiovasc Eng Technol.* 6, no. 4 (2015): 533-45.

Schaaf, S., A. Eder, I. Vollert, A. Stohr, A. Hansen, and T. Eschenhagen. *Generation of Strip-Format Fibrin-BAsed Engineered Heart Tissue (EHT).* Vol. 1181, in *Cardiac Tissue Engineering: Methods and Protocols, Methods in Molecular Biology*. Milica Radisic and Lauren D. Black III, 2014.

Shimizu, T., et al. "Fabrication of pulsatile cardiac tissue grafts using a novel 3-dimensional cell sheet manipulation technique and temperature-responsive cell culture surfaces." *Circ Res* 90, no. 3 (2002): e40.

Stoppel, W.L., D.L. Kaplan, and L.D.III Black. "Electrical and mechanical stimulation of cardiac cells and tissue constructs." *Adv Drug Deliv Rev*, 2016: 135-55.

Tandon, N., et al. "Electrical stimulation systems for cardiac tissue engineering." *Nat Protoc* 4, no. 2 (2009): 155-73.

Tibbitt, M.W., and K.S. Anseth. "Hydrogels as extracellular matrix mimics for 3D cell culture." *Biotechnol Bioeng* 103, no. 4 (2009): 655-63.

Tulloch, N.L., et al. "Growth of engineered human myocardium with mechanical loading and vascular coculture." *Circ Res* 109, no. 1 (2011): 47-59.

Vu, D.T., and T. Kofidis. "Myocardial Restoration: Is It the Cell or the Architecture or Both?" *Cardiology Research and Practice*, 2012.

Vunjak-Novakovic, G., et al. "Challenges in cardiac tissue engineering." *Tissue Eng Part B* 16, no. 2 (2010): 169-87.

Vunjak-Novakovic, G., T. Eschenhagen, and C. Mummery. "Myocardial Tissue Engineering: In Vitro Models." *Cold Spring Harb Perspect Med*, 2014.

Wang, B., et al. "Myocardial scaffold-based cardiac tissue engineering: application of coordinated mechanical and electrical stimulations." *Langmuir* 29, no. 35 (2013): 11109-17.

Williams, C., et al. "Cardiac extracellular matrix-fibrin hybrid scaffolds with tunable properties for cardiovascular tissue engineering." *Acta Biomater*, 2015: 84-95 .

Wirz, S., et al. "Influence of platelet-derived growth factor-AB on tissue development in autologous platelet-rich plasma gels." *Tissue Eng Part A.* 17, no. 13-14 (2011): 1891-9.

Zhang, B., M. Montgomery, L. Davenport-Huyer, A. Korolj, and M. Radisic. "Platform technology for scalable assembly of instantaneously functional mosaic tissues." *Sci Adv* 1, no. 7 (2015).

Zhang, M., D. Methot, V. Poppa, Y. Fujio, K. Walsh, and C.E. Murry. "Cardiomyocyte grafting for cardiac repair: graft cell death and anti-death strategies." *J Mol Cell Cardiol* 33, no. 5 (2001): 907-21.

Zimmermann, W., et al. «Engineered heart tissue grafts improve systolic and diastolic function in infarcted rat hearts.¸ *Nat Med* 12 (2006): 452–458.

Zimmermann, W.H. "Biomechanical regulation of in vitro cardiogenesis for tissue-engineered heart repair." *Stem Cell Research & Therapy* 4, no. 137 (2013).

Zimmermann, W.H., et al. «Tissue engineering of a differentiated cardiac muscle construct.¸ *Circ Res* 90 (2002): 223–230 .

Chapter 2

Design and implementation of a cyclic strain-based bioreactor to train engineered cardiac tissues

2.1 Introduction

Due to the structural and functional complexity of cardiac tissue, successful strategies of cardiac tissue engineering (TE) for the in vitro generation of functional engineered cardiac tissues to be used as substitutes or models for drug screening require in-depth investigations on cardiac tissue developmental aspects and adequate biochemical and biophysical stimulations during culture (Bilodeau and Mantovani 2006, Vunjak-Novakovic, et al. 2010).

As mentioned in the first chapter, a suitable dynamic culture environment is essential in replicating the physiological conditions in vitro. This can be achieved by the use of bioreactors, specialized devices

that attempt to mimic the physiological milieu by monitoring and controlling the culture environment and eventually stimulating the construct (Massai et al., 2013). Indeed, a bioreactor is designed to perform one or more of the following tasks: (i) maintain efficient mass transfer between the cultured cells/constructs and the culture medium (e.g. temperature, pH, osmolality, levels of oxygen, nutrients, metabolites and regulatory molecules), (ii) guarantee spatially uniform, physiologically high cell concentration within the constructs, and (iii) apply physical signals relevant for the development and function of the engineered tissue (e.g. hydrodynamic shear, mechanical, electrical, or combined electromechanical stimuli) (Radisic, et al. 2007).

The monitoring and controlling of the physicochemical environment, in combination with the delivering of native-like physical stimuli carried out with bioreactor-based platform, allows to obtain engineered constructs with improved morphological and functional properties (Carrier, et al. 1999, Korossis, et al. 2005, Bilodeau and Mantovani 2006). In particular, mechanical stimulation has been shown to be crucial during cardiac development, supporting cell differentiation and self-assembling, and for further cardiomyocyte maturation, guiding the overall structure organization and, thus, the functionality of the engineered cardiac constructs (Kensah, et al. 2011, Hirt, Hansen and Eshenhagen 2014). It has been also highlighted the importance in monitoring the evolution of tissue maturation in order to adequately train the neo-tissue (Zimmermann, 2013). In order to overcome some limitations of the bioreactors currently used in the generation and mechanical conditioning of mm-scale cardiac tissue, a novel advanced

bioreactor-based platform is herein proposed. In this chapter, the engineering design and the development of the bioreactor components are presented. The device is proposed as a system meant to deliver native-like or pathologic stimuli (cyclic strain) to engineered cardiac constructs in a wide range of strains and frequencies by means of a reliable linear actuator. The bioreactor is also equipped with a system of sensors to monitor in real-time the evolution of (1) the culture parameters, related to the metabolic behavior of the tissues, and, (2) the physical response of the mechanically stimulated constructs during the culture in a non-destructive manner. Finally, a monitoring and control unit oversees both the mechanical stimulation and the acquisition of the signals from the sensors, allowing the communications from and toward the user thanks to a dedicated purpose-built software. Furthermore, the adopted technical solutions, in terms of hardware and software architecture, allow for an expansion of the device functionalities.

2.2 Bioreactor description

2.2.1 Device requirements

As the bioreactor was designed to work into a standard incubator, all the materials employed in its design and fabrication were chosen accordingly. Furthermore, to assure full compatibility with good manufacturing practice (GMP) standards, few general principles, generally considered the "basics", were used as a blueprint for the design (Partap, Plunkett and O'Brien 2004, Mantero, et al. 2007). Table 1 summarizes these key points.

Table 1 General requirements

General Requirements	Description
Simplicity in the design	It should be quick to assemble and disassemble
Compactness in size	It should fit in a standard size incubator
Cytocompatibility and corrosion-resistance	The materials in contact with culture medium/cells must be inert, while the materials used for external parts must be usable at 37 ° C in humid atmosphere
Facilitate monitoring of cell/tissue quality	The culture chamber in should be in translucent material
Ability to ensure the culture of tissue samples under sterile conditions	The sealing of the moving parts is crucial and must be carefully taken into account
Ease of sterilization and sterility maintenance	It should be possible to sterilize by autoclaving or other methods (resistance of the material at T ≥ 120 ° C for at least 1h)
Ease of use	It should be easy to fix the cells/scaffold in place in sterile conditions under a laminar flow hood –simple to use also for non-trained staff
Possibility of housing a experimentally significant number of specimens	A minimum of three samples should be cultured for each experiment
Scalability	The design should be relatively easy to enlarge without changing its characteristics

In detail, the bioreactor design was driven by four main requirements:

- to apply accurate, controllable and user-defined displacement (namely cyclic strain) in the range of (i) 5 - 100% of strain for ring shaped/strip-like constructs 2-15 mm in length and, (ii) 1-6 Hz of frequency.

- to acquire, in real-time, culture bulk parameters: (i) dissolved oxygen tension (range 0-21%) and, (ii) pH (0-11 pH).[1]
- to measure, in real-time, the force exerted by the cardiac engineered tissue and assess changings in the construct mechanical properties along the culture (forces in the range 0-10N).
- to allow the user in (1) setting the culture condition in terms of strain and waveform, (2) calibrate, display in real-time/save the signals form the sensors and (3) run tests for the mechanical characterization (as in a standard commercial Testing System) of the tissues, by means of a software user friendly interface.

2.2.2 Architectural design and constitutive elements

The architecture of the bioreactor is depicted in Figure 1 and a description of the components in Figure 2. To confer the maximum modularity, the bioreactor has been designed to be composed by four main components: (1) a culture unit, (2) a structural framework, (3) a stimulation and sensing unit and (4) a monitoring and control unit.

The **culture unit** contains and holds the constructs surrounded by the culture medium; the lid of the culture chamber seals and is capable to accommodate up to four immersed sensors.

[1] Acquisition of CO_2 and temperature parameters were also considered as extension of the current design

The **structural framework** is the external chassis which anchors the mutual position of all the components of the bioreactor and allows the actuator to deliver the mechanical stimulus to the 3D construct on one side of the culture unit, while monitoring the force exerted by means of a load cell on the contralateral extremity.

The **stimulation and sensing unit** comprises two distinct subunits. The **stimulation unit** is composed by the linear actuator and the position transducer. Indeed, in the design of the actuation system the use of the motor which have been selected, requires the implementation of a feedback loop control strategy and hence the presence of a position transducer. The **sensing unit** is composed by the pH, O_2 sensors and the force sensor.

Finally, the **monitoring and control unit** oversees (i) the feedback loop motion control strategy, (ii) the acquisition of the signals from the sensors and, (iii) the communications from and toward the user, using a real-time structure. It is composed by software and hardware components, i.e. a real-time controller, an analog input module and a power module, which are boxed in a case and a PC. In Figure 2 a picture of the actual device is shown.

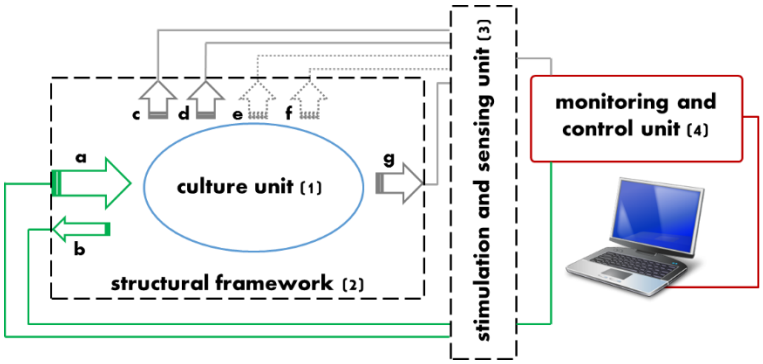

Figure 1: Architecture of the bioreactor and its four main components: culture unit (1), structural framework (2), stimulation and sensing unit (3), monitoring and control unit (4). With regard to the stimulation and sensing unit: green lines indicate the stimulation components which embed: the linear actuator (a) and the position transducer (b) while grey lines indicate the sensing components, i.e., pH (c), O_2 (d) sensors or currently unused spots for two more sensors (e.g. CO_2 and temperature(e, f)) and load cell (g).

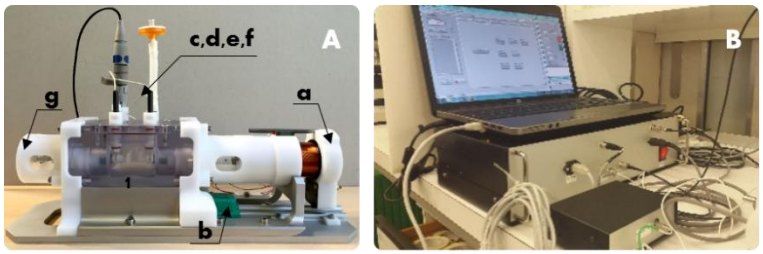

Figure 2: Figure A shows the culture unit(1) assembled within the structural framework (2) and the components of the stimulation and sensing unit(3), i.e linear actuator (a), position transducer (b) and the pH, O_2 and load cell sensors (c,d,g). Figure B shows the (4) monitoring and control unit

The mechanical design has been carried out by means of SolidWorks® (Dassault Systemes, FR). The NI (National Instruments, TX, USA) hardware and the LabView® Graphical Programming Environment

software (National Instruments, TX, USA) were considered the most appropriate choice for the fulfilment of the project requisites.

2.2.3 Culture unit design

The components herein described compose the so called **culture unit.** They enter directly in contact with the constructs and the culture medium. Consequently, this is the solely unit which the components undergo to the sterilization process.

The culture chamber is a transparent autoclavable rectangular vessel (140 x 80 x 75 mm^3 with a priming volume of ˜100 ml). The internal geometry is symmetrical and presents two lateral holes 40 mm in diameter along the longitudinal section which merge into a quadrangular central well (where the constructs are placed) opened in the upper part where the lid seats (Figure 3C). All the internal edges are rounded in order to avoid stagnation points or discontinuities, fissures, interstices, holes, which are preferable targets for microbial contamination. It has been made out of Polycarbonate (PC) which is a strong, tough and optically transparent thermoplastic polymer. Besides, many polycarbonate grades are used in medical applications and can be sterilized using steam at 120 ° C, gamma radiation, or by the ethylene oxide (EtO) method.

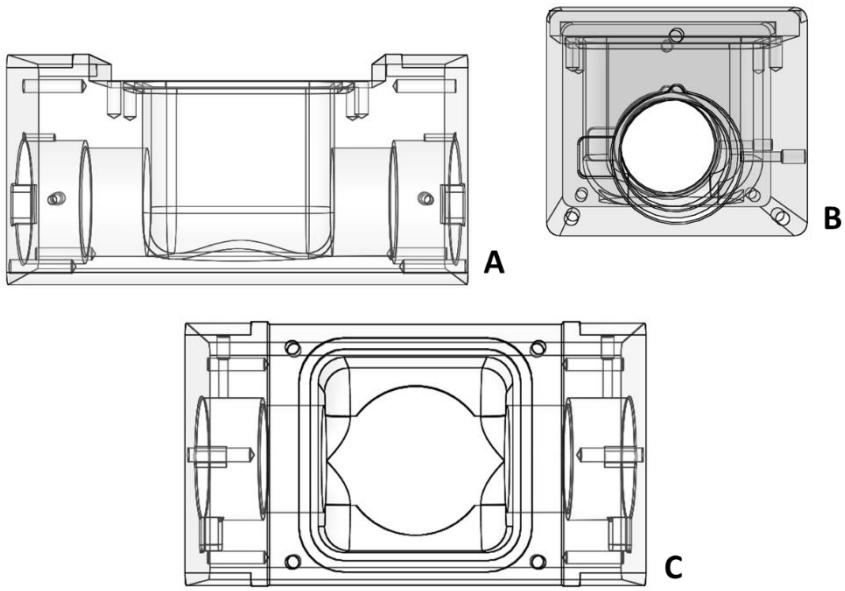

Figure 3: Culture chamber views: (A) longitudinal (B) cross, and (C) top view

Two lateral cylindrical walls (left and right wall) fit into the lateral holes of the chamber with the double function of (1) allowing the shaft, where the constructs are hold by the grasping system, to smoothly shift and deliver the motion, (2) sealing the chamber from the external by means of silicon bellows (Figure 4). It is functional to label one side of the culture unit as the *actuation side*, where the shaft couples the actuator, and the contralateral as the *sensing side*, where it couples the force sensor.

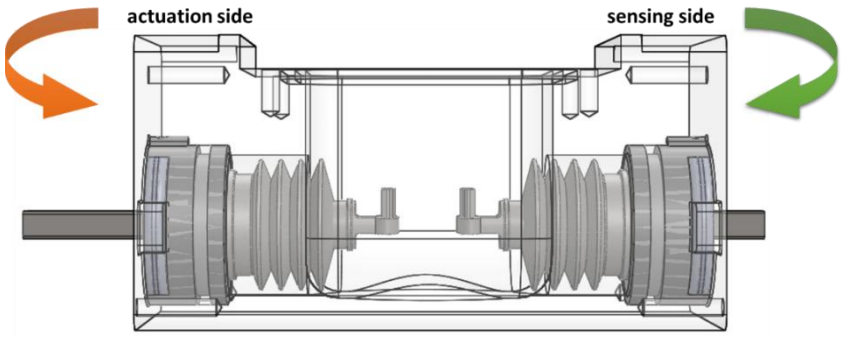

Figure 4: Culture chamber and lateral walls sub-assembly

The walls are made out of Polyoxymethylene (POMc), also known with the commercial name of Delrin®, an engineering thermoplastic material used in precision parts requiring high stiffness, low friction and excellent dimensional stability. The correct positioning of the walls within the chamber is guaranteed by the presence of a bulge on top of them while the insertion and extraction are assisted by a handle integrated on the external surface.

Along the longitudinal section the wall external profile fits, on one side, within the chamber lateral holes and seals the chamber by means of an O-ring, while allows, from the other side, to house the silicone bellow which wraps the shaft and seals the chamber. They are centrally drilled with a circular profile while a thin square profile is maintained at the bottom to prevent the shaft spinning during the mounting operations (Figure 5B). To reduce the friction of the moving shaft, the circular portion of the wall houses a cylindrical flanged lubricant-free bearing (iglidur A350, Igus, UK) (Figure 5B). This specific kind of bearing is

well-suited for oscillating applications, is temperature-resistant (up to 180 ° C) and FDA compliant.

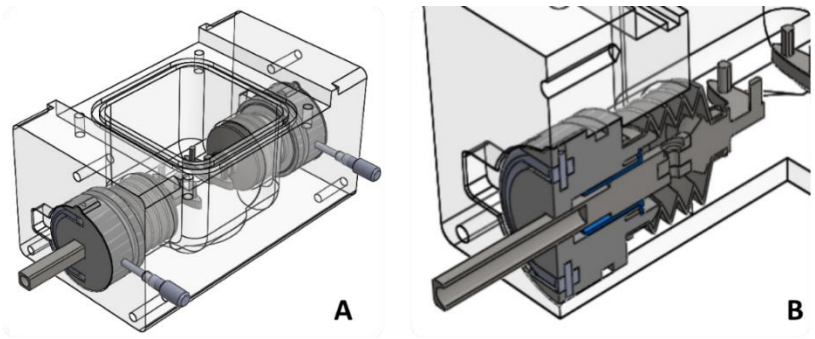

Figure 5: (A) Culture chamber and lateral walls. (B) Lateral walls, subassembly section view

Additionally, two lateral positioners made in AISI 316L[2], secure the walls to the chamber and the shafts position when the system is not in stimulation mode (Figure 5A). These positioners are instrumental in holding the constructs at a certain length after they have been placed within the culture chamber and before the culture unit is being connected to the actuators by the mechanical framework.

The shafts (AISI 316L) are rod shaped in the proximal part and have a square profile in the distal part to fit into the wall and to prevent the shaft spinning during mounting operations (Figure 5B). The proximal tip has been designed to couple several models of holders (or grasping system) in order to be compliant with more than one constructs shape.

[2] AISI 316L is a low-carbon version of the AISI 316 stainless steel, extensively used for many purposes due to its superior corrosion resistance, smoothness, biocompatibility (Hryniewicz, Rokosz and Filippi 2009)

A couple of medical grade silicone bellows were designed and fabricated *ad hoc* to wrap respectively the wall and the shaft (J-Flex rubber, UK) (Figure 5A, B). This solution prevents leakages from the internal part of the culture chamber allowing concurrently the translational motion of the shaft without introducing, for small displacements (5 up 10 mm), significant elastic forces or viscous friction.

Two interchangeable types of holders (POMc) were devised to couple the proximal part of the shafts. The first type (Figure 6A) is able to hold from 3 ring shaped constructs up to 6, if two layers are superimposed (nominal dimension: external diameter = 16 mm, internal diameter = 9-12 mm, height = 1-4 mm). The holder couples the shaft by means of an AISI 316L M3 screw. A radial bulge designed on the distal external profile prevents the bellows to be pulled out from the shaft motion during the stimulation operations. The proximal portion is the actual place where the constructs are placed: it is constituted by an oval base which holds three small rounded pillars. The second type (Figure 6B) acts like a standard grip and is more suitable for strip-like constructs (nominal dimension:, length = 15-20mm, width = 3-6mm, height = 2-7mm)

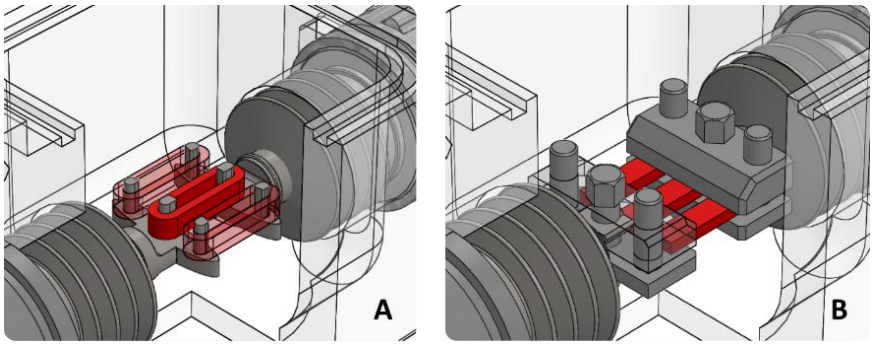

Figure 6: Sample holders for (A) ring-shaped, and (B) strip-like constructs

On the upper part of the chamber, the sealing is guaranteed by the lid, secured to the chamber with four M4 AISI316L screws (Figure 7A, component 1). The lid is made out of PC and has a central circular optical access for the visual inspection of the constructs during the dynamic culture (Figure 7A, component 2). On top of it, four seats, radially distributed around the optical access, allow to accommodate up to four bayonet fitting inserts that hold the sensors for the milieu monitoring (Figure 7A, components 3, 4).

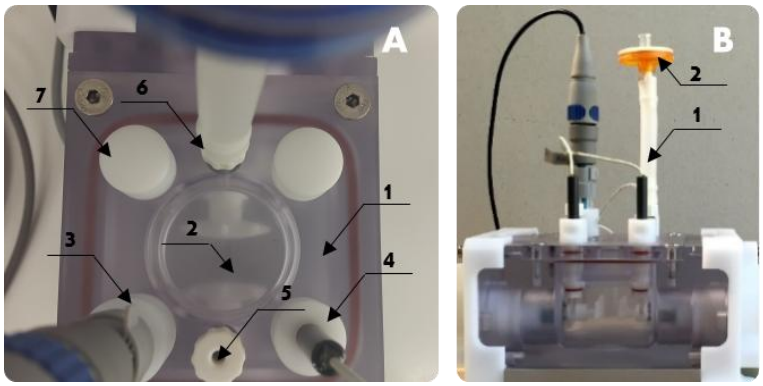

Figure 7: A, top view of the culture unit, elements: (1) lid, (2) circular optical access, (3, 4) bayonet fitting inserts, (5) inlet, (6) outlet and (7) cap. In B, lateral view, the outlet port is connected with (1) silicone compliance and, (2) filter

This solution makes the sensors removable; when they are not used, caps with the same fitting could easily be placed instead of them (Figure 7A, component 7). Furthermore, the chamber filling/emptying likewise the medium replacement is ensured by the presence of inlet (Figure 7A, component 5) and outlet (Figure 7A, component 6) ports[3].

In the platform here presented, the medium exchange is performed manually. However, the inlet and outlet ports make also possible to close the bioreactor within a perfusion feeding circuit for the implementation of an automatic recirculation of oxygenated culture medium. A perfusion feeding would allow to continuously perfuse the culture vessel with fresh

[3] Indeed, within any batch culture device, exhausted culture medium must be periodically replaced to restore the original nutrient and small-molecule concentrations (e.g. glucose, glutamine, grow factors, etc.) and deplete metabolites content (e.g. lactate, ammonia, indirectly restoring pH) within the culture medium.

medium and contemporarily remove exhausted medium to waste, allowing to maintain a quasi-steady culture environment.

Female autoclavable luer locks (1/8" NPT threaded, AISI 316) were used for the two ports on the cap. During the standard working condition, the inlet port is closed with a polypropylene male luer lock cap while the outlet port is connected with a 100 mm high compliance silicone tube (Figure 7B, component 1) that houses a 0.20um pore size filter (Sarsted, DE) on top(Figure 7B, component 2). The presence of the compliance is instrumental to accommodate eventual overpressure created by the displacement of the actuator while the filter on top is instrumental to the gases exchange within the incubator.

2.2.4 Structural Framework

The **structural framework** is devised to anchor the mutual position between all the components of the bioreactor. In particular, it holds together (i) the culture chamber, which contains the constructs, (ii) the linear actuator, which transmits the dynamic stimulation to the constructs, (iii) the position transducer, for the motor position feedback control, and (iv) the force sensor, which senses the construct reaction force. It does not enter in contact with any biologic material and fulfils a structural function. Besides, for the actuator working at high frequencies (up to 6 Hz) a certain well distributed mass is required in order to maintain stable the bioreactor.

With reference to Figure 8, it is composed by an anodized aluminum rectangular base (Figure 8, component 1) on which an aluminum sled (Figure 8, component 2) is screwed. The latter is the seats for the culture

unit and couples, on the actuation side, a permanently fixed lateral shell (Figure 8, component 3) which, internally, has the seat for the culture chamber. The contralateral right shell (Figure 8, component 4) is removable to allow an easy mounting of the culture unit. Externally, the left and right shells have, respectively, the proper seat for the linear actuator and the force sensor that are boxed in cylindrical holders (Figure 8, components 5 and 6).

On the lateral surfaces of the holders, elliptical apertures (Figure 8, element 7) permit to constrain, by means of small screws, the culture unit shafts, respectively, to the actuator and force sensor.

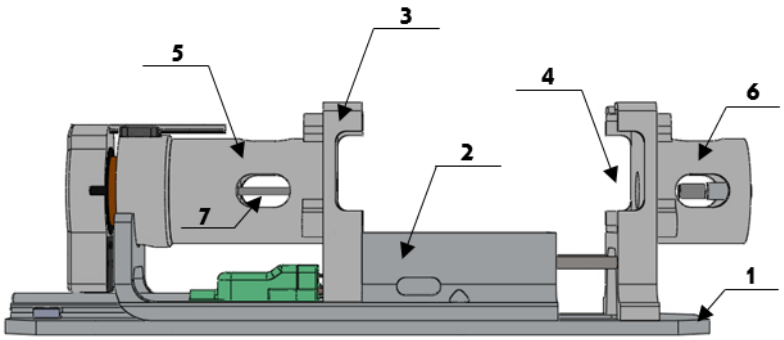

Figure 8: Structural framework components: (1) base, (2) sled, (3) fixed shell, (4) removable shell, (5) motor holder, (6) force sensor holder, and (7) aperture to connect the actuator with the culture unit shaft

Unless otherwise mentioned, all the parts meant to have a hydraulic seat were designed according to the specification of the O-ring manufacturer. The chain of tolerance for the mechanical components was chosen according to the ISO 2768 – mH. Components were obtained by machine tooling by CNC systems where end-to-end component design is

highly automated using computer-aided design (CAD) and computer-aided manufacturing (CAM) programs.

Table 2 summarizes a detailed list of the material used in the manufacturing of the bioreactor. Components are grouped in two categories, i.e. those entering directly in contact with biologic materials and those they are not.

Table 2: List of materials which the bioreactor is composed of

Components	Design Specification	Selected Material
Directly in contact with biological material		
Culture chamber Lid	Cytocompatibility, high Tg, high toughness, high thermal resistance T≥ 121 ° C, transparency, low thermal expansion coefficient	Polycarbonate (PC)
Chamber lateral walls Holders Sensors Insert	Cytocompatibility, high Tg, high toughness, high thermal resistance T≥ 121 ° C, transparency, low thermal expansion coefficient, good mechanical properties	Polyoxymethylene (POM)
O-Ring	Cytocompatibility, high thermal resistance T≥ 121 ° C	Medical grade Silicone
Shafts Screws	Cytocompatibility, high mechanical properties, high thermal resistance T≥ 121 ° , corrosion resistance	AISI 316L Stainless Steel
Containment bellows	Cytocompatibility, high thermal resistance T≥ 121 ° C	Medical grade silicone
Not in contact with biological material		
Mechanical framework (base, sled)	Lightness, high mechanical properties	Anodized Aluminum
Lateral shells Motor holder Force sensor holder	High Tg, high toughness, high thermal resistance T≥121 ° C, transparency, low thermal expansion coefficient, good mechanical properties	Polyoxymethylene (POM)
Screws Couplings	Good mechanical properties, corrosion resistance	AISI 316 Stainless Steel, Aluminum

2.2.5 Stimulation and sensing unit design

As sketched above, the **stimulation and sensing unit** comprises two distinct sub-units (Figure 9). In the next sections, firstly the design of the **stimulation unit** is detailed described. To begin, the sizing of the actuator and the relative power hardware was addressed; then a lumped model of the device was created in order to define the proper control architecture.

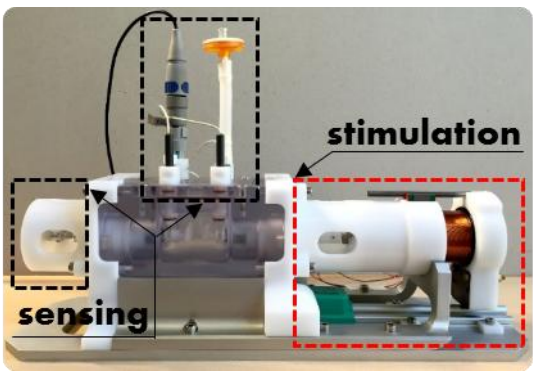

Figure 9: Subunits which compose the stimulation and sensing unit

To follow, the design and implementation of the **sensing unit** for sensing the culture and the constructs properties is illustrated.

2.2.6 Stimulation unit design

Mechanical stimulation devices used in Tissue Engineering applications, often use stepper motors to fulfil the purpose; however, several issues have been ascribed with the use of such actuators. Firstly, they have bandwidth limits that would prevent experiments with higher cyclic rates (frequency), and the addressing of such problems decreases

the mechanical displacement resolution. Additionally, such motors are susceptible to resonant vibrations in the range of frequencies where they are commonly used.

The use of voice coil devices, whenever accurately controlled, could overcome these limitation. (Salazar, et al. 2015) Within the electric motors, voice coil actuators are electromagnetic devices which produce accurately controllable force over a limited stroke with a single coil or phase. These devices are capable of extremely high accelerations (more than 20g), and great positioning accuracy when suitably controlled. Indeed, to fulfil the given specifications, the actuation system of the bioreactor was designed using a voice coil linear actuator. Moreover, the use of a linear actuator simplifies the kinematic mechanism to produce the linear displacement.

2.2.6.1 Actuation system sizing

The GVCM-051-064-01 (Moticont, CA, USA) linear voice coil motor was integrated into the mechanical framework. This actuator consist of two separate parts; an external magnetic housing and a moving coil which is supplied with an internal linear bearing and shaft to support the moving coil.

The actuator is able to yield a maximum continuous force of 29.7 N and a maximum stroke of 31.8 mm which are within the range of specification required for this application. As the displacement transducer is instrumental for the actuation of the standard control strategy, the ONP1-A (Gefran, BS, IT) contactless linear position transducer has been used. They are both integrated onto the mechanical

framework as illustrated in Figure 10, where the chain of transmission of motion between the actuator and culture unit is also described in detail.

While the transducer is fixed to the base, the linear transducer magnetic slider is integral with the motor coil. The mutual positioning between the slider and the transducer body is respectful of the manufacturer indications.

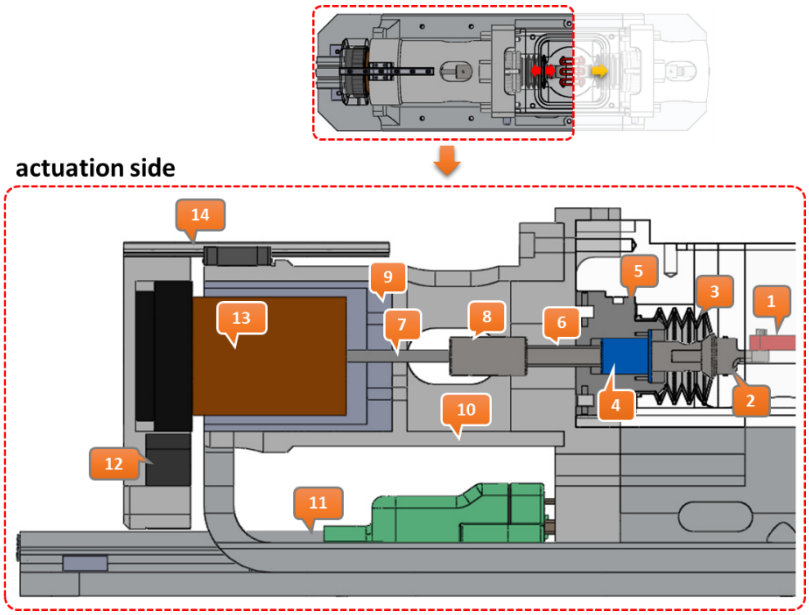

Figure 10: Actuation side, chain of transmission of motion between the actuator and culture unit. The construct (1) is gripped by the holder (2) which is connected to the shaft (2).The bellow (3) tightly wraps around the proximal part of the holder to insulate the chamber from the outside. The shaft, routs along the lubricant-free bearing (4) locked on the lateral wall (5).The shaft is distally hollow to couple the voice coil axle (7) by means of a joint (8). The magnetic housing (9) of the voice coil is fixed to the holder (10). Underneath, the position transducer (11) is fixed to the base while the magnetic slider (12) is anchored to the motor coil (13). Finally a linear guideway (14) prevents the spinning of the coil with respect to magnetic housing.

A detailed mechanical and electrical specification list for the linear voice coil and position transducer is reported in Appendix.

The motor maximum continuous force versus stroke characteristic is depicted in Figure 11. A decrease of force at extreme strokes is observed from the datasheet. In such positions, the actuator coil is not completely linked by the magnetic field of the inner permanent magnet. Although a

performance decrease is expected in these conditions, the actuator is designed to work around mid-stroke to avoid reaching the extremes.

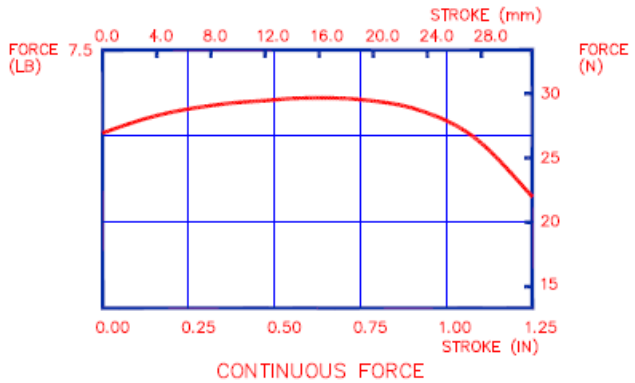

Figure 11: Voice coil actuator characteristic (Moticont, GVCM-051-064-01)

With such hardware, a power module was needed to implement the control architecture. If a continuous force of 30 N is considered, which leads to a continuous current of 3,13 A ($i_{\text{cont}} = {}^{30N}/_{9,6\ N/A}$), the NI 9505 Full H bridge power module (National Instruments, TX, USA) was considered appropriate for the purpose. This device is able to drive loads with continuous current up to 5 A, and intermittent operation at 7.3 A. Furthermore, for the acquisition and conditioning of the position transducer output signal, the NI 9219 module (National Instruments, TX, USA) was chosen. Both the modules for the motor control (NI 9505) and the signal acquisition (NI 9219) allow a full integration with the cRIO NI 9075 (National Instruments, TX, USA) real-time controller which has been selected for the implementation of the real time monitoring and control of the bioreactor operations.

2.2.6.2 Actuation control: a lumped model of the linear actuator

From the modelling point of view, the voice coil actuator can be represented with the following differential equations:

$$V = L\frac{di}{dt} + Ri + K_e v \qquad \text{Eq. 1}$$

$$K_f i = m\frac{dv}{dt} + cv + F \qquad \text{Eq. 2}$$

Eq. 1 describes the electromagnetic behaviour of the device, which depends on the impedance parameters of the voice coil winding (resistance R and inductance L) and the back electromotive force (EMF) constant K_e. The related variables are the input voltage V, the winding current i and the stroke speed of the moving parts v.

On the other hand, the electromechanical dynamics of the system are governed by Eq. 2, where an input force is proportional to the current i by a force constant K_f. Such force is then filtered by the mechanical lumped parameters, i.e. the mass of the moving parts m and the friction losses, which, in this case, are represented as purely viscous with a damping c. Finally, the output force exerted to the probe is F. A schematics of the model is reported in Figure 12:

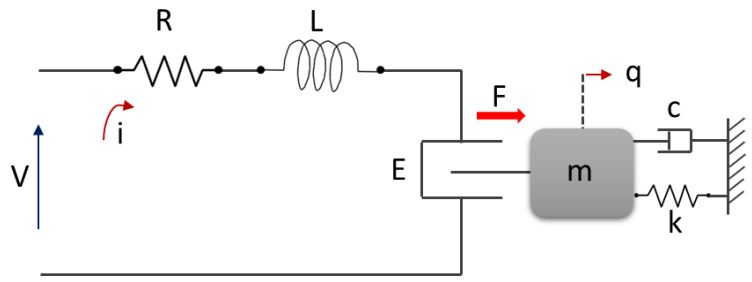

Figure 12: Lumped model of the linear actuator; V is the voltage command, i is the generated current, R and L are the resistance and inductance respectively. E is the back electromotive force, m the mass of the moving part, k and c the stiffness and damping elements, q the position and finally F, the force exerted to the probe.

If iron losses are neglected, the back EMF constant and the force constant can be assumed equivalent, and hence, defined as the motor constant $K_e \cong K_f = K_m$.

A conventional cascade feedback loop control strategy was implemented in this case. The control consists of (1) an inner current feedback loop, designed as a Proportional-Integral (PI) compensator and (2) an outer displacement feedback loop, composed as a Proportional-Integral-Derivative (PID) compensator (Ogata 2010). The general architecture is illustrated in Figure 13.

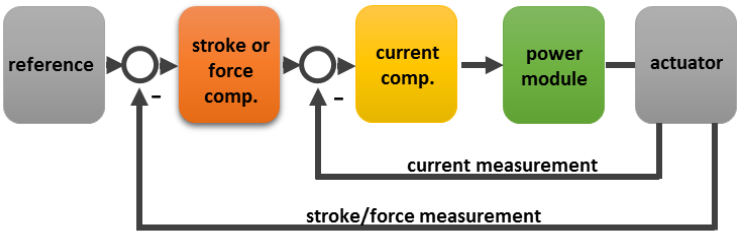

Figure 13: Cascade control architecture: (1) inner current feedback loop and (2) outer displacement feedback loop

For the inner loop, current measurements are performed by the shunt resistance inside the power module, while a dedicated displacement transducer is required for the outer feedback loop. Noteworthy, the same control structure could be used also if a force control is desired, with the only difference of having a force transducer in place of the position transducer.

In contrast with the approach followed for the inner current loop, the position compensator was tuned using Simulink Control Design™ toolbox. The PID gains were selected by observing the rise time, the settling time and the maximum overshoot of the closed-loop step response in the time domain, and the gain and phase margin of the loop function in the frequency domain. These values, which are inherent of classic control design methods (Ogata 2010), are made available through the tuning procedure inside Simulink Control Design™ as the control gains are modified.

Furthermore, to compensate friction effects and provide effective mitigation of the dry friction phenomena that take place from the

contact between moving parts, a feed-forward loop was also integrated (Armostrong-Hélouvry 1991). In this case, the goal was to implement a non-linear law that determines the sign of the stroke rate and yields a constant contribution of force F_0 in correspondence to the sense of motion. Further analytical details on the control model and position compensators design are reported in Appendix.

2.2.7 Sensing unit I: culture monitoring sensors

The bioreactor was equipped with sensors for real time monitoring and recording of the most critical milieu parameters i.e. pH and dissolved oxygen partial pressure (pO_2). As already mentioned, the lid was devised to be compatible with up to four sensors; in fact also the carbon dioxide (pCO2) and temperature sensors (T) were considered to be incorporated in the design, even if not yet integrated in the control and monitoring unit. Figure 14 shows as the full configuration would appear. Selected sensors were all "invasive", which means that they must be placed directly in contact with the culture medium bulk to obtain measurement. From the design point of view, sensors are inserted within the culture well through the dedicated inserts on the cap of the bioreactor. (Figure 14). The inserts, allow the sealing and the holding of the sensing position.

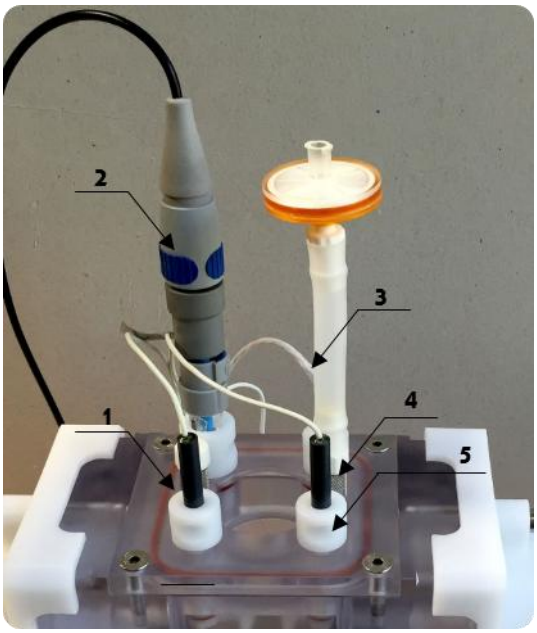

Figure 14: Example of the lid equipped the full configuration of sensors. (1) pO_2, (2) pH and (3)temperature, (4) CO_2 sensors (5) bayonet fitting insert to hold the sensors within the culture

Special care was devoted in selecting sensors small in size and suitable for standard sterilization procedures in order to avoid any contamination risk along the culture. For the dissolved oxygen measurement, the MI-730 Micro-Oxygen Electrode (Microelectrodes Inc., NH, USA) was chosen, as an electrochemical sensor commonly used for oxygen measurements in biological fluids or water (namely Clark cell). The current produced by the redox reaction that develops inside the electrode, is converted in voltage, by means of an adapter serially connected with the sensor. With regard to the pH measurement, the InLabUltraMicro sensor (Mettler Toledo, ZH, Switzerland) was chosen.

Analog signals from the sensors were processed and digitalized by means of the NI 9219 acquisition module (National Instruments, TX, USA) The latter was embedded within the cRIO NI9075 (National Instruments, TX, USA) real-time controller, selected for the implementation of the real time monitoring and control of the bioreactor operations.

A full characterization of the sensors, also to ascertain their sensitivity within the nominal ranges of a standard *in vitro* culture conditions (De Rossi, et al. 2004), was preliminarily carried out in a separate dedicate bench test, then, for each sensor, a specific calibration protocol has been developed according to their physical principle and to the manufacturer indications. After the procedures were standardized, they were integrated in the monitoring and control unit software, developed for the bioreactor operations. Indeed, in order to obtain reliable results, a calibration of the sensors is needed on a regular basis.

Appendix illustrates in details the experimental set-up and characterization procedures.

2.2.8 Sensing unit II: construct monitoring sensor

To continuously monitor in real-time the mechanical properties of cultured tissues, the system was devised to incorporate a force sensor. The tissue reaction force is measured using a load cell placed outside the culture chamber. The tissue is located within the culture chamber where is clamped by the holders. It is stretched on one side from the linear actuator while it is held on the opposite side, which means that the force has to be transmitted to the force sensor through the lateral wall. Figure

15 describes in detail a partial section to illustrate the mechanical elements devised to transmit the force from the construct to the load cell. The machining tolerances of the pieces and the correct mounting of the assembly ideally guarantee the correct coaxiality, i.e. the absence of any torque. However, to improve the coaxiality, a lubricant-free bearing has been introduced.

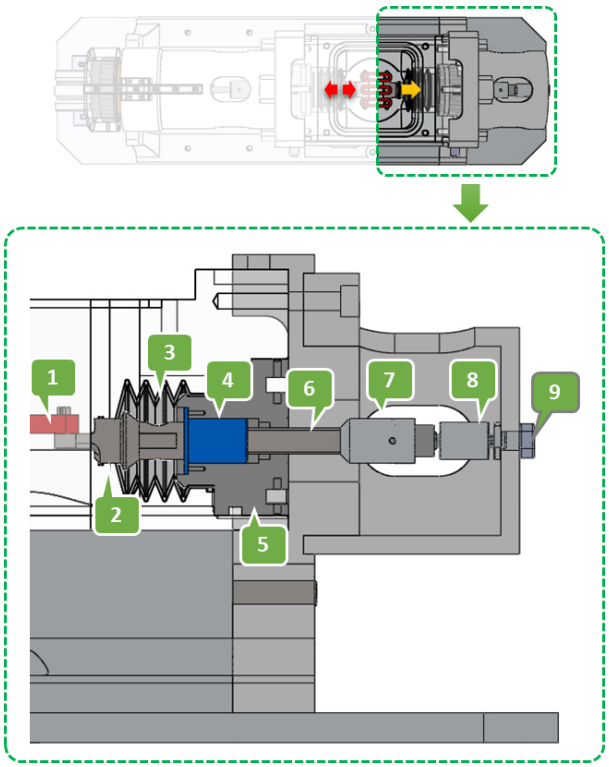

Figure 15: Force sensing chain. The passive reaction force of the construct (1) is transmitted to the holder (2) which is connected to the shaft (6).The bellow (3) tightly wraps around the proximal part of the holder to insulate the chamber from the outside. The shaft, routs along the lubricant-free bearing (4) locked on the lateral wall (5).The shaft is distally hollow and threaded to couple a joint (7) which fits into the left arm of the load cell (8). The latter is fixed to the case by means of a nut (9)

The load cell chosen is a XFTC300-S109 (Measurement Specialties, VA, USA) 10N full scale range force sensor. Special attention was dedicated to the insulation of the cell in order to reach sufficient protection level for a correct functioning within the incubator. The load cell measures tension and/or compression in static and dynamic applications. A signal conditioner, ARD154 (Measurement Specialties, VA, USA), boosts the signal level and increases measurement resolution also improving signal-to-noise ratio. Also in this case, the analog signal from the load cell was processed and digitalized by means of the NI 9219 acquisition module (National Instruments, TX, USA) embedded within the cRIO NI9075 (National Instruments, TX, USA).

2.2.9 Monitoring and control unit design

In this section the architecture of the **monitoring and control unit** is described. The latter oversees (i) the feedback loop motion control strategy, (ii) the acquisition of the signals from the sensors and, (iii) the communications from and toward the user, by means of a real-time structure. A real-time system (which consists of software and hardware components) is able to reliably execute programs with very specific timing requirements, which is instrumental when high performances are required from a device, i.e. the linear actuation control.

LabView® graphical system design platform (National Instruments, TX, USA), has been identified as the suitable environment to integrate all the requirements and in specific for the development of a (1) real-time system for the embedded control of the stimulation unit and, (2) the monitoring of the sensors signals. In addition, LabView® consented

to develop a user-friendly software interface which allows the user to set and monitor the operating culture conditions. The user interface was requested essentially to administer tasks related to the (1) setting of a specific displacement/position mode or (2) receiving, processing and saving of the data from the sensors.

The National Instruments hardware was considered the most appropriate choice for the implementation of the embedded monitoring and control architecture and for the compatibility with the sensors and the actuator. A detailed list of the technical features of the hardware modules, which have been used, is reported in Appendix.

To guarantee the adequate functionality of the hardware elements used in the design, a host–target application architecture has been developed according to the scheme in Figure 16.

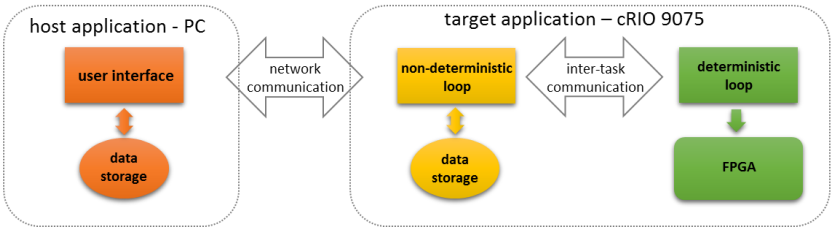

Figure 16: host-target application architecture

The *host application*, is the actual software developed with LabView®. It runs on the PC and executes actions with VI's sending commands to the target and receiving information from it. The cRIO 9075 (real-time processor) (National Instruments, TX, USA) is the *target application*, a platform suggested for embedded applications.

The architecture of Figure 16 was structured in order to parallelize two main processes, (1) the mechanical actuation (a bidirectional dataflow from host to target), and (2) the signals from sensors (a unidirectional dataflow from target to host)

In detail, for what concerns the mechanical status, the software controls four conditions for the bioreactor: (1) the stand-by condition, (2) the activation/deactivation of the control status, (3) cyclic motion, e.g. sinus waved, square-waved and triangular waved displacement, and (4) the ramp displacement.

These operational modes, were organized, within the user interface, in two main panels which can be selectively activated by the user i.e. (a) Mechanical Stimulation Panel and, (b) Characterization Panel. Controls and indicators allow the user to actively command and monitor the operations. They are composed by three main sections: (i) a status indicator which summarizes the current settings, (ii) an area were the user inputs the values and chooses settings for the action required and, (iii) an area where the signals form the stimulation components are graphed.

In Figure 17 the Mechanical Stimulation Panel is depicted. The user can choose the stimulation mode, stimulation frequency and duration, the % of displacement as well as move backwards and forwards with a step of variable amplitude. On the right part, the position transducer displacement signal is visualized as well as the force developed by the motor during the motion.

Figure 18 shows the Mechanical Characterization Panel. The user can move backwards and forwards with a step of variable amplitude, then set the slope of the ramp (mm/min) as well as the maximum displacement.

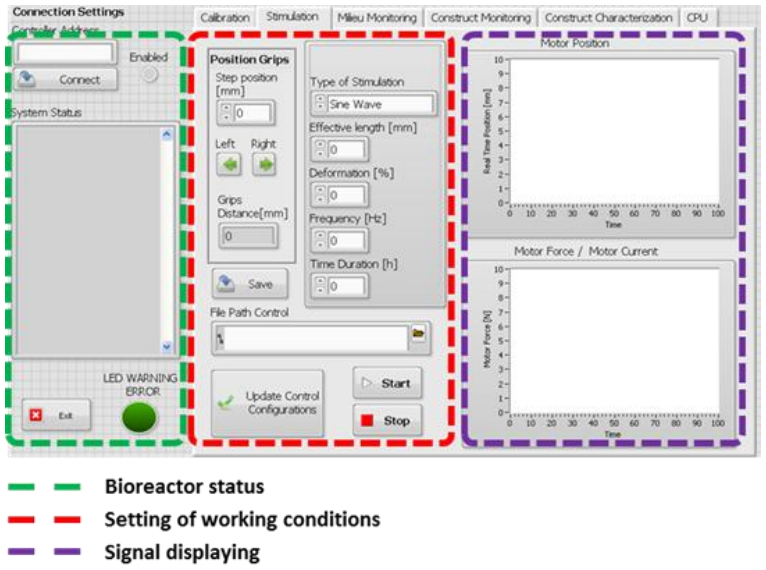

Figure 17: Mechanical Stimulation Panel. (i) Dashed green indicates a status indicator which summarizes the current settings, (ii) dashed red the area were the user inputs the values and chooses settings for the action required and, (iii) in dashed purple the area where signals from the stimulation components are graphed

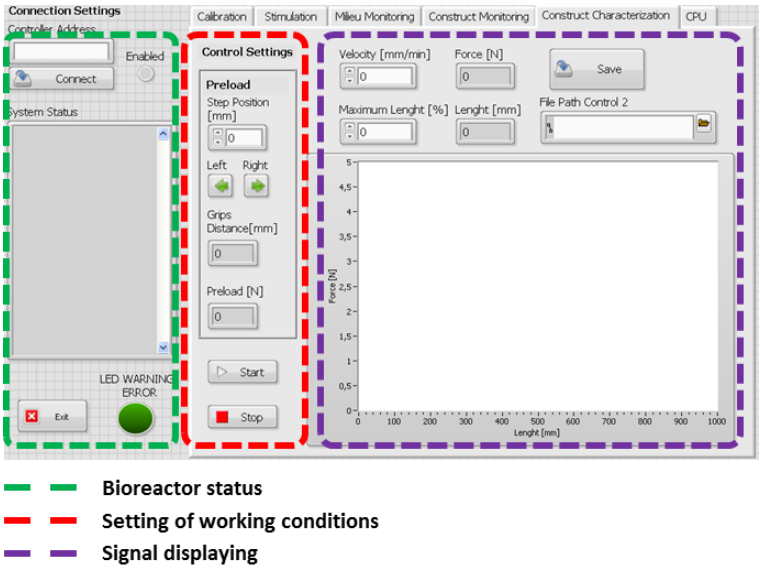

Figure 18: Mechanical Characterization Panel. (i) Dashed green indicates a status indicator which summarizes the current settings, (ii) dashed red the area were the user inputs the values and chooses settings for the action required and, (iii) in dashed purple the area where the position VS force data are graphed

On the other hand, the software allows to execute actions on the signals from the sensors. Two main events are executed within the user Interface, i.e. by the host, (1) the calibration, where the signals are calibrated according to the experimental procedures (independently developed) and, (2) the visual displaying/saving of the signals

The correspondent panel is the so called Monitoring Panel, reported in Figure 19. The calibration section allows to access into an interface specifically designed to guide the user within the calibration. Furthermore, the saving of the signals could be enabled by the user.

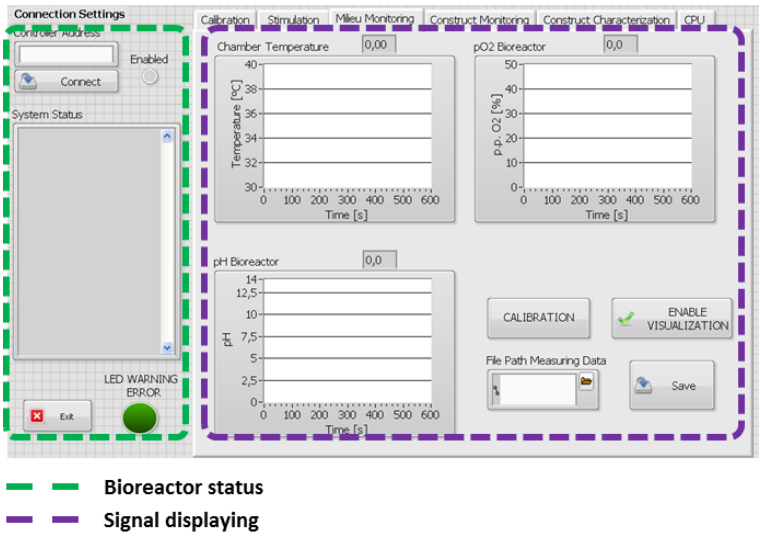

Figure 19: Monitoring Panel. (i) Dashed green indicates a status indicator which summarizes the current settings, (iii) in dashed purple the area where the signals from the sensing unit components are graphed

Technically, the cRIO target system executes (1) the proportional-integral-derivative control algorithm with the proper loop rates and interacts directly with the linear voice coil actuator[4], and, (2) the sensor signal acquisition. Motion control tasks, according to the control model outputs, are real-time performed. Indeed, as predicted by the model, each level of the control architecture has to work within a specific bandwidth.

These two tasks run in parallel. To correctly control the actuator and process the data the two loops need to be synchronized. The NI 9219 acquisition module (Analog input module) acquires at the same time

[4] The control loop was firstly modelled and tuned in Matlab/Simulink then the obtained parameters were used in the LabView implementation.

each channel. The sampling frequency is determined by the fastest operation that is required in the system; indeed, to actuate at high frequencies (up to 6 Hz), the linear position transducer analog signal should be consequently sampled. Also, for the load cell, to follow dynamically the changes in the force at high frequencies, the signal should be sampled with same criteria, while the other signals i.e. pH and pO_2 have slower dynamics. Hence, the maximum NI 9219 acquisition module sampling frequency, 100 S/s, was considered satisfactory.

The modules, cabling as well as the connectors from and toward the actuator/sensors were boarded in the so called control box.

2.3 Bioreactor assessment and results

2.3.1 Units assembling and preliminary operations

The bioreactor components were assembled together to check the couplings and the ease of assembling/disassembling. The mechanical framework was assembled and, both the motor and the position transducer anchored to the chassis. The mutual position between the transducer and its sliding element, fixed to the bottom of the coil, was verified.

The culture unit was assembled separately and finally the sensors mounted on top by means of the dedicated inserts. The compliance was connected to the outlet port and a luer fitting cap on the inlet port.

Afterwards, the culture unit was installed within the framework. On the "actuation side", the concentricity and coaxiality of the motor shaft with respect to the culture unit shaft was also ascertained. After the coupling, no appreciable friction was detected in moving by hand the coil, which seemed to slide freely. On the "sensing side", contralateral to the actuation, the load cell was fixed to the holder and clamped with its own joint to the culture unit shaft.

The actuator, position transducer, the pH and oxygen sensors were connected to the control box by means of dedicated connectors. Finally, the control box was connected to the PC by means of a LAN cable. Preliminary controls were executed to check the correctness of the electrical cabling. Figure 20 shows in detail a complete view of the system once the components were assembled.

Figure 20: Culture unit installed within the mechanical framework. In the upper panel a perspective view of the bioreactor is represented. In the middle panel details on the sensing (left picture) and actuation side (right side) are reported while the lower panel shows the top view

Figure 21 shows an enlarged view of the system which comprehends (1) the control box (2) the PC with the software for the monitoring and control operations.

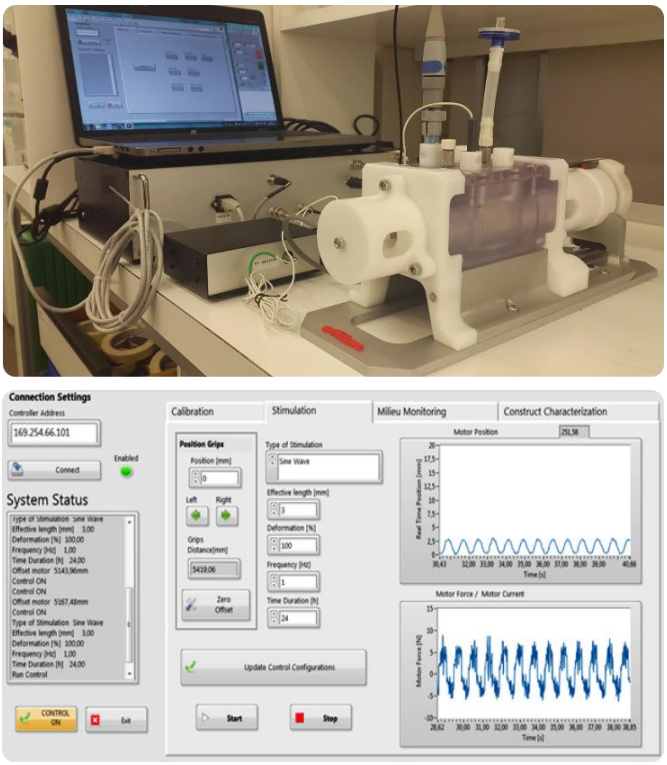

Figure 21: Monitoring and control system

The software was preliminary tested for the single subsystems, then the functioning of all the controls and indicators within the three main software panels (1) Stimulation Panel, (2) Monitoring Panel and, (3) Characterization Panel was ascertained.

2.3.2 Stimulation unit tuning and assessment

To speed up the tuning of the actuation control loops and determine the starting values for the Proportional-Integrative-Derivative (PID) compensator, a lumped control model of the actuation system was

implemented in MATLAB/Simulink®. The output values served as a basis for the control tuning in LabView®. Subsequently, the generated displacement and its accordance with the input reference, in terms of frequency and amplitude, was verified on the real system. To address defective reference tracking, an additional mapping gain element was used to adapt the output amplitude to the desired value. Next sections illustrates in detail these assessment operations.

2.3.2.1 Actuation control model, simulation and results

The lumped control model of the actuation system was implemented in MATLAB/Simulink®, as shown in Figure 22. Indeed after having implemented the control structures in LabView®, the existence of the model was advantageous to base the initial values.

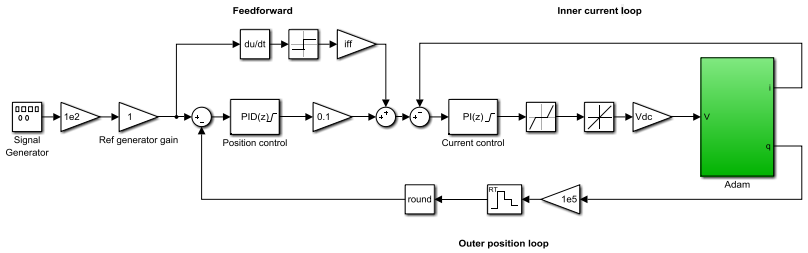

Figure 22: MATLAB/Simulink® model of the complete control system.

This model contains the already described control architecture enhanced with further implementation details. The plant (actuator) is represented as a subsystem with one input (voltage V) and two outputs (current i and position q). The mechanical parameters of the plant are listed in Table 3.

Table 3: Plant parameters

Parameters	Value
mass (g)	333,5
viscous friction coefficient (Ns/m)	20,31
stiffness (N/m)	50
dry friction force (N)	3,84

The controllers were discretized at specific sample rates to emulate their implementation on the LabView® hardware. The derivative action of the outer-loop PID was filtered to avoid infinite gains at high frequencies. Integral wind-up was limited using a clamping algorithm (Visioli 2003). Furthermore, the position feedback signal was under sampled and rounded to reproduce the limitations of the target hardware[5]. The feed-forward current gain (Kff) was identified by finding the Coulomb friction force offset of the device. The system parameters are summarized in Table 4.

[5] Indeed, an important aspect regards the power stage inability to realize infinitely small duty cycles. Minimum conduction time was taken into account from the manufacturer's datasheet.

Table 4: Control model parameters

Parameter	Value
DC bus voltage (V)	24
current saturation (A)	3
inner loop bandwidth (Hz)	500
inner loop proportional gain (1/A)	0,223
inner loop integration time constant (ms)	0,436
inner loop discretization step (us)	50
feedforward current gain (A)	0,3
outer loop proportional gain (A/mm)	1,2
outer loop integration time constant (s)	1,43
outer loop derivative time constant (s)	0,02
outer loop discretization step (ms)	10
power stage minimum conduction time (us)	2

For simulation purposes, the model was executed using the ode23s variable-step integration method with a maximum step size of 50s. This solver choice is suitable for electromechanical system models, which are usually stiff due to the presence of time constants different in orders of magnitude.

A broad range of working condition have been simulated in terms of displacement and frequency. Nevertheless, at the present, the span has been limited to the range of 0.5-3mm displacement, and 1-6Hz frequency.

Three main output values were considered significant: (1) the position measurement versus position reference profile (2) the current measurement versus current measurement profile, and (3) the voltage command curve. Each simulation run is characterised by the following parameters:

- Amplitude of the position reference waveform
- Frequency of the position reference waveform
- Reference gain used for that particular condition

Firstly, in Table 5, the most inherent response features for the control system are reported.

Table 5: Control system response features

Parameter	Value
rise time (s)	0,02
settling time (s)	0,66
overshoot (%)	6,59
gain margin (dB)	9,93
phase margin (deg)	61,3

For clarity of dissertation, only some working condition are presented, being the intermediate condition less relevant. In the figures: position measurement (solid, blue) versus position reference (dashed) is reported in the first line; current measurement (solid, blue) versus current reference (dashed) in the middle line while the voltage command is reported on the lower line.

Amplitude: 0.5mm, Frequency: 1Hz, Gain: 1.04

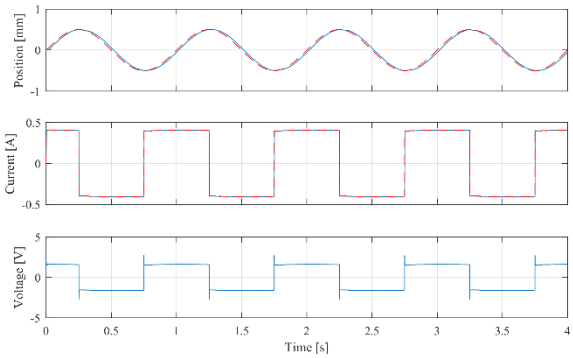

Figure 23 – Amplitude 0.5 mm, 1 Hz

Amplitude: 3mm, Frequency: 1Hz, Gain: 1.04

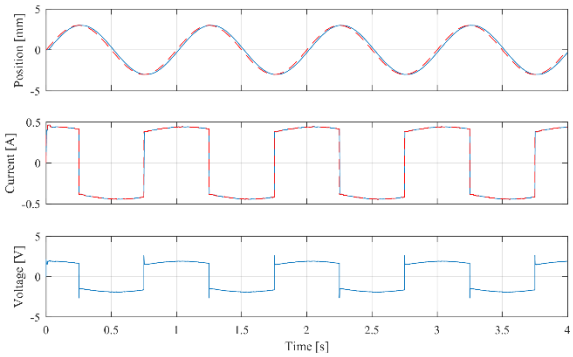

Figure 24 – Amplitude 3 mm, 1 Hz

Amplitude: 1mm, Frequency: 6Hz, Gain: 1.2:

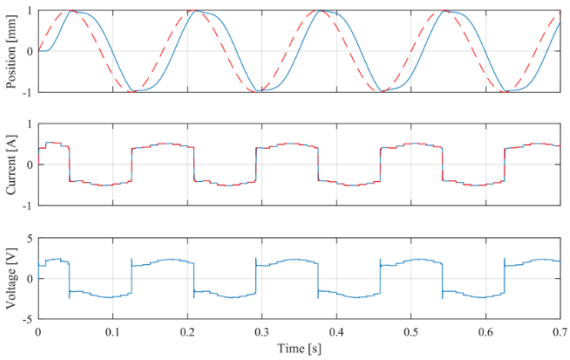

Figure 25 - Amplitude 1mm, 6Hz

Amplitude: 3mm, Frequency: 6Hz, Gain: 1.2:

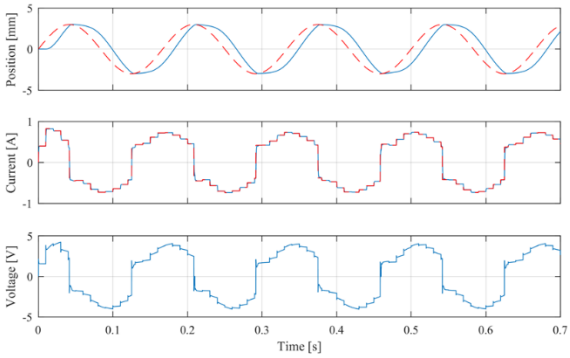

Figure 26 - Amplitude 3mm, 6Hz

As expected, the gains to be used in in LabView® control tuning (1 Hz, G_{ref}: 1.04, 2 Hz, G_{ref}: 1.1, 6 Hz, G_{ref}: 1.2) are independent from the amplitude for two main reasons:

(1) The system is not in saturation which means the actuator doesn't require high current and so the amplitude variation is not heavily affecting the voice coil performances.
(2) There is only one non linearity implemented in the model: the friction which has been modelled as the contribution of the (i) viscous friction, and (ii) the Columbian friction. However, the latter is balanced by the feed-forward loop.

The output values served for the control tuning in LabView®.

2.3.2.2 Motion verification

Once the system was assembled and put in standard operative conditions, the generated displacement and its accordance with the input reference, in terms of frequency and amplitude, was verified.

The input reference of the system consists of a desired waveform profile to follow. During static or quasi-static testing, position and current errors tend asymptotically to zero due to the integral action of the compensators. Indeed in the actual system, during dynamic excitation, perfect reference tracking is not guaranteed in transient conditions. To address this issue, an additional mapping gain element is used to adapt the output amplitude to the desired value. This approach includes the introduction of a gain coeffient K for the PID value, and it is valid because there is interest in providing a specific waveform amplitude, disregarding of the phase lag between input and output. In this particular case, this mapping has to be experimentally tuned by

spanning the broad dynamic working range of the device and suitably selecting a reference gain for specific amplitude and frequency conditions.

The generated displacement and its accordance with the input reference, in terms of frequency and amplitude, was verified. Starting from the Proportional-Integrative-Derivative (PID) values from simulation output (kp:0.0122; kd:0.098; ki:4e-5), the most acceptable K-PID and Kff values were found by spanning a sub selected dynamic working range of the device (0.5-3mm at 1 Hz). Reference gains found for the specific displacement are reported in Table 6.

Table 6: K-PID and Kff values obtained from the experimental mapping

Amplitude(mm)	KPID	Kff
0,5	5	3,1
1	5	3,3
1,5	4,6	2,9
2	4,3	2,9
2,5	4,25	2,85
3	4,2	2,9

The input reference and the correspondent output waveforms are grouped and shown in the position measurement (solid, black) vs position reference (dashed, black) are superimposed, the amplitude ranges between 0,5 and 3mm with 0,5 step increment. (Time in seconds on the x axis and displacement in mm on the y axis).

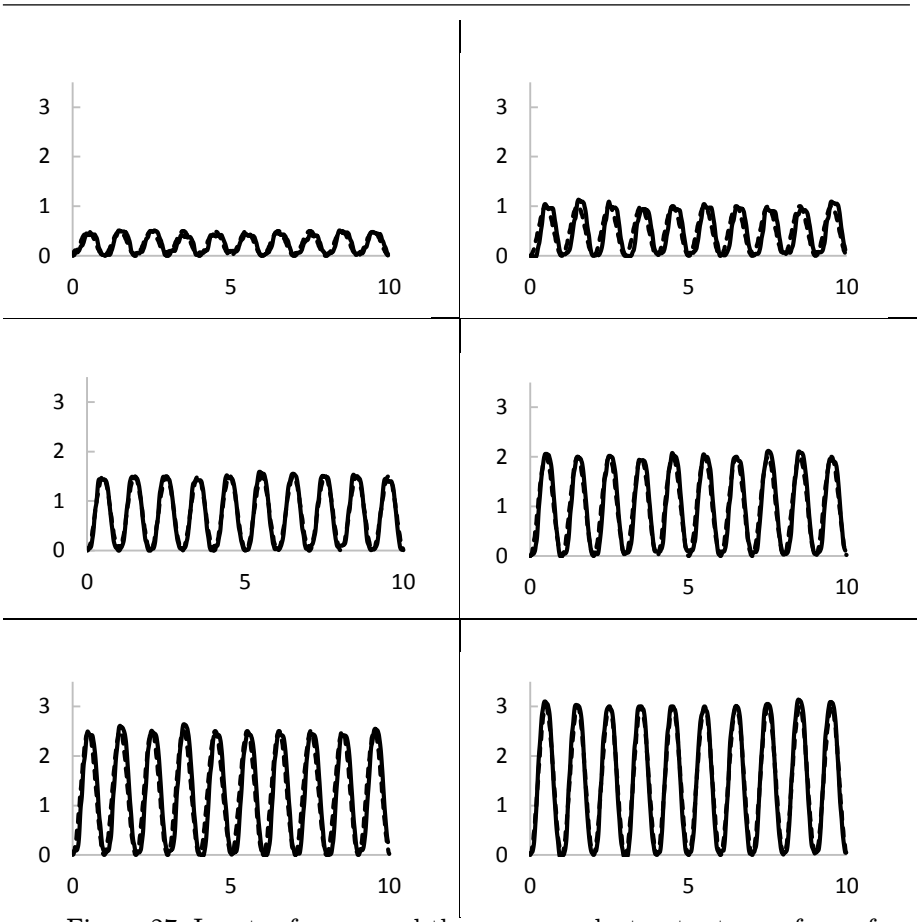

Figure 27: Input reference and the correspondent output waveforms for displacement in the range 0.5-3mm @ 1Hz. Time in seconds on the x axis and displacement in mm on the y axis

For low displacements i.e.0.5-1mm, the actuator is able to follow the reference with a discrete performance. The signals appears to be regular in frequency even with moderate oscillations on the peak amplitudes. In the considered window, i.e. 10 seconds of signal, the lowest measured waves show an error, with respect of the nominal value of 30%, at 0.5mm

and 13% at 1mm respectively, while the highest peak to peak waves are moderately lower. Besides, the shape is not always regular.

For higher displacements, from 1,5mm up to 3mm, the actuator is able to follow the reference with a better performance. The signals appears to be regular in frequency and even if some oscillations on the peak amplitudes are present, the repeatability of the signal increases. Errors range between 8.7 and 3.3%.

Discrepancies found between the model and the real system are to be ascribed to hysteretic non-linearities which are present and too intricate to be included in a first approximation model. Further improvements can be obtained with a refinement of the mapping procedure. Besides, the system showed an enhanced sensitivity to the initial coil position. However, this latter issue is consistent with the intrinsic characteristics of the voice coil and can be override positioning the coil congruently.

2.3.3 Sensing unit assessment

2.3.3.1 pH and O2 sensors

The pH and O2 sensor's characterization procedures have been developed independently from the platform, before the system was completed and assembled. This approach is valid because, during operations, the calibration of these two sensors is done before they undergo to sterilization process and assembled into the lid of the bioreactor. A dedicated bench test has been devised for the characterization of each sensor. The bench was composed by: (1) the NI 9219 (National Instrument, USA) acquisition module embedded in the

CompactRIO-9075 chassis (National Instrument, USA) and, (2) a PC where a dedicate purpose-built software interface developed in LabView (National Instrument, USA) allowed to acquire and record signals from the sensors. After the procedures were standardized, they were integrated in the main user interface, developed for the bioreactor operations.

Sensitivity, and offset values for both O2 and pH sensors are reported in Appendix. Furthermore, for the pH sensor, an additional validation test has been carried out to ascertain the ability of the sensor to measure small changes of pH in a narrow range around pH 7. In the Appendix the procedures are firstly described, and a scheme is furnished to assist the user step by step in the calibration process.

2.3.3.2 Force sensor

The assessment of the force sensor regarded the evaluation of the inaccuracy in sensing that could originate by the adopted architectural solution. In fact, the force exerted by the constructs has to be transmitted from the inside of the culture unit through the lateral wall to the force sensor. Even if the machining tolerances and the correct mounting of the assembly ideally guarantee the coaxiality and the absence of any torque, yet, significant friction due to potential misalignments could be originated.

After a preliminary calibration, tests were carried out to verify that the mechanical coupling between the cell and the probe (the construct holder) allows the correct sensing. Therefore, the ability of the sensing system to determine the mechanical stiffness of a calibrated

instrumentation spring was verified. The spring stiffness was previously determined using an MTS standard tester (MTS System Corporation, USA) equipped with a 10N full scale range load cell. A linear regression on the force-displacement data was carried out to calculate the slope of the curve in the linear region. Results from three independent tests gave a mean value of 0.057 ± 5.19e-5 N/mm.

The spring stiffness was estimated in three bioreactor configurations: (i) load cell directly connected to the shaft, (ii) complete configuration including the lubricant-free linear bearing and, (iii) complete configuration in absence of the lubricant-free linear bearing. Figure 28 illustrates the three configurations.

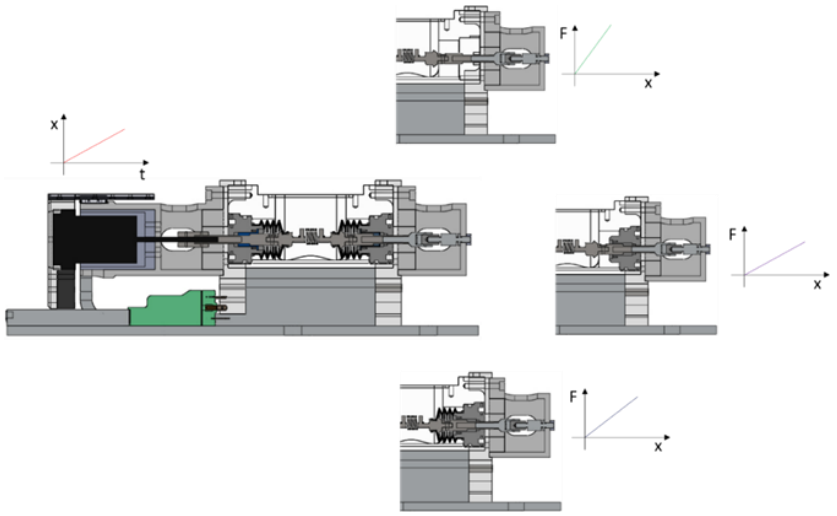

Figure 28: Scheme of the testing conditions, from the top to the bottom (1) load cell directly connected to the shaft (2) system in the complete configuration including the bearing, and (3) system without in the complete configuration excluding the lubricant-free bearing.

The tests were carried out in dry condition, i.e. without any fluid inside the culture unit, setting in the Characterization Panel a ramp displacement with a nominal speed of 5mm/min and a total displacement of 3mm. A minimum of three independent test were run for each condition. Results in terms of the calculated stiffness (K: (N/mm)) are presented as the average ± SD, and grouped in Figure 29.

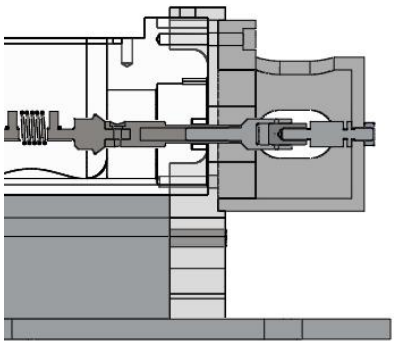

(i) without lateral wall
nominal stiffness,
K=0.057±5.19e-5 N/mm
Calculated stiffness,
K=0.05±8.89e-5 N/mm

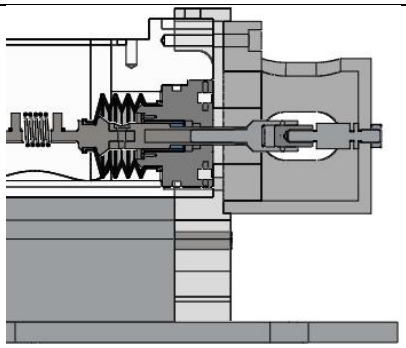

(ii) complete
nominal stiffness,
K=0.057±5.19e-5 N/mm
Calculated stiffness,
K=0.028±5.94e-3 N/mm

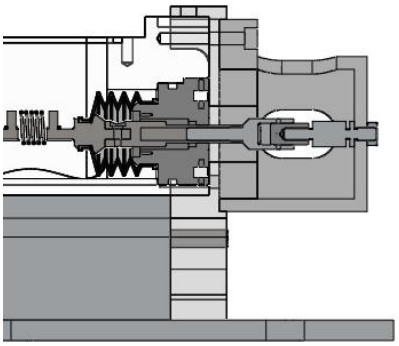

(iii) without bearing

nominal stiffness,

K=0.057±5.19e-5 N/mm

Calculated stiffness,

K=0.052±9.54e-4 N/mm

Figure 29: Characterization test configurations, from top to down: (i) without the later wall, (ii) complete, (iii) without the linear bearing

In the first condition, i.e. the load cell is directly connected to the shaft, the mean stiffness value was: $K_{(i)}$=0.050±8.89e-5 N/mm. Values obtained from the independent tests were overlapping, even if the averaged stiffness is slightly lower than the one calculated with the MTS system.

In the second configuration, i.e. complete configuration, the mean value for the stiffness was: $K_{(ii)}$=0.028±5.94e-3 N/mm. This value is almost the half of the nominal stiffness. Most likely, a misalignment is originated by imperfect coaxiality of the joint which couples the shaft on one side and the load cell on the other side. The bearing is over-constraining the shaft, and consequently, if a misalignment is present a significant friction could follow.

In the third configuration, carried out in the absence of the bearing, the calculated stiffness is: $K_{(iii)}$= 0.052±9.54e-4 N/mm. Tests are

overlapping even if, as already observed in the first test, the mean stiffness is slightly lower than the one calculated with the MTS system.

The presence of the linear bearing showed to over-constrain the shaft. In the absence of the bearing the value found for the stiffness differed at maximum 10% with respect to the real value, thus indicating that the system can be used in this configuration for an indicative evaluation of the cultured construct stiffness even if further modification could be required to increase the sensitivity.

2.3.4 Sterility test and performance in incubator

The bioreactor has been tested for sterility maintenance of the culture unit and the milieu sensors, in (1) static conditions and (2) during dynamic motion within the incubator.

The culture unit elements were previously washed and soaked for 1h. Before sterilization some pieces were preassembled to reduce the contamination risk during the assembling procedure under the hood (the shaft were coupled with the construct holder and inserted within the lateral wall with the bellow wrapping both sides). The chamber, the preassembled later walls, the lid, the lid caps, the luer lock connectors, the compliance tube, the sensors inserts, and inlet tubing were independently packed and sterilized in autoclave (120 $^{\circ}$C, 1h).

Separately, the tip of pH and O_2 sensors was carefully washed in PBS and then immersed in freshly PBS for 20 min. After washing, they were placed in a sterile 120 mm petri dish and underwent to a 20 min

sterilization cycle by UV under the hood. (10 min each side; turned meanwhile and likewise exposed to improve the sterilization process).

After sterilization, the components were transferred under the hood and the culture unit assembled. Then, in sequence the following operations were executed:

- The chamber was filled with standard culture medium (DMEM5671, Sigma-Aldrich). No streptomycin/penicillin was used within the medium to enhance the validity of the test.
- The lid was mounted on top of the culture unit (A sterile filter was used on top of the compliance and a sterile injection site coupled with the inlet tubing).
- The pH and oxygen sensors were inserted within the lid by means of the bayonet fitting inserts. The other two open spots for were closed with the dedicated caps.

The assembly was then transferred within the incubator as shown in Figure 30.

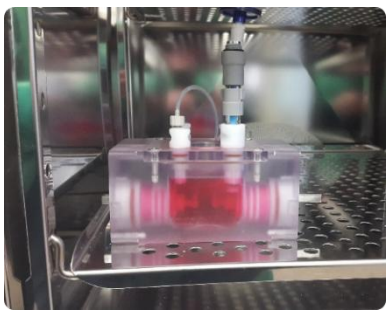

Figure 30: Assembly within the incubator

Each 48 hours 5 mL of medium were sampled by the injection site port with a 10mL sterile syringe and checked: (1) at a glance, to check any colour and/or density changes and, (2) under a standard optical microscope to check the presence of any bacteria or yeasts.

After 5 days the chamber was moved under the hood and the lid removed to check that any contamination or yeasts aggregates were present in the medium bulk neither nearby of the sensors. No medium color change neither viscosity was observed (Figure 31).

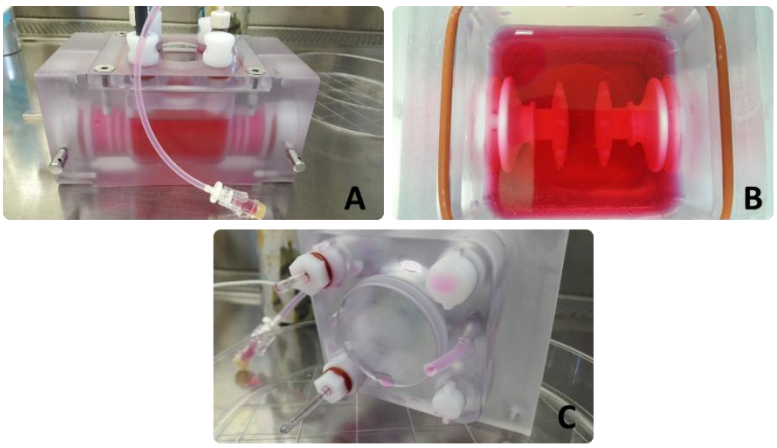

Figure 31: Medium and sensor tip status after sterility test. (A), the culture unit after the culture, (B) culture medium appearance and, (C) detail in nearby of the sensors tip. Any contamination or yeasts aggregates were present in the medium bulk neither nearby of the sensors

To verify the sealing and sterility maintenance under dynamic condition, after 5 days of static culture, the culture unit was mounted on the mechanical framework and connected to the control box; a

sinusoidal displacement of 1,5mm at 1Hz was imparted for 1 day (Figure 32).

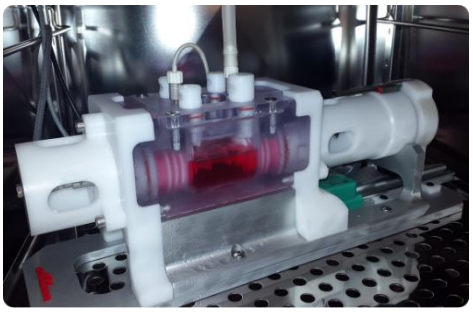

Figure 32: Bioreactor within the incubator during dynamical motion

The chamber was then removed from the chassis and replaced in the incubator up to 10 days. Neither yeasts aggregates nor any other source of contamination were found in the medium bulk or nearby of the sensors.

For what concerns the overall system performance within incubator, the increase of temperature (from environmental 24-27 $^{\circ}$C to 37 $^{\circ}$C) and humidity (from 50-60% to 98/99%) seemed to not affect the performance of the bioreactor. Some condensation drops were observed on the coil after 6 hours of mechanical actuation without any consequence on the motor performance

2.4 Discussions and conclusions

In this chapter the design and development of a novel advanced bioreactor has been presented. The proposed system is meant (1) to deliver native-like or pathologic cyclic strain to thick-relevant engineered cardiac constructs, (2) to assess their mechanical properties during the culture in a non-destructive manner, and (3) to monitor medium parameters in real time. At present, several devices have been developed for this purpose (Birla, Huang and Dennis 2007, Kensah, et al. 2011, Govoni, et al. 2014). However, tissue mechanical properties have never been monitored in combination with physicochemical parameters (Kensah, et al. 2011) and the mechanical stimulation pattern is limited in terms of waveforms, frequency and duty cycle, narrowing the strategies for applying biomimetic culture strategies (Birla, Huang and Dennis 2007). Additionally, current devices do not adapt the stimulation to the actual maturation stage of the tissue, which would turn into the optimization of cardiac muscle-relevant properties (Zimmermann 2013).

The engineering solutions introduced in the design of this new cyclic strain-based bioreactor allow to obtain controllable displacements within physiological/pathological ranges (0.5-20% of strain, 1-6 Hz stimulation frequency). Firstly, the use of the voice coil actuator simplifies the kinematic mechanism to produce the linear displacement. Additionally, the feed-forward loop integrated in the control strategy permits to take into account friction effects due to the mechanical couplings and provides effective mitigation of the dry friction phenomena. The experimental tuning of the actuation control was speeded up by the lumped model developed in Simulink™, and the obtained assessment results show the

suitability of the actuator in following the waveforms imposed by the reference. To guarantee reference tracking in dynamic conditions, an additional mapping gain element was used to adapt the output amplitude to the desired value. At present, the mapping gain was found for a sub selected dynamic working range of the device (0.5-3mm at 1 Hz) which was considered a starting point for a more comprehensive validation. Noteworthy, the control strategy which have been designed is also suitable for a force-based control if a force transducer is used in the control loop in place of the position transducer.

With regards to the sensors for O_2 and pH, characterization procedures have been established and in house tests showed a suitable sensitivity.

The sensing system designed to assess the mechanical properties of the cultured tissues has been evaluated by means of a calibrated instrumentation spring. With the present configuration, the stiffness measured within the bioreactor differed at maximum 10% of the real value, thus indicating that the system can be used for an indicative evaluation of the elastic modulus even if further modification is required to increase the sensitivity.

Finally, the sterility maintenance of the culture unit in its complete configuration, i.e. with the sensors within the culture chamber, was verified in static and dynamic conditions. Contextually, the validity of the sterilization procedure for the O_2 and pH sensors was verified.

Some limitations affect the bioreactor performance in the current configuration. From the mechanical point of view, the coupling between

the actuator and the load, i.e. the engineered tissue, could introduce significant friction which could affect the displacement accuracy. Furthermore, the coupling on the "sensing side", between the load cell and the shaft, could be critical. Indeed, even if the machining tolerances and the correct mounting of the assembly ideally guarantee the correct centering and the absence of any torque, friction due to potential uncontrolled misalignments could be originate by the thermal expansion and shrinkage of the components due to repeated sterilization cycles. Some structural modifications, involving the increase of the gap between sliding elements, i.e. the lateral walls and the shafts, or the design of an alternative coupling method, could actually mitigate the friction effects. Moreover, future modifications could implicate the housing of the force sensor within the culture chamber in order to increase the measurements reliability.

As regards to the control strategy, the hardware used to implement the control strategy presents some limitations. During high speed displacements, processor frequency could be not high enough to close the actuation displacement loop in order to guarantee the Hard Real Time (HRT) determinism. A future solution could be to separate the monitoring of the sensors (which have a slower dynamic) from the actuation control, by using two dedicated modules.

In addition, the off-line characterization of the friction (which is taken into account with the feed-forward loop) could be subjected to errors as far as the test conditions are significantly changing (e.g. humidity, increase of temperature, thermal dilatation of the components). In this

case, the implementation of an adaptive control strategy could overcome this limitation.

Although these limitations, the developed bioreactor represents a valuable proof of concept capable, in its most advanced operational mode, to culture engineered cardiac constructs with a biomimetic approach, by monitoring both their mechanical properties and the most relevant culture parameters during the culture, and by providing native-like/pathologic cyclic stretch stimulation. Furthermore, the adopted hardware and software architecture will allow in the future the implementation of an adaptive stimulation protocol in order to train the cultured constructs on the basis of their actual maturation stage.

Acknowledgements

The author would like to thank Prof. Tonoli and Dr. Renato Galluzzi (Department of Mechanical and Aerospace Engineering, Politecnico di Torino, Italy) for the contribution in developing the actuation control architecture and Ing. Andres Rodriguez (Bioindustrial Engineering group, Department of Mechanical and Aerospace Engineering, Politecnico di Torino, Italy) for the development of the software.

References

Armostrong-Hélouvry, B. "Control of Machines with Friction." (Academic Publishers) 1991.

Bilodeau, K., and D. Mantovani. "Bioreactors for tissue engineering: focus on mechanical constraints. A comparative review." *Tissue Engineering* 12, no. 8 (2006): 2367-2383.

Birla, R.K., Y.C. Huang, and R.G. Dennis. "Development of a novel bioreactor for the mechanical loading of tissue-engineered heart muscle." *Tissue Engineering* 13, no. 9 (2007): 2239-48.

Carrier, R.L., et al. "Cardiac tissue engineering: cell seeding, cultivation parameters, and tissue construct characterization." *Biotechnol Bioeng* 64, no. 5 (1999): 580-9.

De Rossi, D., A Ahluwalia, A. Mazzoldi, D. Pede, and EP. Scilingo. *Sensori per misure biomediche.* Patron Editore, 2004.

Govoni, M., et al. "An innovative stand-alone bioreactor for the highly reproducible transfer of cyclic mechanical stretch to stem cells cultured in a 3D scaffold." *J Tissue Eng Regen Med* 8, no. 10 (2014): 787-93.

Hirt, M.N., A. Hansen, and T. Eshenhagen. "Cardiac Tissue Engineering: State of the Art." *Circulation Research* 114, no. 2 (2014): 354-67.

Hryniewicz, T., K. Rokosz, and M. Filippi. "Biomaterial Studies on AISI 316L Stainless Steel after Magnetoelectropolishing." *Materials*, no. 2 (2009): 129-145.

Kensah, G., et al. "A novel miniaturized multimodal bioreactor for continuous in situ assessment of bioartificial cardiac tissue during stimulation and maturation." *Tissue Eng Part C* 17, no. 4 (2011): 463-73.

Korossis, SA., F. Bolland, JN. Kearney, J. Fisher, and E. Ingham. *Bioreactors in Tissue Engineering.* Vol. 2, in *Topics in Tissue Engineering*. N. Ashammakhi & R.L. Reis, 2005.

Mantero, S., N. Sadr, SA. Riboldi, S. Lorenzoni, and FM. Montevecchi. "A new electro-mechanical bioreactor for soft tissue engineering." *Journal of Applied Biomaterial and Biomechanics* 2, no. 5 (2007): 107-116.

Ogata, K. *Modern Control Engineering.* Fifth Edition. NY, USA: Prentice Hall, 2010.

Partap, S., NA. Plunkett, and FJ. O'Brien. "Bioreactors in Tissue Engineering." Chap. 6 in *Tissue Engineering*. 2004.

Radisic, M., H. Park, S. Gerecht, C. Cannizzaro, R. Langer, and G. Vunjak-Novakovic. "Biomimetic approach to cardiac tissue engineering." *Philos Trans R Soc Lond B Biol Sci* 362, no. 1484 (2007): 1357–1368.

Salazar, B.H., A.T. Cashion, R.G. Dennis, and R.K. Birla. "Development of a Cyclic Strain Bioreactor for Mechanical Enhancement and Assessment of Bioengineered Myocardial Constructs." *Cardiovasc Eng Technol.* 6, no. 4 (2015): 533-45.

Visioli, A. "Modified anti-windup scheme for PID controllers." *Control Theory and Applications.* IEEE Proceedings, 2003. 49-54.

Vunjak-Novakovic, G., et al. "Challenges in cardiac tissue engineering." *Tissue Eng Part B* 16, no. 2 (2010): 169-87.

Zimmermann, W.H. "Biomechanical regulation of in vitro cardiogenesis for tissue-engineered heart repair." *Stem Cell Research & Therapy* 4, no. 137 (2013).

Appendix

Current, position and feed-forward loop compensator design

As already mentioned in Chapter II, the voice coil actuator can be represented with the following differential equations:

$$V = L\frac{di}{dt} + Ri + K_e v \qquad \text{Eq. 1}$$

$$K_\mathrm{f} i = m\frac{\mathrm{d}v}{\mathrm{d}t} + cv + F \qquad \text{Eq. 2}$$

Eq. 1 describes the electromagnetic behaviour of the device dependant on the resistance R, the inductance L and the back electromotive force (EMF) constant K_e. The related variables are the input voltage V, the winding current i and the stroke speed of the moving parts v. Eq. 2 governs the electromechanical dynamics of the system, where an input force is proportional to the current i by a force constant K_f. The latter is filtered by the mechanical lumped parameters, i.e. the mass of the moving parts m and the friction losses, which, in this case, are represented as purely viscous with a damping c. Finally, the output force exerted to the probe is F.

A conventional cascade feedback loop control architecture has been implemented to produce accurate and controllable displacement of the voice coil linear actuator. Indeed, an inner current feedback loop sets the

current, which is proportional to the force by a force constant $K_{f.}$, while the outer loop sets the position. Furthermore, a feed-forward loop is used to reduce friction effects. Scheme of Figure 1 summarizes the feedback loop control architecture.

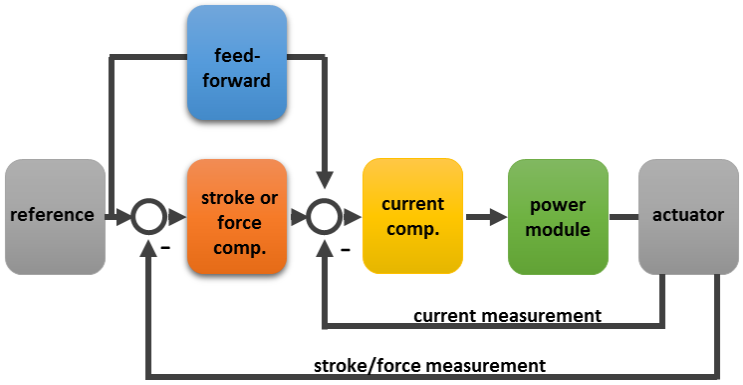

Figure 1: Cascade control architecture and feed-forward control loop

The inner loop: current compensator design

The inner loop has been designed as a Proportional-Integral (PI) compensator. It can be tuned following an analytic approach where the integral time constant is used to cancel the electromagnetic pole of the voice coil actuator. In particular, the transfer function between voltage and current is simply:

$$G_{\mathrm{i}}(s) = \frac{i(s)}{V(s)} = \frac{1}{sL+R} \qquad \text{Eq. 3}$$

Note that the stroke speed is considered as a disturbance in this case. In other words, the Eq. 3 transfer function indicates short-circuit operation. The compensator transfer function is:

$$C_{\mathrm{i}}(s) = K_{\mathrm{p,i}}\left(1 + \frac{1}{s\tau_{\mathrm{i,i}}}\right) \qquad \text{Eq. 4}$$

being $K_{\mathrm{p,i}}$ the proportional gain of the PI controller and $\tau_{\mathrm{i,i}}$ the time constant. The closed-loop transfer function assuming a current feedback on the plant $G_{\mathrm{i}}(s)$ and a current reference i_{ref} is:

$$F_{\mathrm{i}}(s) = \frac{i(s)}{i_{\mathrm{ref}}(s)} = \frac{G_{\mathrm{i}}(s)C_{\mathrm{i}}(s)}{1+G_{\mathrm{i}}(s)C_{\mathrm{i}}(s)} = \frac{K_{\mathrm{p,i}}\left(1+s\tau_{\mathrm{i,i}}\right)}{s\tau_{\mathrm{i,i}}(sL+R)+K_{\mathrm{p,i}}\left(1+s\tau_{\mathrm{i,i}}\right)} \qquad \text{Eq. 5}$$

Choosing $\tau_{\mathrm{i,i}} = L/R$ leads to the following simplification:

$$F_{\mathrm{i}}(s) = \frac{1}{s\frac{L}{K_{\mathrm{p,i}}}+1} \qquad \text{Eq. 6}$$

The latter transfer function exhibits a first-order behaviour with unitary static gain. The frequency of its pole denotes the bandwidth of the controlled system. Thus, to achieve a particular actuation frequency, the proportional gain can be tuned according to

$$K_{\mathrm{p,i}} = 2\pi f_{\mathrm{i}} L \qquad \text{Eq. 7}$$

where f_{i} is the bandwidth frequency of interest.

The outer loop: position compensator design

Considering the force as an ideal input of the system (which is a valid assumption if the current loop, i.e. the inner loop, is tuned correctly and the actuator is working within the bandwidth) the transfer function between force and position is simply:

$$G_q(s) = \frac{q(s)}{F(s)} = \frac{1}{ms^2+cs+k} \qquad \text{Eq. 8}$$

Consider a generic Proportional-Integral-Derivative (PID) compensator $C_{\mathrm{q}}(s)$ with transfer function:

$$C_{\mathrm{q}}(s) = K_{\mathrm{p,q}}\left(1 + \frac{1}{s\tau_{\mathrm{i,q}}} + s\tau_{\mathrm{d,q}}\right) \qquad \text{Eq. 9}$$

being $K_{\mathrm{p,q}}$ its proportional gain, and $\tau_{\mathrm{i,q}}$, $\tau_{\mathrm{d,q}}$ the time constants due to the integral and derivative actions, respectively. The closed-loop transfer function, assuming a position feedback on the plant $G_q(s)$ and a reference position q_{ref}, is:

$$F_i(s) = \frac{q(s)}{q_{\mathrm{ref}}(s)} = \frac{G_{\mathrm{q}}(s)C_{\mathrm{q}}(s)}{1+G_{\mathrm{q}}(s)C_{\mathrm{q}}(s)} \qquad \text{Eq. 10}$$

The position compensator was tuned using Simulink Control Design™ toolbox. PID gains were selected by observing the rise time, the settling time and the maximum overshoot of the closed-loop step response in the time domain, and the gain and phase margin of the loop function in the frequency domain. These values, which are inherent of classic control design methods (Ogata, 2010), are made available through

the tuning procedure inside Simulink Control Design™ as the control gains are modified.

The feed-forward loop: friction compensation

A feed-forward loop has been implemented to reduce friction effects according to the scheme of Figure 1. In this case, the goal was to use a non-linear law that determines the sign of the stroke rate and yields a constant contribution of force F_0 in correspondence to the sense of motion:

$$F_{\mathrm{ff}} = F_0 \cdot \mathrm{sign}\big(sq_{\mathrm{ref}}(s)\big) \qquad \text{Eq. 11}$$

This action provides effective mitigation of the dry friction phenomena that take place from the contact between moving parts (Armostrong-Hélouvry, 1991).

Sensors characterization procedures and assessment

Different method of characterization for the sensors have been preliminary tested and the most suitable selected, then, for each sensor, a specific calibration protocol has been developed according to its the physical principle and to the manufacturer indications.

pH sensor calibration procedure

The pH InLabUltraMicro (Mettler Toledo, ZH, Switzerland) sensor is a combined electrode where the pH-sensitive glass electrode is concentrically surrounded by the reference electrode filled with reference electrolyte. Generally, the pH sensor is a glass electrode and its working principle is based on Nernst equation:

$$E = \frac{RT}{nF} log \frac{C_1}{C_2}$$

Where:

- E: Output voltage (mV)
- R: Universal gas constant ($8.31439 \frac{J}{mol\,K}$)
- T: Temperature (K)
- F: Faraday constant ($96495.7 \frac{C}{mol}$)
- n: charge of measured ion (in this case n=1)
- C1: active ion concentration in solution 1
- C2: active ion concentration in solution 2

The potential E, that is generated between two platinum electrodes, the pH electrode and the reference electrode, is a linear function of the hydrogen concentration in the solution which, by definition, gives the pH value. The pH electrode is the part that actually senses the pH in the solution. It consists of a glass shaft with a thin glass membrane at the end, sensitive to H+ ions. The purpose of the reference electrode, instead, is to provide a defined stable reference potential for the pH sensor potential to be measured against. Sensor characteristics are reported in the section Hardware datasheet.

In order to achieve the best accuracy, a standard three point calibration method was considered the most appropriate for the InLabUltraMicro (Mettler Toledo, ZH, Switzerland) pH sensor. In addition, given the narrow range in which the measurements could lie (the pH value of the culture medium it is supposed to be approximately around 7,2-7,4), and to best mimic the working conditions for the sensor a specific validation test was designed. The changes of the solution pH were generated adding an acid or a base starting from a solution at pH 7.0. These measurements were carried out also with the Hamilton pH sensor (Hamilton, USA) which possess nominal comparable characteristics with InLabUltraMicro.

(A) Standard three points calibration

The calibration of the pH sensor is done by using different buffer solutions (pH 7, pH 4,01 and pH 9,21 at 20 ° C, FLUKA, Sigma-Aldrich, USA) with known and stable pH value. The first buffer sets the zero point, the second sets the slope and the calibration over the entire

measuring range has to be verified by means of the third buffer solution. In the ideal conditions, at 37 $^{\circ}$C the sensor sensitivity should be of -61.46 mV/pH and show a linear characteristic in the range 0-10pH.

Prior to calibration, an inspection procedure on the sensor is needful. The sensor was cleaned with double distilled water and a cotton pads, then the electrolyte level inside the electrode and the presence of bubbles in the liquid were verified. Potential bubbles inside the electrolyte were removed by shaking the sensor in the vertical plane. After the inspection, the calibration procedure, described in detail in Figure 2 starts by inserting the sensor first into the solution with pH 4,01, then into solution with pH 7 and finally in the solution with pH 9,21. An amount of 15 ml of the buffer solution within each 50 ml falcon is enough for the tip of the sensor to be completely immersed.

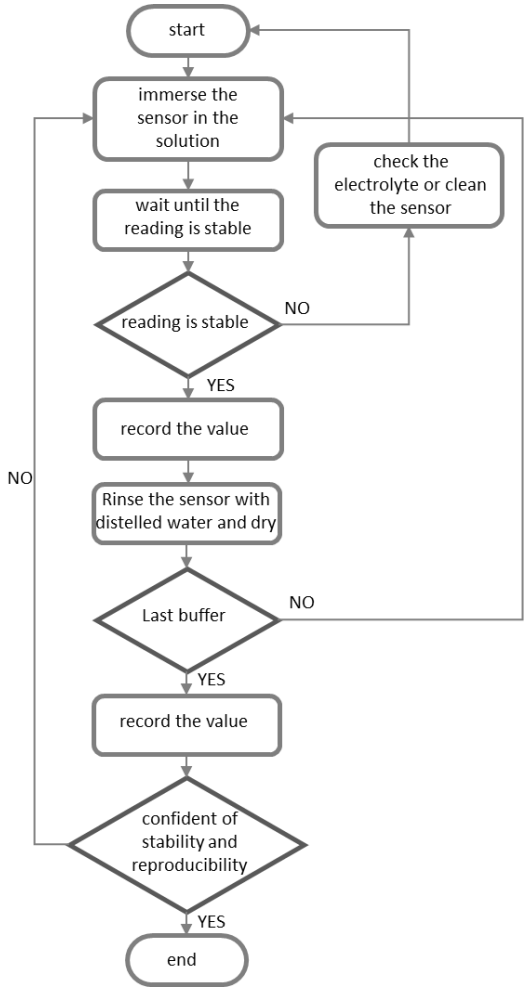

Figure 2: pH sensor calibration flow chart

Three independent measurement sessions were realized, and five records for each of the three pH buffer points were collected. A linear regression of the averaged values has been calculated for sensor sensitivity and offset. Measures are the mean value of 100 points of the digitalized signal. For each experimental session, the time constant was

found to be around 5 minute, i.e. the time needed to reach a certain stability in the output voltage. The temperature was monitored all along the test by means of a digital thermometer and remained constant at 26 ˚ C. Values of the calibration and theoretical curves in terms of sensor sensitivity (mV/pH) and offset (mV) are reported in Table 1 and plotted in Figure 3.

Table 1: pH-meter sensitivity and offset: theoretical vs experimental

	Slope (mV/pH)	Offset (mV)	T (˚ C)
Experimental	-50,65	343,38	26
Theoretical	-61,46	430,25	37

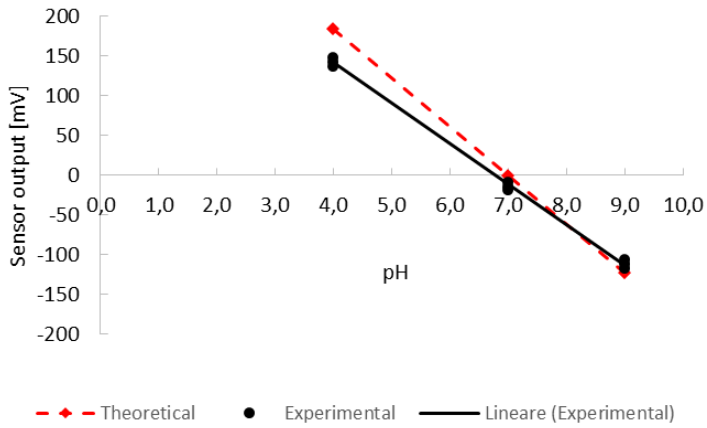

Figure 3: pH calibration curves: theoretical vs experimental

(B) Validation Test: small changes in the interval 6.0-8.0 pH and comparison with Hamilton sensor

Starting from a pH 7 solution (FLUKA 33643, Sigma-Aldrich, USA) an acid solution (HCl 1M) or a base (NaOH 1M) were added to the solution to test the sensitivity of the sensor to the pH increase or decrease. The Hamilton pH sensor and XSm pH-meter (Hamilton, USA) were used in this test to compare the results. Both the sensors were calibrated before to run the test.

Several trials were carried out before to define the amount of acid or base to add at each step. For the pH decrease, 30µl of HCl 1 M acid were added with a 200 µl pipette in the solution at pH 7 (40 ml) and the mixture put under stirring for 3 minutes. In the following steps, the amount was increased up to 70 µl. The pH value was then measured with both the sensors. Similarly, for the pH increase 80µl of NaOH 1 M were added in the solution at pH 7 (40 ml) and the mixture put under stirring for 3 minutes. Also in this case the pH was measured with both the sensors. The temperature was monitored all along the test by means of a digital thermometer and remained constant at 26 ° C. The number of the measures was not fixed *a priori* but chosen accordingly the reaching of a variation in the desired range. Values of the calibration in terms of sensors sensitivity (mV/pH) and offset (mV) are reported in Table 2. The sensors behaviour is graphed in Figure 4.

Table 2: InLabUltramicro pH-meter sensitivity and offset

	Slope (mV/pH)	Offset (mV)
Decrease test	-50,47	346,60
Increase test	-49,95	343,30

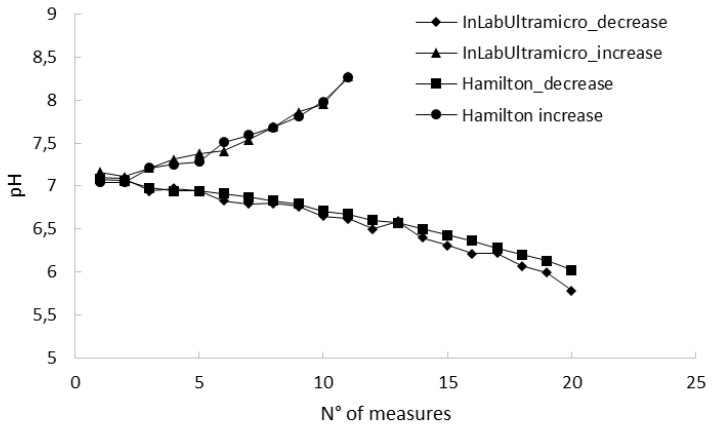

Figure 4: Curves from InLabUltramicro and Hamilton ph-meters for decrease and increase tests

The changes in pH of the solution, generated adding an acid or a base starting from a solution at pH 7.0 are closely followed. Indeed, the InLabUltramicro pH meter shows a good sensitivity for small variation of the pH. The agreement between the two sensors was evaluated by means of the Bland-Altman plot, which graphs the difference between the two measurements, i.e. variations measured with the two sensors, vs their average. Bland and Altman plots are extensively used to evaluate the agreement among two different instruments or two measurements techniques and helps in seeing discrepancies between the measurements from the two sensors.

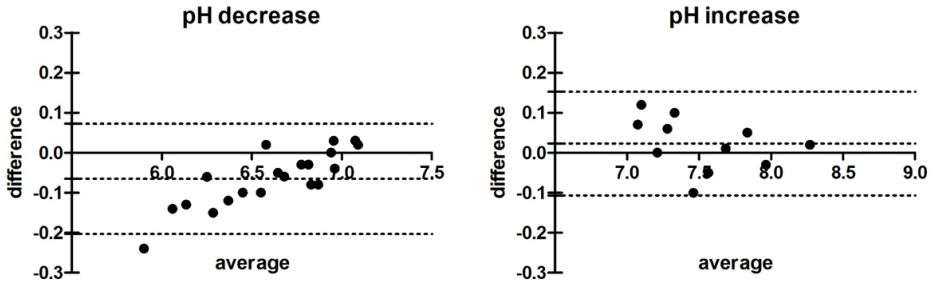

Figure 5: Bland-Altman graphs of variations measured with the two sensors, vs their average

The Bland-Altman graphs shows good agreement between the measuremenst. Differences among the measurements of the two instruments, except one, lies within the 95% limits of agreement, which are reported in the graph. The results from the test validate the sensor confirming its suitability in monitoring small changes of the pH within the culture medium.

O2 sensor characterization procedure

The O2 MI-730 Micro-Oxygen Electrode (Microelectrodes Inc., NH, USA) is a Clark cell, an electrochemical sensor commonly used for oxygen concentration measurements in biological fluids or water. The current produced by the redox reaction that develops inside the electrode is directly proportional to the partial pressure of oxygen. According to the datasheet (see the section Hardware datasheet), a liner relationship between input concentration of O2 and output current can be assumed. The sensor measures 1700 pA in air at 25 $^{\circ}$C; the expected current values in the bioreactor's culture chamber (@ 37 $^{\circ}$C) in a range of pO2

concentrations of 0,5-100% are respectively 59-1768 pA. (Microelectrodes). Given the phenomena dynamics, is reasonable to assume that the bandwidth of the output signal lies between 0 and 2 Hz (De Rossi, et al., 2004). Besides an adapter is used to convert the output current from the sensor in an analogical tension signal (1mV/5 pA input).

A two-point calibration method seemed the most appropriate for the O2 MI-730 sensor (Microelectrodes Inc, USA) This method, according to the manufacturer indications, requires the use of two standard gases with percent values close to those of Oxygen to be measured. Common values used are 0% Oxygen for zeroing and 21% Oxygen (Ambient Air) for sloping or gain.

Two Lightcyl-large bottles (Siad, BG, Italy) of sample gases were used. The bottles (1,6l, 40 bar) are composed respectively by: 3 or 18.8% of O2, 5 or 10% of CO2 and Nitrogen for the remaining volume (percentages are expressed with respect to the total volume). A pressure reducer for disposable bottles was also furnished to distribute the gases at an adjustable pressure.

Before proceeding with calibration, the sensor were prepared, by checking the electrolyte level where the electrode is immersed (according to the datasheet it should have a minimum height of 6 mm), the absence of trapped bubbles near the electrode tip and the external membrane status.

To decrease the calibration time, two separate calibration chambers filled with double distilled water (12 ml) were prepared, one for the 3%

and another for the sloping gas such as 18.8% of Oxygen. To set up the calibration chambers, gases were flushed for 30 minutes in each chamber to obtain a steady state oxygen level. The bubbling rate was carefully regulated (3 - 6 bubbles per second). Care was devoted to monitor the temperature. The calibration procedure is described in detail in Figure 6.

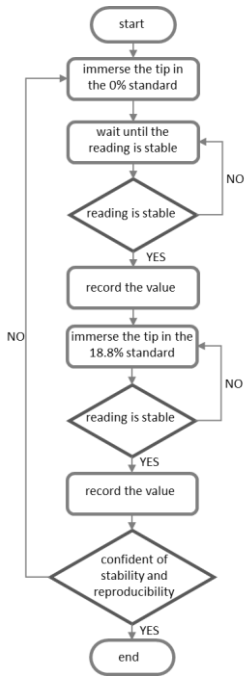

Figure 6: O_2 sensor calibration flow chart

The calibration data were calculated on the values obtained from three independent experimental session. A linear regression of the averaged values has been calculated for sensor sensitivity and offset. Each measure is the mean value of 100 points of the digitalized signal.

The temperature was monitored all along the test by means of a digital thermometer and remained constant at 26 ° C. Values of the calibration and theoretical curves in terms of sensor sensitivity (mV/%O_2) and offset (mV) are reported in Table 3 and plotted in Figure 7

Table 3: Oxygen sensor sensitivity and offset: theoretical vs experimental

	Slope (mV/%O_2)	Offset (mV)	T (° C)
Experimental	13.06	2.49	26
Theoretical	16.19	0.00	37

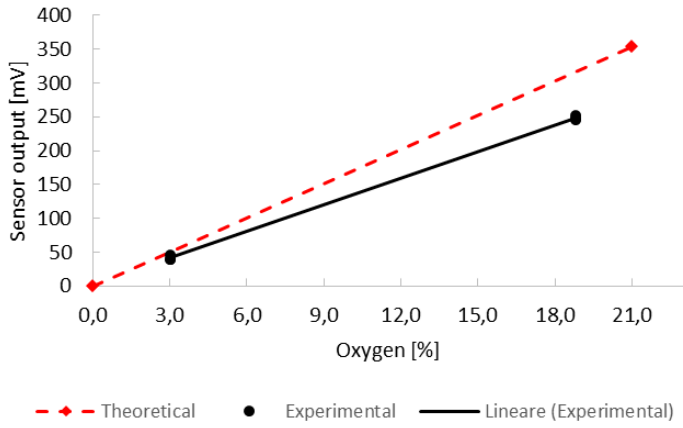

Figure 7: Oxygen sensor calibration curves: theoretical vs experimental

The time constant was determined as the temporal difference from the immersion of the sensor tip into the sample gases and the reaching of the steady state. The signal was considered stable when the standard deviation of the averaged values was lower than 2.5mV, which corresponds, considering the slope of the calibration curve, to 0.2% of

Oxygen. Signals are obtained from three independent experimental session. Figure 8 shows the averaged signal value

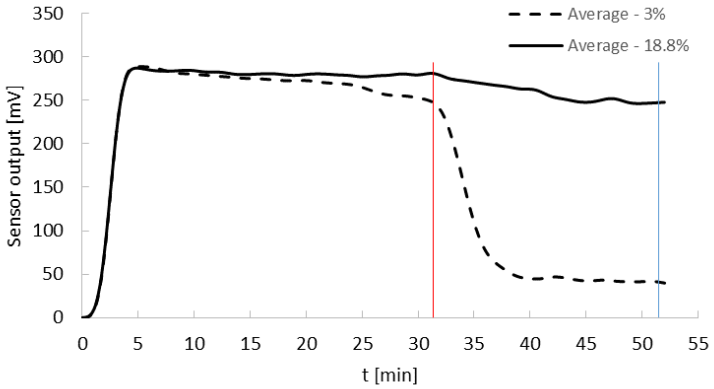

Figure 8: Averaged value of the Oxygen sensor signal

The sensor is inserted in the calibration chamber, respectively 3% and 18.8% when indicated by the red line, i.e. after 30 min of bubbling of the gases within the chambers. The blue line indicates the reaching of steady value which corresponds to a time constant of 30 min.

Load cell calibration procedure and assessment

The load cell chosen is a XFTC300-S109 (Measurement Specialties, VA, USA) 10N full scale range force sensor. The cell measures tension and/or compression in static and dynamic applications. The sensing element is fitted with a fully temperature compensated Wheatstone bridge equipped with high stability micro-machined silicon strain gages. A signal conditioner, ARD154 (Measurement Specialties, VA, USA), boosts the signal level and increases measurement resolution also

improving signal-to-noise ratio. The bridge supply voltage it set on ffi10V analogue output with a sensitivity of 30mV/V. It allows to adjust the zero and the gain and to filter the signal within a defined bandwidth. A detailed description of the sensor and its conditioner is reported at the end of the Appendix.

According to the ANSI/ISA (1979) standard, the procedure for the load cell calibration is a static process were the system is used to make measurements of known reference values of the measurand, i.e. known weights (it is static because time is not a factor, the measuring system is allowed to reach the equilibrium prior to take a reading). The measurand values are incrementally increased from the low end of the range to the top end; then incrementally reduced to the low end; and the process repeated several times. That procedure furnishes linearity, hysteresis, repeatability, overall accuracy, maximum systematic and random errors parameters to complete characterize the sensor but it is not required to be executed on a regular base. Indeed, the load cell was chosen according to these characteristics and already calibrated by the manufacturer and a single test with 5 calibrated weights (20g, 50g, 100g, 200g, 500g) seemed satisfactory for the purpose. That allowed to estimate the sensitivity and the DC offset of the signal. Values of the calibration and theoretical curves in terms of sensor sensitivity (mV/mN) and offset (mV) are reported in Table 4 and plotted in Figure 9.

Table 4: Load cell sensitivity and offset: theoretical vs experimental

	Slope (mV/mN)	Offset (mV)
Experimental	0.51	24.54
Theoretical	0.50	0.00

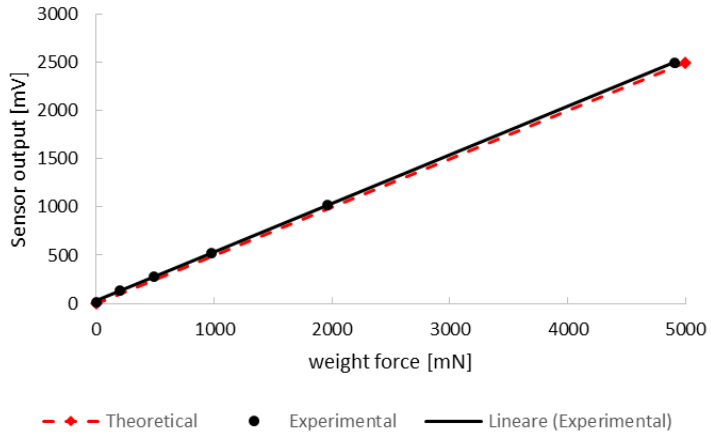

Figure 9: Load cell calibration curves: theoretical vs experimental

In the following, the datasheet of the pH, O_2, load cell sensors, voice coil motor and the linear transducer are reported. Lastly, a brief description of the National Instruments hardware is given and a datasheet for the most relevant characteristics is included.

GVCM-051-064-01 linear voice coil and ONP1A linear position transducer

DEVICE	PARAMETER	VALUE
	continuous force	32,9 N
	force constant	9,6 N/A
	back EMF constant	9,6 V/M/S
	stroke	31,8 mm
	coil resistance	3,9 Ohms
	coil inductance @ 1000Hz	1,6 mH
	max continuous power	36 W
	linear bearing type	recirculating balls
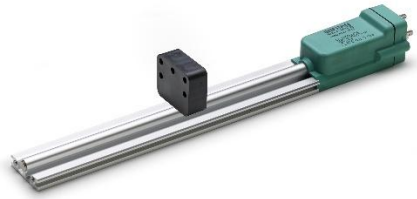	measurand	displacement
	max acceleration	100 m/s2
	resolution	Infinite
	working temperature	-20 +75 ° C
	coefficient of temperature	≤0,01% fs/ ° C
	output signal	0,1-10,1 V
	nominal power supply	24±20%
	output load	≥10 KΩ
	protection	IP65
	max stroke	50 mm

InLabUltraMicro pH sensor

DEVICE	PARAMETER	VALUE
	type of sensor	pH Glass electrode
	reference electrodes type	Ag-AgCl
	type of measure	Invasive
	dimensions	Shaft diameter: 3 mm Shaft length:40 mm
	sterilization	UV
	Output	Voltage
	measure range	From 0 to 11 pH
	zero point	7 ±0.25 pH
	slope	-58.16 mV at 25 ° C

O2MI-730 Micro-Oxygen Electrode sensor and O2-ADAPT Oxygen Adapter

DEVICE	PARAMETER	VALUE
	type of sensor	Clark cell
	reference electrode type	Ag
	type of measure	Invasive
	depth of immersion	0.1 mm
	dimensions	Body and tip: 3mm Total length: 86 mm Lead length: 2 m
	sterilization	UV sterilizable
	Output	Current
	response range	0 to 100%
	sensitivity	1700 pA in air at 25flC
	response time	20 s
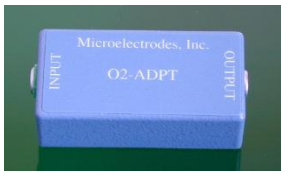	size	28.5 mm x 22.4 mm x 58 mm
	output	1mV/5 pA Input
	connectors	LEMO 00.250

XFTC300-S10 Load cell and ARD154 signal conditioning system

DEVICE	PARAMETER	VALUE
	full scale range	0-10N
	resolution	Infinite
	excitation	10Vdc
	signal output	100mV
	offset	≤ ±10mV
	linearity + hysteresis	≤ ±0,5%FS
	operating temperature	-40 ° C to +120 ° C
	Compensation temperature	0 ° to 60 ° C
	cable output	2m of Ø2mm Teflon jacket cable
	input voltage	24 Vdc
	bridge impedance	120-1000Ω
	bridge excitation	5Vor 10V
	Adjustable sensitivity range	0,1 to 30mV/V
	Calibration push-button	0,1 to 10mV/V
	Accuracy	0.01% FS

cRIO-9075 Integrated 400 MHz Real-Time Controller and LX25 FPGA

The cRIO-9075 integrated system combines a real-time processor for deterministic processes and a reconfigurable Field Programmable Gate Array (FPGA) within the same chassis for embedded machine control and monitoring applications. It integrates a 400 MHz real-time processor with an FPGA and has four slots for NI C Series I/O modules. Details are reported in Table 5.

Table 5: NI cRIO-9075 real-time controller characteristics

DEVICE	PARAMETER	VALUE
	Product family	Real time controller
	Number of Slots	4
	Integrated Controller	400 MHz real-time
	Input Voltage Range	9 V - 30 V
	Power Consumption	15 W
	FPGA	Spartan-6 LX25

NI 9219, Universal Analog Input Module

The NI 9219 is a 4-channel module designed for measuring several signals from sensors such as strain gages, resistance temperature detectors (RTDs), thermocouples, load cells, and other powered sensors. It can be embedded in the CompactRIO chassis. The channels are individually selectable, in order to perform a different measurement type

on each of the four channels. Measurement ranges differ for each type of measurement and include up to 60 V for voltage and 25 mA for current. Details are reported in Table 6.

Table 6: NI 9219 signal acquisition module characteristics

DEVICE	PARAMETER	VALUE
	Product family	I/O signal conditioning
	Measurement Type	Current, Voltage, RTD
	Sampling frequency	100S/s/ch
	Differential channels	4
	Analog input resolution	24 bits
	Accuracy	271 μV
	Range	-0.125 V - 0.125 V

NI 9505 Full H-Bridge Brushed DC Servo Drive Module

The NI 9505 C module for NI CompactRIO is a full H-bridge servo motor drive for direct connectivity to actuators such as fractional horsepower brushed DC servo motors, relays, lamps, solenoids, and valves. The configurability and performance of the field programmable gate array (FPGA), make it suitable for creating intelligent and efficient control systems using the NI LabView® graphical system design platform. The NI 9505 delivers continuous current of up to 5 A at 40 ˚C (or 1 A at 70 ˚C) at 30 V. Details are reported in Table 7.

Table 7: NI 9505 power stage module characteristics

DEVICE	PARAMETER	VALUE
	Product family	Motion Drive
	Inductance Range	500 `H - 1000 mH
	Quadrature / Incremental Interface	Direct Connect
	Maximum quadrature frequency	5 MHz
	Continuous current	5 A

Chapter 3

Effects of cyclic strain on maturation, contractility and mechanical properties of Engineered Cardiac Tissues. A proof of concept.

3.1 Introduction

In the past years, significant advancements were made in the generation of 3D Engineered Cardiac Tissues (ECT) used as functional *in vitro* models for drug screening or investigating fundamental mechanisms (Vunjak-Novakovic, et al., 2014; Hirt, et al., 2014). These so far experiences collectively suggest that the use of suitable scaffolds as support for cells and the application of physiological physical signals (e.g. electrical and mechanical stimuli) are instrumental in achieving the appropriate structural rearrangement and maturation of the cardiac neo-tissue (Vunjak-Novakovic, Tandon, et al. 2010, W. Zimmermann, 2013).

Many types of biomaterials have been investigated for cardiac engineering, from synthetic to natural ones, resembling some key component of the native extracellular matrix (Govoni, et al., 2013). Among all the investigated materials, numerous advantages have been highlighted for the use of hydrogels, which allow a high seeding efficiency and homogenous cell distribution by gelation entrapment, eventually minimizing loss of cells. (Jockenhoevel, et al., 2001).

In particular, fibrin gels have some advantages over other hydrogel types, such as been easy to be injected, tunable for stiffness and structure, biocompatible, FDA approved and already widely use in the clinic routine. Moreover, the timing of the reaction can be easily adjusted by altering the ratio of thrombin to fibrinogen or the ratio of calcium to thrombin allowing the creation of various geometries. (Yuan, et al., 2011). Polymerisation and degradation of the fibrin gel is manageable and can be tuned to the tissue development by using of the protease inhibitors, such as aprotinin and tranexamic acid (Cholewinski, et al., 2009). Besides, the compact cell-seeded structure that results from gelation provides an adequate hardness for mechanical loading (Mol, et al., 2005).

Improved cardiac tissue structure and higher force development have been observed in fibrin based engineered constructs that were exposed to cyclic stretch by motorized stretching devices (Birla, et al., 2007; Morgan & Black III, 2014; Salazar, et al., 2015) or those cultured in auxotonic conditions (Hansen, et al., 2010). To this purpose, several bioreactors have been developed and used to provide controlled mechanical stimulation during culture in order to promote the

development of cardiac engineered constructs and address their phenotype. (Akhyari, et al., 2002 ; Birla, et al., 2007; Morgan & Black III, 2014; Salazar, et al., 2015). Yet, the optimal mechanical stimulation strategy has not been extensively explored (Salazar, et al., 2015). Indeed, most of the culture platforms were meant to passively apply a time-constant or variable stimulus predefined by the user regardless of the continuous changes of the maturing ECT during the time of *in vitro* culture.

In the previous chapter we described a novel bioreactor design, capable in its most advanced operational mode to (i) apply native-like or pathologic stimuli (namely cyclic strain), (ii) monitor in real-time both the milieu parameters (e.g. oxygen tension, pH) and the progress in mechanical stiffness of the mm-scale ECT, eventually adapting the stimulation to their actual maturation stage.

As a proof of concept and towards the final validation of the bioreactor potential we first assessed its feasibility in generating functional and mature ECT. To this purpose, fibrin-based, ring shaped ECTs were generated and cultured within the bioreactor. The effects of cyclic strain on the maturation, alignment, modification on the elastic properties and contractility of ECTs were assessed by means of histologic assessments, mechanical testing and response to external electrical pacing along the culture.

3.2 Material and Methods

The bioreactor based platform (described in detail in Chapter II) has been tested for suitability in culturing and delivering mechanical cyclical stimulation to 3D fibrin-based, ring shaped ECT. As summarized by the schematic experimental outline (Figure 1), neonatal rat cardiomyocytes were embedded in a fibrin gel and the so generated constructs were pre-cultured for 5 days in static condition and transferred into the bioreactor to be subjected to cyclic mechanical stimulation for additional 4 days (10% strain at 1 Hz). In parallel, control engineered ring-tissues were cultured statically for 9 days. Tissue organization, composition, maturation, mechanical and electrical functionality were assessed at different time culture points.

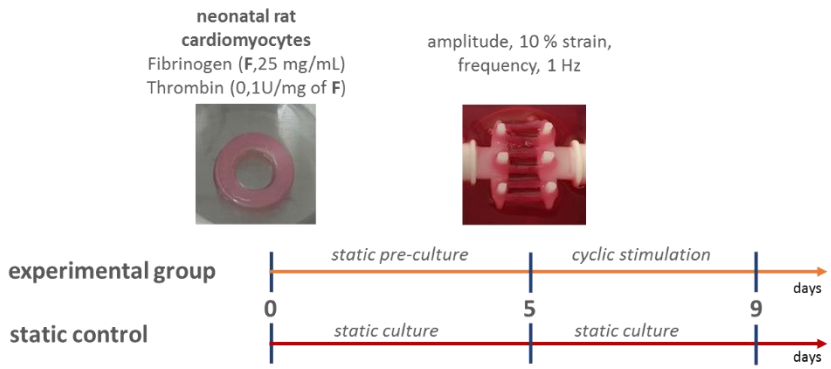

Figure 1 – Outline of the experimental plan

3.2.1 Generation of fibrin-based cardiac tissues (ECTs)

Freshly isolated neonatal rat cardiomyocytes were embedded in a fibrin gel at a density of $18x10^6$ cells/ml (Vunjak-Novakovic, et al.,

2010); 23.0 µl[1] of aprotinin (3000 KIU/mL, Sigma) (Centola, et al., 2013) and 115.7 µl of $CaCl_2$ (40mM) (Cholewinski, et al., 2009) were mixed with 10 µl of thrombin (2.5U/mL final, or 0.1 U/mL thrombin solution per mg fibrinogen, Sigma) (Centola, et al., 2013; Hansen, et al., 2010; Morgan & Black III, 2014) and the solution was transferred into a custom silicone mold (Figure 2A), able to cast up to three ring shaped constructs (ring dimension: external diameter = 16 mm, internal diameter = 10 mm, height = 3 mm, approximately equivalent to a 400 µL of solution). In parallel, the cells were suspended in 150 µl of high glucose (4.5 g/L) culture medium (DMEM), supplemented by 1% FBS, 1% Pen/Strep, 1% L-glutamine, 1% Hepes and mixed with 99.5 µl of fibrinogen (25 mg/mL, Sigma) (Hansen, et al., 2010; Morgan & Black III, 2014). Hydrogels were obtained by pouring the cell-fibrinogen solution within the mold, already containing the thrombin mix (Hansen, et al., 2010). After complete hydrogel polymerization during incubation at 37 ° C for 45 minutes, the rings were removed from the molds, placed into a 6 well plates (Figure 2B) and 4ml/well culture medium was added and incubated again in 37 ° C, 5% CO_2 and 21% O_2 humidified incubator.

[1] Quantities in µl for one construct.

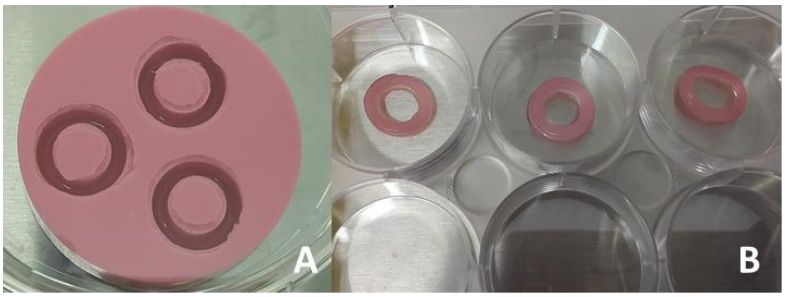

Figure 2: ECTM cast within the custom silicone mold (A) polymerized ECTM after removal from the mold (B).

Constructs were cultured for 5 days in static condition (Zimmermann, et al., 2000; Radisic, et al., 2004) followed by cyclic mechanical stimulation (10% strain at 1 Hz) for 4 days. Control engineered ring-tissues were cultured statically for 9 days. The culture medium consisted in low glucose (1g/L) DMEM (Gibco), supplemented with 10% FBS, 1% L-glutamine, 1% Hepes, 1% Penicillin/Streptomycin and was changed twice a week. At day 3, tranexamic acid *(t*AMCA, Sigma) at a concentration of 160 g/mL, was added in each well in order to delay fibrin gel degradation (Cholewinski, et al., 2009).

Bioreactor assembly and ECT mechanical stimulation

After 5 days of pre-culture, samples were transferred into the bioreactor and underwent to cyclic mechanical stimulation for additional 4 days. At day 5, the culture unit were assembled and the samples placed within the culture well.

To prepare the bioreactor under sterile condition, some pieces of the culture unit were preassembled and packed for sterilization, to reduce

the contamination risk during the assembling procedure. Indeed, for each side, the shaft was coupled with the construct holder and inserted within the lateral wall while the bellow was wrapped at both sides. The chamber, the pre-assembled later walls, the lid, the lid caps, the luer lock connectors, the compliance tube, and inlet tubing were independently packed and sterilized in autoclave.

The culture unit was assembled and the constructs transferred within the culture chamber under a laminar flow tissue culture hood. The series of images of Figure 3 shows the steps in sequence:

i. The left and right sub-assemblies composed by the lateral walls, the shafts, and the bellows were inserted in the culture chamber. This very first step allows to put in place the construct holders and to laterally seal the chamber (Figure 3A). The steady, nominal distance between the construct holders was 11.5 mm. Preliminary assessments suggested that this was the appropriate distance to ease the placement of the engineered constructs, aligning them according to the stretching direction avoiding to preload them. Besides, this distance was appropriate to assess the displacement once the culture chamber was connected to the mechanical actuator. The position of the shaft was maintained fixed by the two lateral position screws.

ii. The lid was leaned on top of the culture chamber, the inlet port connected to the inlet tube, closed at the opposite site with an injection site. The outlet port was connected to the compliance tube which was closed with a filter (2 μm) at the opposite site.

The four spots for the sensors were closed with the caps. Once completely assembled, a 200 mm petri dish was used to temporarily place the lid (Figure 3B).

iii. The chamber was filled with 50mL of culture medium (maintained at 37 °C) supplemented with *t*AMCA. Six ECTs were located between the two opposite pins (two constructs per couple of pins) as depicted in Figure 3C. Further 35mL of culture medium were added to reach a total of 85mL. The lid was screwed on top of the chamber. In this configuration the culture unit is a sterile closed system and can be moved out from the hood into the incubator (Figure 3D).

iv. The culture unit was connected to the mechanical framework directly inside the incubator (Figure 3E). The "actuation side" of the culture unit was attached to the actuator by means of the dedicate joint and the relative position-screw whose function was to hold fixed the holder. The initial distance of 15 mm between the coil and the magnetic housing was chosen as the most suitable for the voice coil and for having the best range of performance for the linear actuator.

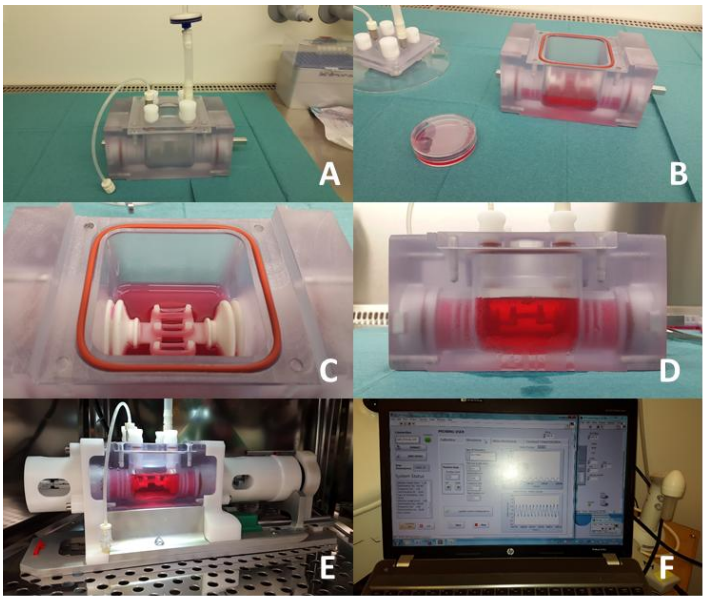

Figure 3: Assembling of the culture unit under sterile condition (A), prefilling with the culture medium (B), construct location between the holders pillar (C), completion of the filling up of the culture chamber with medium and placement of the lid (D), connection of the culture unit to the mechanical framework inside the incubator (E) and setting of the stimulation parameters via the dedicated software (F).

Initial settings and stimulation parameters were settled via the purpose-built software (Figure 3F): a pretension of 1 mm was imposed as minimum preload. At the beginning a sinusoidal strain with a frequency of 1Hz and amplitude of 8% of the initial length (12.5mm) was applied. Subsequently, the pretension was manually adjusted day by day to guarantee a constant 10% strain amplitude. Twenty five percent of the total amount of the culture medium present in the bioreactor was changed on day 3.

3.2.2 ECT characterization

3.2.2.1 Histological Evaluation

The cell distribution and morphological data on tissue development and organization were assessed by means of hematoxylin and eosin (H&E) staining on samples slices. The most relevant cardiac markers such as sarcomeric α-actinin, Troponin I and Connexin 43 were identified by immunofluorescent analysis. The presence of cardiac fibroblasts and the cell proliferation were assessed by using anti-Vimentin and anti-ki67 antibodies, respectively.

For histology, one half of each cultured ring was fixed for 1 h in 1.5% paraformaldehyde followed by a treatment with 30% sucrose solution overnight. The so fixed scaffold was then further divided in two halves then embedded in OCT (CellPath, UK), orienting each part through either the central transverse or the longitudinal cross section and 10-14 μm thick sections were cut by means of a micro-cryostat (Microm International GmbH, Germany).

Sections were stained with hematoxylin and eosin (H&E) according to standard protocols. Colour images were acquired with the Olympus BX63 microscope (Olympus, Switzerland). For fluorescence images, sections were tri-labeled for DAPI (to identify nuclei), cardiac troponin I (cTnI), and Connexin 43 or also quad-labeled for DAPI, sarcomeric α actinin (α-actinin), Vimentin and ki67.

Construct sections were incubated for 1 h in 0.3% Triton X-100 and 2% normal goat serum in PBS, and then for 1 h in the following primary antibodies: (a) mouse monoclonal anti-Cardiac Troponin I (Abcam) and (b) rabbit polyclonal anti-Connexin 43 (Millipore ab1728) at 1:100 or (c) mouse monoclonal anti-sarcomeric α actin (Abcam), (d) rabbit polyclonal anti-Ki67 (Abcam), and (d) goat polyclonal anti-Vimentin (Abcam) at 1:100. Subsequently, tissue sections were incubated in the dark for 1 h in fluorescently labelled Alexa488, and Alexa647 anti-mouse and anti-rabbit (Invitrogen) or Alexa488, Alexa 546 and Alexa647 anti-mouse and anti-rabbit and anti-goat (Invitrogen) secondary antibody at 1:200. Nuclei were stained using DAPI (Invitrogen) at 1:150 for 1 h. Antibodies were diluted in 0.3%Triton X-100 and 2% normal goat serum in PBS. Fluorescent images were taken with an Olympus BX63 microscope (Olympus, Switzerland) while confocal images were taken with a Zeiss LSM 510 microscope.

3.2.2.2 DNA quantification

The quantification of DNA was used to (i) assess the cell amount and to (2) normalize values of the collagen content; was quantified by the CyQUANT®Cell Proliferation Assay (Invitrogen). Each sample was weighed and digested overnight at 57 °C in 500µL of proteinase K solution (1 mg/mL proteinase K, 50mM TRIS, 1mM EDTA, 1mM iodoacetamide, and 10mg/mL pepstatin-A; Sigma–Aldrich) in double distilled water or potassium phosphate buffer (Sadr, et al., 2012). Working solutions were prepared according to the manufacturer's protocols. The analyses were carried out measuring fluorescence with a

SpectraMax Gemini XS Microplate Spectrofuorometer (Molecular Devices, USA). The excitation and emission wavelengths used were 485 and 583 nm, respectively. Each sample was measured in triplicate.

3.2.2.3 Collagen quantification - Hydroxyproline assay

Quantification of the collagen content within the ECT, was carried out with the hydroxyproline assay. After digestion in proteinase K (the same used for the DNA quantification), samples were mixed with equal parts with 12M HCl, hydrolyzed at 120 ° C for 24h and then dried (Cigan, et al., 2013). Samples were mixed with 50 μL buffered chloramine T reagent (63.5 mg of chloramine T dissolved in 1 mL water, and then diluted with 1.5mL n-propanol and 2.5 mL acetate-citrate buffer (pH 6); made fresh daily) and incubated for 20 min at room temperature. Then, further 50 μL dimethylaminobenzaldehyde (DMAB) solution mixed with perchloric acid were added (0.45 DMAB in 2 mL n-propanol and 1 mL perchloric acid 20%). The ratio of hydroxyproline to collagen mass was assumed as 1:10. The mixture was heated for 20 min at 60 ° C, cooled, and the absorbance determined at 550nm. The hydroxyproline concentration was determined from a standard curve (stock solution of hydroxyproline: 1mg/mL) (Hofman, et al., 2011)

3.2.2.4 Electrical functionality

The ECT contractile function was assessed by evaluating the response to the external pacing. The Excitation Threshold (ET) and Maximum Capture Rate (MCR), defined respectively as the voltage at which constructs are observed to beat synchronously and the maximum pacing frequency for synchronous contraction (evaluated using voltage of 2

times the ET), were determined (Radisic, et al., 2004). Furthermore, video analysis of constructs under stimulation was performed to determine the regularity and frequency of contractions.

At day 5 and 9, the contractile function of the samples was evaluated by monitoring spontaneous beating and contractile activity upon electrical stimulation at 2X/4X magnification using a bright field microscope (Olympus), keeping the temperature constant at 37 ° C. Each construct was placed in a Petri dish filled with 5 mL of medium and containing two carbon rod electrodes (Figure 4A, B), which were connected to a custom built electrical stimulation system (Figure 4B, C) (stimulation frequency range=0-10 Hz, stimulation amplitude= 2-6 V/cm and pulse duration=0-10 ms).

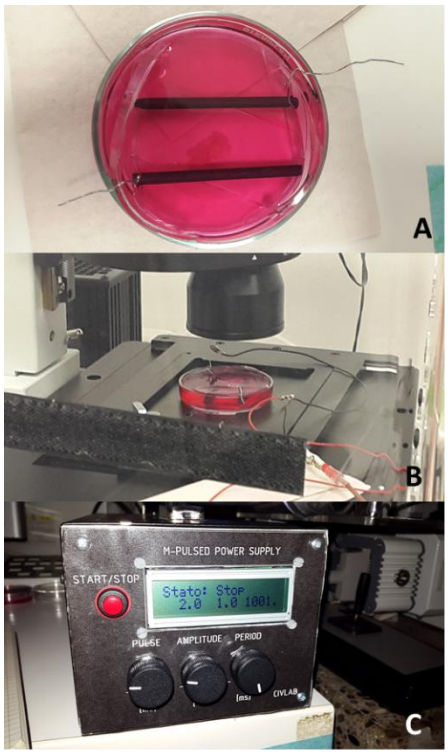

Figure 4: Stimulation chamber (A), 37 ° C controlled atmosphere Olympus microscope (B), custom built electrical stimulator (C)

Stimuli (rectangular pulses, 2ms duration) were applied at a rate of 1Hz starting at the 1.0 V amplitude. Different spots of the constructs (n= 3, 4) were analysed: the voltage amplitude was increased in 0.5 V increments till to reach the ET. The MCR, was determined using the voltage set at 2 times the ET by increasing the stimulation frequency in 0.1 Hz increments, until the paced contractions became irregular or desisted at all. Each stimulation sequence was digitally recorded (fps=20 up to 40). Video images recorded during the pacing were analysed in

ImageJ 1.47 software (Research Service Branch, NIH). Video frames (Figure 5A) were scaled according to the magnification, a threshold to quantitatively operate on the images, and a selection to highlight the construct and its surrounding space of movement during the contraction was defined (Figure 5, B).

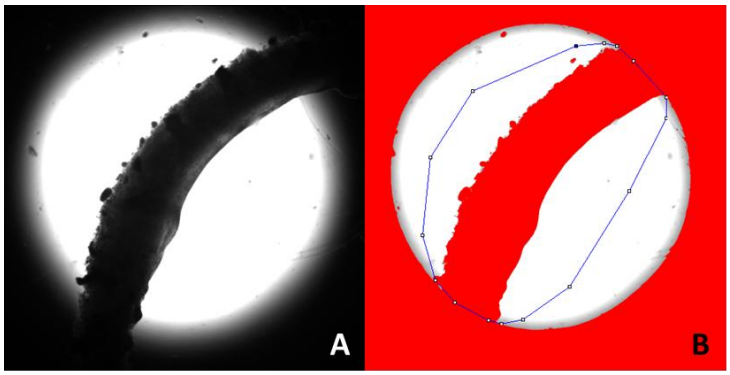

Figure 5: Assessment of the contractility under pacing in ImageJ 1.47 software. Frame of the video during pacing (A) and, delimitation of the region of interest (B).

The centre of mass coordinates were used to calculate the displacement of the selected area throughout the frames, which was then normalized to the position of the first frame, as follows: ($d_i = \sqrt{(x_2 - x_1)^2 - (y_2 - y_1)^2}$). Subsequently, the so obtained signal was used to (1) qualitatively show whether the ring follows the pacing and (2) eventually calculate the power spectral density (PSD) of the signal to assess the dominant frequency.

3.2.2.5 Mechanical properties: uniaxial tests

ECTs have been tested for elastic properties by determining the Young Modulus (E); initial length L_0 and cross sections (A_1, A_2) were measured with a digital caliper. The rings were hooked in a Microbionix (MTS System) using a 2N load cell and tensioned till an initial load of 0,02N was reached. A series of 10 cycles each of 0-10% strain at 0.1 Hz were performed, then the rings were stretched to failure at a rate of 5 mm/min. The engineering stress and strain were calculated as force divided the initial cross-sectional area (sum of the two areas on the opposite branches A_1, A_2) and the ratio of the change in length ($L - L_0$) and the original length (L_0). The Young Modulus (E) was calculated by linear regression of the stress-strain curve in the range of 0-30% elongation.

3.3 Results

3.3.1 Feasibility of the bioreactor-based culture of ECTs

The bioreactor suitability for culturing and delivering mechanical cyclical stimulation to 3D mm-scale cardiac-like tissues was verified. The assembling procedure, including the placement of the ECTs resulted to be easy and not time consuming. Indeed, time and changing of temperature could actually be an issue in handling cardiac tissue surrogates (Schaaf, et al., 2014). The culture system resulted to be free of bacteria/virus contamination during the entire dynamic stimulation period for all the conducted experiments. Changes in temperature (from environmental 24-27 $^\circ$C to 37 $^\circ$C in the incubator) and humidity (from

environmental 50-60% to 98/99% in the incubator) seemed to not affect the long term performances of the voice coil actuator or the displacement sensor which. A not significant difference in peak to peak amplitude was observed only at the beginning of the stimulation while the temperature of the system reached the incubator environment temperature (37 ° C). Therefore, a slight adaptation of the control parameters, in terms of K-PID (the additional gain implemented to modulate the Proportional-Integrative-Derivative compensator contribution), was needed to restore the nominal peak to peak amplitude. Even if some condensation drops formed on the surface of coil after 6 hours of mechanical actuation, the motor performance was not impaired.

3.3.2 ETCs remodeling along culture

The initial size of the engineered tissues was reproducible, but varied during the culture time. In static condition, we observed a significant shrinkage, whereas in the dynamic culture the cell-based construct maintained a similar size, but the fibrin gel appeared strongly remodelled (Figure 6). The ring cross section changed in shape and dimension: from an initial square-shape (˜9 mm^2) to a circular-shape (˜0.79-1 mm^2 for dynamic or ˜3.5-4 mm^2 for static condition).

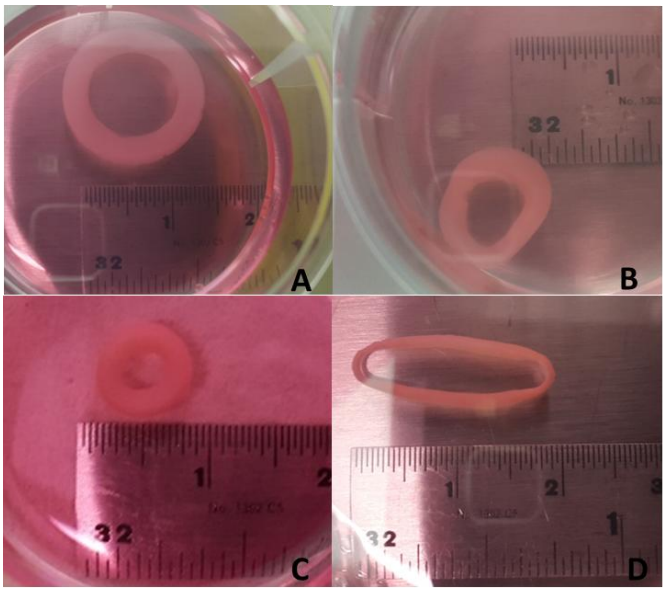

Figure 6: ECT initial size (a) and after 5 (b) or 9 (c) days in static condition (c) and after 9 days of culture in dynamic condition (d).

In previous experiments, dedicated to the optimization of culture parameters, we found out that no *t*AMCA supplementation in the culture medium resulted in the quick degradation of the constructs (data not shown).

Representative images of the samples stained for H&E at day 1 showed that cells were similarly present in the border and the center of the generated constructs, suggesting a uniform spatial cell distribution within the entire scaffold (Figure 7A). Regarding the cell morphology, cardiomyocytes encapsulated in the fibrin gel initially appeared round-shaped. After 5 days of static culture, constructs slightly shrank in size, but this didn' t result in any significant difference in cell

distribution along the border or in the centre of the construct compared to 1 day after encapsulation (Figure 7A).

DNA quantification, normalized to the sample weight, confirmed the qualitative observation, showing no significant difference in the amount of cells between day 5 and day 1 (Figure 8).

As opposed to static controls, at day 9, after four days of dynamic stimulation, samples showed a significant remodeling of the tissue along the border where the majority of the cells showed an elongated morphology, aligned with the construct edge (Figure 7B). Stimulated engineered tissues showed a superior extracellular matrix deposition and cell density at the border zone (within the first 50-200 μm-from the edges). For the majority of the samples, this improved organization was observed only on one side of the longitudinal cross section. For static controls, cells were mainly still round shaped and scarce matrix was deposited. No significant histological difference was noticed between the border and the centre of the static constructs.

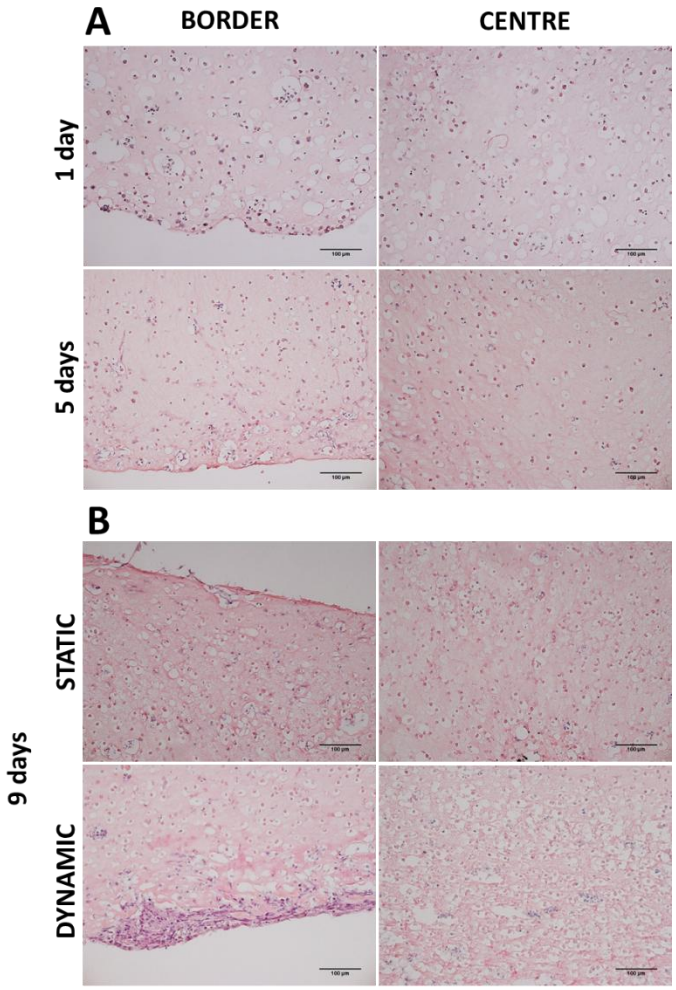

Figure 7: H&E stained sections of samples cultured for 1 or 5 days in unstimulated condition (A) and further culture up to 9 days in static or dynamic culture (B). Representative images of the border (left) and the center (right) of the constructs (longitudinal cross sections used) are shown (scale bar 100µm).

At day 9, in both static and dynamic conditions, the DNA amount drastically dropped almost 5 folds compared to day 5 (Figure 8). The cellular loss along the culture could be ascribed to the shrinkage and remodeling. However, as further analysis on the quantification of the DNA amount within the culture medium are needed to clarify this aspect.

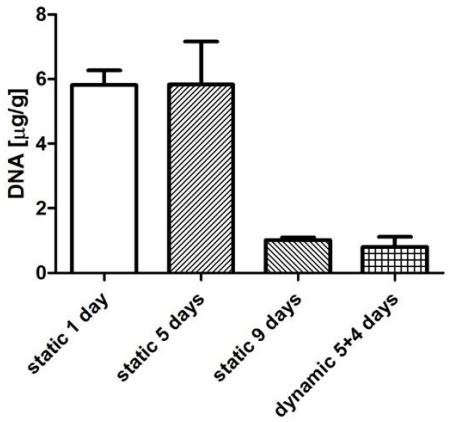

Figure 8: DNA content normalized to the dry weight at days 1, 5 and 9 for dynamically stimulated constructs and static controls

3.3.3 Cardiac maturation

Cardiomyocyte maturation and syncytia formation were assessed by late mature cardiac markers, as cardiac troponin I (cTnI), which is a contractile protein present in the mature sarcomeres, and Connexin 43 (Cx43), which is the most predominant electrical gap junctional protein.

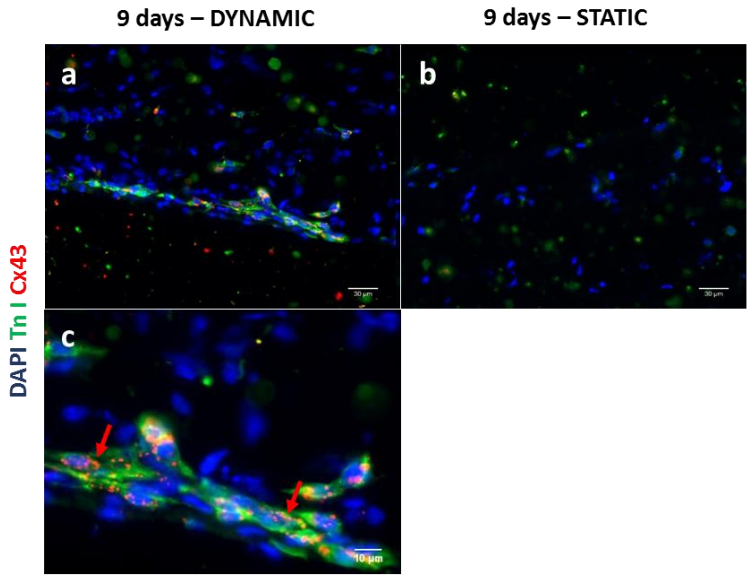

Figure 9: ECT cardiac maturation. Immunohistology staining for cell nuclei (DAPI, blue), Cx43 (red) and cTnI (green) of either mechanically stimulated constructs at low (a)or high (c) magnification and of static control (b). Scale bar 30μm. In the high magnification (c) of the dynamic condition the red arrows indicate the Cx43. Scale bar 10 μm

In stimulated ECTs, most of the cardiomyocytes close to the edges (up to 30-100 μm from the border) showed an elongated morphology with a cardiac troponin I structure and organization which is typical of mature sarcomeres and were longitudinally oriented, aligned towards the direction of the applied strain (Figure 9a, c).

In addition, cardiomyocytes appeared to be electrically coupled by the expression of functional gap junctions (Cx43), predominantly in-betweens neighbouring cells. In static condition, instead, cardiomyocytes showed preferentially a round shaped morphology and no mature

structures were found. Cells appeared to be mostly isolated, not connected and immature cells both at the edge and in the center of the static controls (Figure 9b).

The presence of cardiac fibroblasts and cell proliferation was assessed by distinguishing cardiomyocytes, expressing sarcomeric α actinin (α-actinin), a protein associated with z-discs that defines cardiac muscle sarcomeres, fibroblasts (vimentin-positive cells) and proliferating cells (positive for Ki67).

In dynamic condition, ECTs were characterized again by a well-organized network of elongated and longitudinally oriented cardiomyocytes, which showed α actinin positive striations characteristic of mature cells.

Cardiac fibroblasts positive for DAPI and Vimentin and negative for α-actinin were found in both dynamic (Figure 10a) and static condition (Figure 10b). In the dynamic condition fibroblasts were present in superior number and were mainly present at the edges, surrounding the organized cardiomyocytes.

Furthermore, in the dynamic condition more proliferating fibroblasts were found compared to static controls. The further investigation on the possible differentiation of fibroblasts into myofibroblasts is still ongoing.

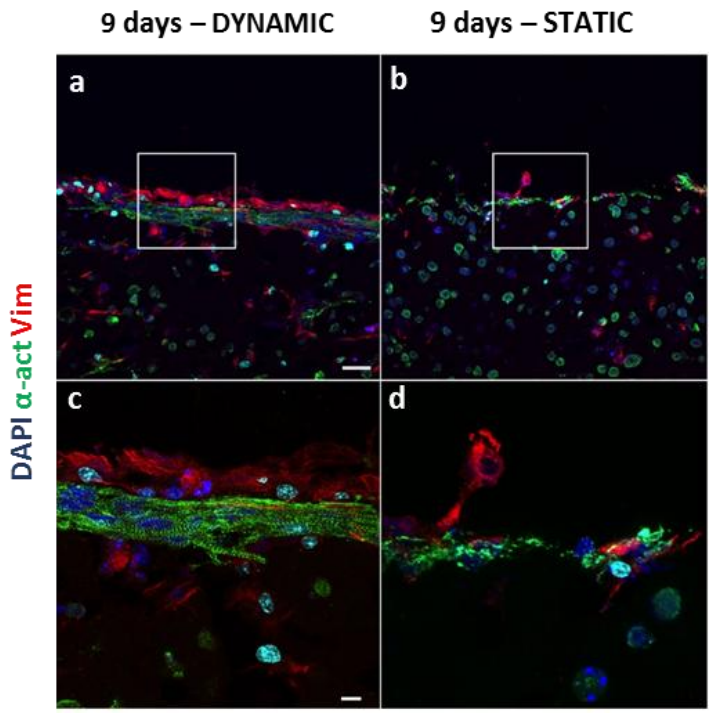

Figure 10: Confocal images of ECTs stained for cell nuclei (DAPI, blue), α-actinin (green), Vimentin (red) and ki67 (cyan)of (a) mechanically stimulated constructs and (b) static control at 40x magnification (scale bar 30µm). The areas within the white squares in (a) and (b) are enlarged respectively for dynamic in (c) and for static conditions (d) at 100x magnification (scale bar 5µm).

3.3.4 Electrical functionality

At day 5, ECTs did not spontaneously beat. If electrically stimulated, they responded to stimulation showing an Excitation Threshold (ET) of 7.2±3.3 V/cm and a maximum capture rate (MCR) of 5.0±2.1 Hz (Figure 11). The signals processed from the video analysis during stimulation at 1Hz showed an asynchronous and irregular contractile activity. The

peaks height was not uniform within the observed temporal window (Figure 12A, left panel). When the frequency was increased, the majority of the samples followed the pacing input with their own frequency. The power spectral density (PSD) of the signal assessed that the frequency is highly spread within the spectrum, indicating the partial inability of the constructs in following the pacing (Figure 12B, left panel). These data collectively suggest that, even if the constructs responded to the stimulation, the tissue maturation in terms of functional coupling of the cells was not yet achieved.

At day 9, no spontaneous beating was observed neither in dynamically stimulated nor in static controls. Noteworthy, no statically cultured ECT resulted to be functionally mature. On the contrary, all the dynamically stimulated constructs responded to external pacing. ET and MCR resulted to be 3.6±0.8 V/cm and 5.2±1.46 Hz, respectively (Figure 11). The signals processed from the video analysis of the contractility during stimulation at 1Hz showed a synchronous and regular contractile activity of the 3D constructs. The peaks height was uniform within the observed temporal window (Figure 12A, right panel). The power spectral density (PSD) of the signal assessed that the dominant frequency is localized at 1 Hz, i.e. the pacing frequency, indicating the ability of the constructs in following the pacing (Figure 12B, right panel,). When the frequency was increased, the samples were following the pacing input according to the correspondent frequency. In this case, the dynamic stimulation was instrumental for the further development of the excitation-contraction coupling machinery and so for tissue maturation. Indeed, as confirmed by the histologic images, even if

the network of cTnI-positive (or actinin-positive) cells was limited in thickness and confined to the lateral edge of the construct, it was continuous along the longitudinal cross section. Furthermore, the application of the cyclic mechanical stimulation increased also the Cx43 expression which implies the presence of electrical gap junctions.

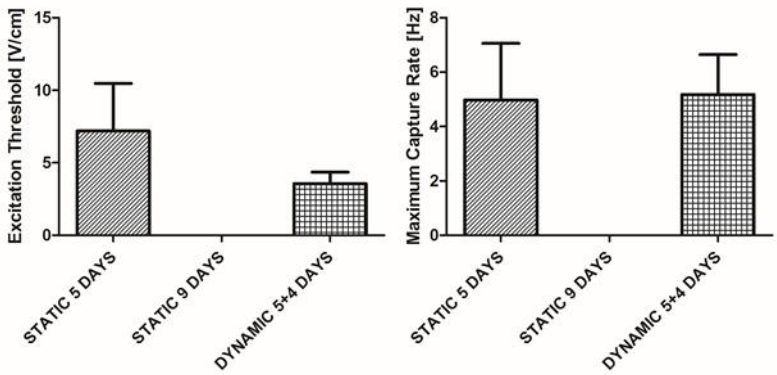

Figure 11: Graphs displaying the excitation threshold and maximum capture rate at 5 and 9 days of static and dynamic conditions and after 5 or 9 days of culture.

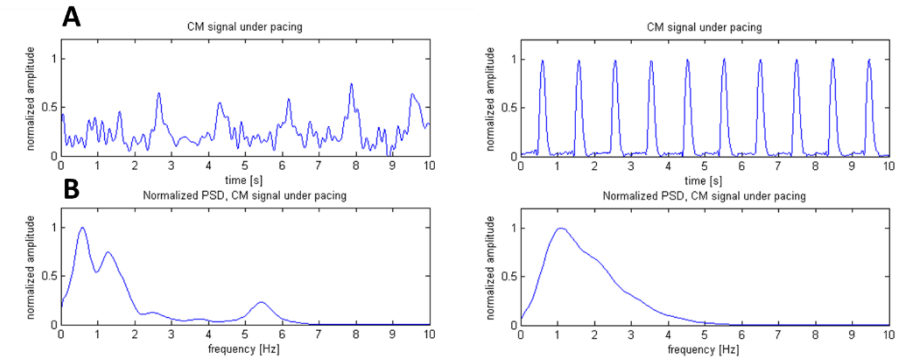

Figure 12: Analysis of the contractility (A) and the dominant frequency (B) of ECTs under pacing after 5 days in static condition (left)or 5+4 days in dynamic culture (right)

3.3.5 Mechanical uniaxial test and collagen quantification

The Young Modulus (E) was calculated by linear regression of the stress-strain curve in the range of 0-30% elongation. The ring shaped ECTs were hooked in the Microbionix (MTS System) using a 2N load cell (Figure 13, left panel). The modulus calculated in this range was found to be coherent with the elastic modulus calculated within the entire stress-strain curve range, till rupture (data not shown). This finding suggests that it is possible to assess the progress of the construct stiffness along the culture in a non-destructive manner within the established range of strain.

Constructs were pre-tensioned with an initial load of 20mN and, after a series of 10 cycles of 0-10% strain at 0.1 Hz, were stretched until failure. Elastic modulus was found to only slightly increase (6.7%) in the first five days of culture: 29.6±8.9 KPa and 31.7±3.1 KPa at day 1 and 5, respectively (Figure 13, right panel). At day 9, E for static condition was found to be 87.5±9.2 KPa and increased by 194.9% compared to the beginning of the culture. After additional 4 days of culture in dynamic condition, E increased up to 117.3 ± 13.0 KPa (Figure 13, right panel). Therefore, dynamically stimulated samples further improved the mechanical properties, by 295.5% and 34.1%, compared to constructs statically cultured for 1 or 9 days, respectively.

With respect to the beginning of the stimulation (at day 5), E of samples that underwent to cyclic stretch increased by 270.5% while the static controls had an increase of only 176.3% in further 4 days of culture.

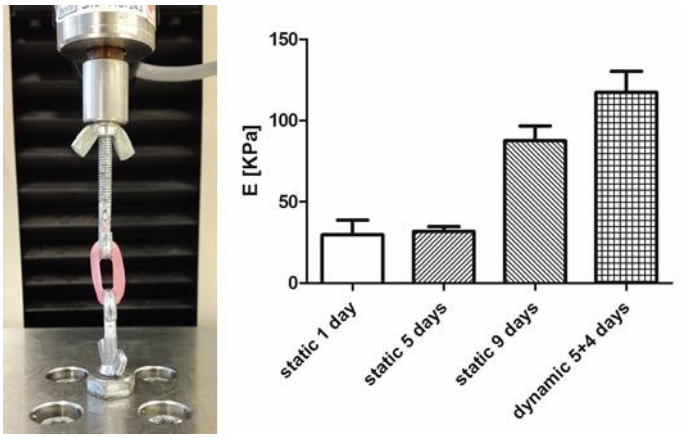

Figure 13: Set-up of the mechanical test (left panel).Young Modulus (E) of the constructs found in static or dynamic conditions (right panel)

The total content of collagen per sample was quantified via hydroxyproline assay and the total and was normalized by the respective amount of DNA.

The collagen content was 0.38 ± 0.07 and 0.52 ± 0.33 at day 1 and 5, respectively (Figure 14, left panel). After 5 days of static culture, the collagen amount increased by 37.7%. At day 9, the collagen content arose to 1.76 ± 0.52 for static condition and was 2.85 ± 0.51 in the dynamic stimulated constructs (Figure 14, left panel). For constructs after 9 days of static culture, the collagen content increased by 366.8% compared with constructs at the first day of culture. The presence of collagen in the dynamic stimulated samples was further enhanced with an increase of 653.9% compared with constructs at the first day of culture. With respect to day 5, i.e. at the beginning of the stimulation, the collagen content of samples that underwent to cyclic stretch increased by 445.7%

while the static controls had an increase of 239.2% in further 4 days of culture.

Both the Young modulus and the collagen content increased over the time in culture. Figure 14 (right panel) shows a plot of the collagen content versus E regardless to the culture condition. The linear regression calculated on the data (R^2=0.90) showed a significant correlation indicating that the enhancement of the mechanical properties could be ascribed to the collagen deposited in the ECM along the culture. This is reasonable, as collagen is the primary load-bearing protein which provides passive stiffness during diastole in the native heart matrix. (Fomovsky, Thomopoulos and Holmes 2010).

Interestingly, in the dynamic condition the 61.5% more of collagen content was found in comparison with the static control. The increment of collagen is most likely due to the superior presence of fibroblasts in the dynamic condition compared to the static controls and that, somehow, the cyclic stretch likely enhanced the proliferation of fibroblasts and consequently the amount of the produced ECM.

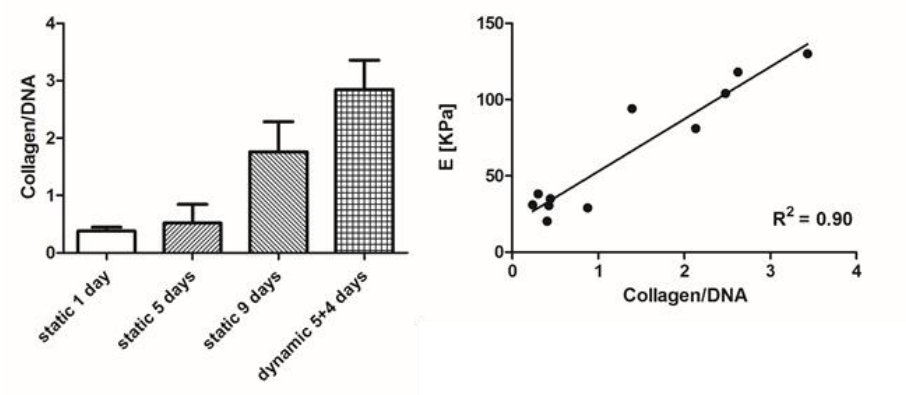

Figure 14: Collagen content normalized to DNA (left panel) and linear regression of the collagen content versus Young modulus (right panel).

3.4 Discussions and Conclusions

Individually, both mechanical and electrical stimulation have been established as standard conditioning methods for engineered cardiac constructs and have been studied extensively. These stimuli were shown to significantly increase the functional and the overall maturation of the cardiac-like tissues. While electrical stimulation is related to the establishment of functional gap junction, mechanical stimulation was shown to particularly improve the 3D tissue organization, cell alignment, cardiac maturation and the functionality in terms of generated active force. Mechanical stimulation alone appears quite a potent regulator in the development and cardiac morphogenesis, indeed much of the reorganization that occurs in utero is in the presence of changing mechanical stimuli (Stoppel, Kaplan and Black 2016).

There are different types of mechanical stimulation that can be applied, static or cyclic loading (corresponding to isometric and isotonic contraction) or auxotonic loading (a combination of isometric and isotonic loading). Even if auxotonic loading seems to resemble the physiologic contraction cycle quite closely, cyclic strain could be applied also in early maturation stage of the cardiac constructs. Indeed, under a proper frequency, the engineered constructs could adapts the contraction cycle to the stretch cycle (W. Zimmermann, 2013). Auxotonic contraction indeed are possible only when the myofibers are quite mature and the contractile unit is well formed and is able to contracts.

Several bioreactors have been developed to provide controlled mechanical stimulation during culture (Akhyari, et al. 2002 , Birla, Huang and Dennis 2007, Morgan and Black III 2014, Salazar, et al. 2015) to generate reliable functional cardiac in vitro models to investigate fundamental biological questions. However, most of the past bioreactors focused on the mere application of the cyclic strain. Based on our knowledge, there is not yet a device capable to apply physiological strain to 3D mm-thick samples: (1) mimicking the wide range of conditions experienced by the heart tissue in vivo, (2) monitoring the maturation progresses and (3) adapting the stimulation pattern to the actual maturation stage of the constructs.

In this PhD project, the aim was to develop a new bioreactor-based platform which, in its most advanced operational mode, is capable to deliver native-like/pathologic stimuli, measuring in real-time the tissue response (and the milieu parameters) and eventually adapting the stimulation to the maturation phase of the constructs. As a proof of

concept and towards the final validation of the platform potential, in this first experimental series, the bioreactor has been used in its basic configuration, to verify its feasibility in delivering mechanical cyclical stimulation to 3D fibrin-based, ring shaped Engineered Cardiac Tissue (ECTs) under dynamic culture.

Firstly, the platform has been verified for the engineering design and the suitability in culturing *ad-hoc* designed constructs. Indeed, the bioreactor showed: (i) ease and quickness of assembling the device components as well as loading the constructs, (ii) maintenance of the culture sterility during dynamic motion (iii) capability in setting the culture parameters (cyclic displacement and frequency) by means of the software user interface, (iv) preservation of the mechanical functionality and long-term performances.

Secondly, the effects of mechanical conditioning on ECTs have been evaluated. To that end, neonatal rat cardiomyocytes were embedded in a fibrin gel and the generated constructs were pre-cultured for 5 days in static condition and transferred into the bioreactor to be cyclically stretched for 4 days (10% strain at 1 Hz). In parallel, control engineered ring-tissues were cultured statically for 9 days.

To fulfil this purpose, the fibrin gel composition and fibrin to thrombin ratio where chosen to integrate some requirements: (1) ease of casting, (2) manageability, and (3) adequate hardiness for mechanical loading as well as the control of degradation. Several combinations and proportions of the components of the fibrin gel mixture (i.e. mainly calcium, fibrinogen, thrombin and cells), for heart tissue models, are

proposed in literature mostly to adjust the time of polymerization and degradation reactions, also controlled by using protease inhibitors, such as aprotinin and tranexamic acid (Cholewinski, et al. 2009, Birla, Huang and Dennis 2007, Morgan and Black III 2014). Besides, the ECTs mix composition, must be adapted and optimized for the specific shape/topology, casting method and the experiment settings of each culture platform. (Yuan, Sullivan and Black 2011).

According to this, the fibrin gel mixture and the casting technique chosen in this work allowed for a fast polymerisation and gel compaction as well as repeatability in the ECTs topology. The use of *t*AMCA, supplemented in the culture medium, allowed to control the degradation within the 5 days of pre-culture before the mechanical stimulation started. Furthermore, histologic H&E representative images of the samples at day 1, showed a homogenous cell distribution within the entire scaffold confirming the suitability of the casting protocol.

The use of the bioreactor platform showed to be instrumental for delivering sinusoidal cyclic strain, resulting in ECT maturation and in the formation of electrical gap junctional protein between neighboring cardiomyocytes. Fluorescent and confocal images of the stimulated construct showed a network of cTnI positive or sarcomeric α-actinin, longitudinally oriented, elongated and mature cardiomyocytes prevalently localized on the lateral edge of the construct, ranging within a thickness of 30μm up to 100 μm and continuous along the longitudinal cross section. Stimulation increased also the Cx43 expression mostly on lateral parts of the cell membrane. Conversely, such structures were

sporadically found in the static controls. Prevalently isolated, not connected and immature cells were found at edge as well as in the centre of the constructs. These findings were consistent with previous studies on neonatal rat or chick cardiomyocytes embedded in Matrigel and collagen I, subjected to mechanical stimulation (10% strain, 2Hz) (Zimmermann, Schneiderbanger, et al. 2002). These structural properties were associated to an increased contraction force as well as a positive force-length and negative force frequency relationship (Zimmermann, Fink, et al. 2000, Fink, et al. 2000).

Although nuclei appeared to be homogenously distributed through the sample thickness, this kind of structure was systematically found at the edges and specifically only on one side of the longitudinal cross section. Limitation of the oxygen (and nutrients) diffusion, within the three-dimensional constructs, has been already observed in previous studies: increasing the distance from the construct edge correlated with a decline in cardiomyocyte density and viability towards the centre. (Seiffert, et al. 2013). In the 5 days of pre-culture, constructs were statically housed within six-well plate and supplemented with 5mL of culture medium. In this set-up, nutrient transport is diffusion-limited and one side of the ring is in direct contact with the culture plate and less exposed to the medium. Indeed, images of the central transverse section, showed higher cellularity and the presence of the network almost all around the section with the exception of a small portion. This pre-culture condition could justify why, after stimulation, in the longitudinal cross sections, for the majority of the samples, this more optimal organization was observed only on one side of the longitudinal cross

section. This part most likely corresponded to the portion of the ring that was in contact with either the well plate in static condition or the other replicates during cyclic strain and, therefore, resulted less exposed to the culture medium. Furthermore, even if the applied stretch could promote nutrient and waste exchange by cyclically opening the scaffold structure, based on our results, the diffusion of nutrients and oxygen appeared not to be efficient in the very centre of the ring.

The improved functional structure, promoted by the mechanical stimulation, was confirmed by the contractility assessment. Before stimulation, after 5 days of static pre-culture, ECTs responded to the pacing (ET=7.2±3.3 V/cm and MCR=5.0±2.1 Hz) irregularly and following the increasing pacing input with their own frequency. After cyclic stimulation they were beating synchronously at the pacing frequency with an excitation threshold mean value about the half (3.6±0.8 V/cm V/cm) and following the increase of pacing within a maximum capture rate range slightly higher (5.0±2.1 Hz). These electrical excitability parameters are usually used for evaluation of the electrical functionality in protocols where the sole electrical stimulation is applied, which is known to enhance the intercellular electrical communication (Radisic, Park and Shing, et al. 2004). In protocols where only the mechanical stimulation is administered, the functional performances, for spontaneous beating and in the presence of pacing, is assessed by measuring the force of contraction (twitch tension) (Salazar, et al. 2015). However, also the application of the sole mechanical stimulation resulted in an analogous functional coupling of cardiac cells (Zimmermann, et al. 2006), indicating that phasic stretch is instrumental

for the further development of an adult-like cardiac phenotype responsive to electrical excitation.

The collagen content increased along the culture, and further increased in the presence of cyclic stretch; this is consistent with studies of cardiomyocytes cultured in 3D scaffolds composed by collagen I and Matrigel (Fink, et al. 2000 , Zimmermann, Schneiderbanger, et al. 2002) or fibrin (Salazar, et al. 2015). Also, the collagen content was found to be positively correlated with the Young modulus, which is reasonable since the role of collagen in sustaining the heart passive stiffness (Fomovsky, Thomopoulos and Holmes 2010). It is possible to speculate that the major amount of collagen found in the stimulated constructs was due to new ECM synthetized by fibroblasts (Salazar, et al. 2015). Indeed, a superior presence of fibroblasts was observed in the dynamic condition compared to the static controls. Some cells were double positive for vimentin and Ki67, which indicates that mechanical stimulation might support fibroblast proliferation. Further investigations are also needed in order to ascertain if any phenotype switch to myofibroblasts has occurred (Zimmermann, Schneiderbanger, et al. 2002).

One of the main limitations emerged during operations with the current bioreactor design is the low number of replicates that could be stretched in each experiment and the fact that each replicate is not independent from the others. A novel attachment mechanism could be devised for increasing the number of cultured samples guaranteeing homogeneous load. Different geometries of the ECTs should be also tested. The ratio fibrinogen to thrombin can also be tuned to evaluate

the effect on oxygen diffusion within the inner part of the 3D construct. Assays to assess viability should also be performed. The use of special well plates that allow for an exchange of nutrients during static pre-culture could optimize the tissue development since the early phase of pre-culture.

In conclusion, this study has shown the feasibility of the bioreactor-platform in delivering mechanical cyclical stimulation to 3D fibrin-based, ring shaped ECTs. The platform has been verified for the engineering design and the suitability in culturing the *ad-hoc* designed constructs. Jointly, compared with static controls, ECTs cultured under dynamic stimulation were functionally mature, capable to respond to external electrical pacing. ECTs also showed a significant matrix remodeling, followed by an increase of collagen deposition. The assessment of the mechanical properties at predefined step points of the culture revealed to be a fundamental tool to control cell phenotype and thus ECM synthesis.

In this very first experiments, the bioreactor platform has been used in its basic configuration, disabling the force, pH and O_2 sensing functions. Mechanical assessment of the fibrin based construct has been conducted with a standard test machine to separate the variability due to the device under investigation from the ECTs variability.

In the next steps, to reach the comprehensive validation of the platform, the constructs properties and the milieu parameters will be monitored and recorded by the sensors (force, pH, O_2), which have been already devised. The output from these experimental data will serve to

generate a dataset usable for creating a developmental predictive model in order to adequately (physiologically) train the cardiac construct to develop optimal contractile and structural properties.

In a further step, the bioreactor potential could be exploited by using human Endothelial stem cells (ESC) or induced Pluripotent Stem Cells (iPSC) to possibly generate cardiac patches capable to substitute the damaged myocardium after a myocardial infarction.

Acknowledgements

The author would like to thank PI Dr. Anna Marsano (Cardiac Surgery and Engineering group, Universitätsspital, Basel, Switzerland) for the opportunity to work in her group and for the kind support, Dr. Giulia Cerino and Dr. Emanuele Gaudiello (Cardiac Surgery and Engineering group, Universitätsspital, Basel, Switzerland) for the warm welcome and insightful suggestions.

References

Akhyari, P., et al. "Mechanical stretch regimen enhances the formation of bioengineered autologous cardiac muscle grafts." *Circulation* 106, no. 12 Suppl 1 (2002): I137-42.

Birla, R.K., Y.C. Huang, and R.G. Dennis. "Development of a novel bioreactor for the mechanical loading of tissue-engineered heart muscle." *Tissue Engineering* 13, no. 9 (2007): 2239-48.

Centola, M., et al. "Scaffold-based delivery of a clinically relevant anti-angiogenic drug promotes the formation of in vivo stable cartilage." *Tissue Eng Part A* 19, no. 17-18 (2013): 1960-71.

Cholewinski, E., M. Dietrich, T. C. Flanagan, T. Schmitz-Rode, and S. Jockenhoevel. "Tranexamic acid- an alternative to aprotinin in fibrin-based cardiovascular tissue engineering." *Tissue Engineering Part A*, 2009.

Cigan, A.D., et al. "Insulin, Ascorbate, and Glucose Have a Much Creater Influence than Transferrin and Selenuos Acid on the In Vitro Growth of Engineered Cartilage in Chondrogenic Media." (Tissue Engineering: part A) 19, no. 17-18 (2013): 1941-1948.

Fink, C., S. Ergün, D. Kralisch, U. Remmers, J. Weil, and T. Eschenhagen. "Chronic stretch of engineered heart tissue induces hypertrophy and functional improvement." *FASEB J* 14, no. 5 (2000): 669-79.

Fomovsky, G.M., S. Thomopoulos, and J.W. Holmes. "Contribution of extracellular matrix to the mechanical properties of the heart." *J Mol Cell Cardiol* 48, no. 3 (2010): 490-6.

Govoni, M., Muscari C., C. Guarnieri, and E. Giordano. "Mechanostimulation Protocols for Cardiac Tissue Engineering." 2013.

Hansen, A., et al. "Development of a drug screening platform based on engineered heart tissue." *Circ Res* 107, no. 1 (2010): 35-44.

Hirt, M.N., A. Hansen, and T. Eshenhagen. "Cardiac Tissue Engineering: State of the Art." *Circulation Research* 114, no. 2 (2014): 354-67.

Hofman, K., B. Hall, H. Cleaver, and S. Marshall. "High-throughput qauntificationof hydroxyproline for determination of collagen." *Analytical Biochemistry* 417 (2011): 289-291.

Jockenhoevel, S., et al. "Fibrin gel-advantages of a new scaffold in cardiovascular tissue engineering." *Eur J Cardiothorac Surg* 19, no. 4 (2001): 424-30.

Mol, A., et al. "Fibrin as a cell carrier in cardiovascular tissue engineering applications." *Biomaterials* 26, no. 16 (2005): 3113-21.

Morgan, K.Y., and L.D. Black III. *Creation of Bioreactor for the Apllication of Variable Amplitude Mechanical Stimulation of Fibrin Gel-Based Engineered Cardiac Tissue.* Vol. 1181, in *Cardiac Tissue Engineering: Methods and Protocols, Methods in Molecular Biology*. Milica Radisic and Lauren D. Black III, 2014.

Radisic, M., et al. "Functional assembly of engineered myocardium by electrical stimulation of cardiac myocytes cultured on scaffolds." *PNAS* 101 , no. 52 (2004): 18129–18134.

Sadr, N., et al. "Enhancing the biological performance of synthetic polymeric materials by decoration with engineered, decellularized extracellular matrix." *Biomaterials* 33, no. 20 (2012): 5085-93.

Salazar, B.H., A.T. Cashion, R.G. Dennis, and R.K. Birla. "Development of a Cyclic Strain Bioreactor for Mechanical Enhancement and Assessment of Bioengineered Myocardial Constructs." *Cardiovasc Eng Technol.* 6, no. 4 (2015): 533-45.

Schaaf, S., A. Eder, I. Vollert, A. Stohr, A. Hansen, and T. Eschenhagen. *Generation of Strip-Format Fibrin-BAsed Engineered Heart Tissue (EHT).* Vol. 1181, in *Cardiac Tissue Engineering: Methods and Protocols, Methods in Molecular Biology*. Milica Radisic and Lauren D. Black III, 2014.

Seiffert, M., et al. «Oxygen diffusion in fibrin-based engineered heart tissue and the effect of artificial oxygen carriers.¸ *Thorac cardiovasc Surg*, 2013.

Stoppel, W.L., D.L. Kaplan, and L.D.III Black. "Electrical and mechanical stimulation of cardiac cells and tissue constructs." *Adv Drug Deliv Rev*, 2016: 135-55.

Vunjak-Novakovic, G., et al. "Challenges in cardiac tissue engineering." *Tissue Eng Part B* 16, no. 2 (2010): 169-87.

Vunjak-Novakovic, G., T. Eschenhagen, and C. Mummery. "Myocardial Tissue Engineering: In Vitro Models." *Cold Spring Harb Perspect Med*, 2014.

Yuan, Y.K., K.E. Sullivan, and L.D. Black. "Encapsulation of cardiomyocytes in a fibrin hydrogel for cardiac tissue engineering." *Journal of Visualized Experiments* 19, no. 55 (2011).

Zimmermann, W., et al. «Engineered heart tissue grafts improve systolic and diastolic function in infarcted rat hearts.¸ *Nat Med* 12 (2006): 452–458.

Zimmermann, W.H. "Biomechanical regulation of in vitro cardiogenesis for tissue-engineered heart repair." *Stem Cell Research & Therapy* 4, no. 137 (2013).

Zimmermann, W.H., C. Fink, D. Kralisch, U. Remmers, J. Weil, and T. Eschenhagen. "Three-dimensional engineered heart tissue from neonatal rat cardiac myocytes." *Biotechnol Bioeng* 68 (2000): 106–114.

Zimmermann, W.H., et al. «Tissue engineering of a differentiated cardiac muscle construct.¸ *Circ Res* 90 (2002): 223–230 .

Chapter 4
Conclusions and Future Perspectives

4.1 Bioreactor platform

In this thesis the design and development of a bioreactor platform for culturing cardiac tissue has been presented. The here proposed system is designed (1) to deliver native-like or pathologic-like stimuli (namely cyclic strain) to 3D engineered cardiac constructs, (2) to assess their mechanical properties along the culture in a non-destructive manner and (3) to monitor in real time the culture environment. In the past years, several devices have been developed for the purpose of culturing cardiac tissue (Birla, Huang and Dennis 2007, Kensah, et al. 2011, Govoni, et al. 2014). However, the mechanical properties of the constructs have never been monitored in combination with physicochemical parameters (Kensah, et al. 2011). Moreover, the delivered mechanical stimulation have been mainly narrowed to pre-defined stimulation waveforms, thus limiting the application of biomimetic culture strategies (Birla, Huang

and Dennis 2007). For these main reasons, the bioreactor-based platforms developed for cardiac tissue engineering applications so far, are still ineffective in properly training the cardiac engineered muscle to develop optimal contractile and structural properties. (Zimmermann 2013).

The engineering solutions which have been introduced in the design of the bioreactor allowed the implementation of a displacement-controlled strategy within a wide range of physiological/pathological elongations and frequencies. In principle, the designed control architecture is also suitable for a force-based control, when a force transducer is used in the control loop in place of the position transducer.

In view of the advantages of using a linear actuator, which simplifies the actuation kinematics *per-se*, the application of the voice coil allowed the obtainment of an enhanced positioning accuracy and of markedly high accelerations. Indeed, one of the main drawback of using stepper motors is their limited bandwidth, which would prevent the exploration of high cycle rates in experiments, a problem that can be addressed only by accepting an impaired mechanical displacement resolution (Salazar, et al. 2015).

Thanks to the adopted control strategy, high fidelity tracking of the reference position is guaranteed also when modification of environmental variables (e.g. temperature, humidity, and pressure) can be the source of unexpected additional friction.

With regards to the sensing unit, the selected sensors for O_2 and pH monitoring are characterized by the proper sensitivity. Moreover, when embedded within the culture unit, the housing mechanism (bayonet fitting inserts) and the sterilization procedures have given evidence of sterility maintenance both in static and dynamic working conditions.

The sensing unit, i.e. the load cell, has demonstrated the capability to estimate the mechanical properties, i.e. stiffness, of a calibrated instrumentation spring within maximum 10% of the real value, thus confirming that the system can be applied for a real time evaluation of the mechanical properties of cultured constructs, even if further improvements are required to increase its reliability, when applied to monitor real constructs.

Finally, the software user-interface, which have been developed on-purpose, has demonstrated to fulfill the design requisites in terms of (i) driving the stimulation settings and (ii) displaying signals from the sensor.

4.2 Engineered Cardiac Tissues

As a proof of concept, and towards the final validation of the platform potential, a first experimental campaign has been carried out with a double aim: (1) to verify the bioreactor feasibility in delivering mechanical cyclical stimulation to 3D fibrin-based, ring shaped Engineered Cardiac Tissues (ECTs); (2) to assess the effect of cyclic

strain on tissue maturation, contractility and modification on its elastic properties.

To that end, neonatal rat cardiomyocytes embedded in ring-shaped fibrin gel, have been pre-cultured for 5 days in static condition and transferred into the bioreactor to be cyclically stretched for 4 days (10% strain at 1 Hz). In parallel, control engineered ring-tissues have been cultured statically for 9 days.

Concerning the first aim, the reliability of the bioreactor platform has been verified both for the engineering design and for the capability of culturing *ad-hoc* designed constructs.

With regard to the second aim, the sinusoidal cyclic strain prescribed to the construct has showed to be instrumental in ECTs maturation and in the formation of electrical gap junctional proteins among neighboring cardiomyocytes. Fluorescent and confocal microscopy images have confirmed that the imposed stimulation has promoted: (1) the Cx43 expression and (2) the formation of a network of cTnI/sarcomeric α-actinin positive, longitudinally oriented, elongated and mature cardiomyocytes along the longitudinal cross section (even if prevalently localized on lateral edge) of the construct. Conversely, in the static controls, prevalently isolated, not connected and immature cells have been observed at edge as well as in the centre of the constructs.

The mechanical stimulation was also instrumental to promote the development of an adult-like cardiac phenotype responsive to electrical

excitation. The mechanical stimulation has improved the functional coupling of the cells: while static controls have been observed to not beat neither spontaneously nor under pacing, stimulated constructs have responded regularly and synchronously to pacing.

Among the main findings, ECTs have been observed to undergo a significant matrix remodelling, followed by an increase of collagen deposition. Moreover it has been found that the cyclic stimulation enhanced the mechanical properties of the cultured ring constructs. In particular a marked increase of the Young modulus has been observed for dynamically stimulated specimen, compared to the first day of culture and the static controls. The construct increased Young modulus has been found to be correlated with the increase of collagen, which is the primary load-bearing protein in the native heart matrix.

4.3 Limitations

The current bioreactor configuration could be further optimized to improve even more the control over the mechanical stimulation and therefore over the final quality of the engineered cardiac models.

From a mechanical point of view, the solution adopted to couple the actuator and the engineered tissue (i.e., the load) might introduce unexpected friction that affects the displacement accuracy. Indeed, as far as the test conditions are significantly changing (e.g. humidity, increase of temperature, thermal dilatation of the components) the

friction mitigation sustained by the feed-forward loop (off-line characterized), becomes inadequate.

A few structural modifications, involving the increase of the gap between sliding elements, i.e. the lateral walls and the shafts, or the design of an alternative coupling method, could actually mitigate the friction effects.

Pertaining to the control strategy, the hardware used to implement the control strategy presents few limitations. During high speed displacements, processor frequency could be not high enough to close the actuation displacement loop. A future solution could be to separate the monitoring of the sensors (which have a slower dynamic) from the actuation control, by using two dedicated modules in order to guarantee a Hard Real Time (HRT) performance.

Furthermore, the coupling between the load cell and the shaft on the "sensing side", has revealed to be a possible design weakness. In the current set-up the load cell is placed outside of the culture chamber, and the force exerted by the construct has to be transmitted through the lateral wall. This architectural solution could be a source of inaccuracy. Future modifications could embed the housing of the force sensor within the culture chamber in order to increase the measurement reliability.

About the feasibility in culturing engineering cardiac models, the main limitation of the current bioreactor design is in the low number of replicates that could be stretched in each experiment and the fact that

each replicate is not independent from the others. A novel attachment mechanism could be devised for increasing the number of cultured samples guaranteeing homogeneous load.

Concerning the engineered cardiac tissues, other geometries besides the ring-shaped samples (e.g. strips, dog bone-shape) could be used in order to simplify the casting procedure and to perform the mechanical testing according to standard protocol. Moreover, the integration of well plates allowing for an exchange of nutrients during static pre-culture could improve the protocol and optimize the maturation of the tissue since the early phase of pre-culture.

4.4 Conclusive Considerations and Future works

The biological validation of the platform here proposed has been planned in a step-by-step manner. This first biological experimental series allowed to verify the capability of the bioreactor of delivering mechanical stimulation to 3D fibrin-based, ring shaped ECTs and showed that the application of cyclic strain (10%, 1Hz) improved tissue maturation, contractility and stiffness.

In these experiments, the bioreactor platform has been used in its basic configuration, disabling the force, pH and O_2 sensing functions. Mechanical assessment of the fibrin based construct has been conducted with a standard test machine (MTS, MTS System Corporation, USA) to separate the variability due to the device under investigation from the ECTs variability.

Two further steps are required in order to reach a comprehensive validation of the platform. In the next step, biological tests will be carried out applying cyclic strain while monitoring in real time the evolution of the mechanical properties by enabling the force measuring system of the bioreactor. Besides, the O_2 and pH milieu parameters, will be monitored and recorded. The output from these experimental data will serve as a basis for the generation of a dataset to be used as predictive model to mimic the developmental process.

Thanks to the adopted hardware and software architecture the further step will be the implementation of an adaptive culture strategy. Indeed, the use of an automated feedback loop could allow to measure, in real-time, the tissue mechanical response and, on its basis, to define the appropriate mechanical stimulation in order to adequately (physiologically) stimulate the cardiac construct to develop optimal contractile and structural properties.

Furthermore, the integration of an electrical stimulation system to facilitate syncytial arrangement of cardiomyocyte and further assist morphologic and functional maturation, can be easily integrated within the bioreactor platform to enrich its functionalities.

Finally, the implementation of an automated feeding perfusion circuit will allow the automatic exchange of the medium within the culture chamber, in response to significant variations of the metabolic quantities measured by the milieu sensors.

References

Birla, R.K., Y.C. Huang, and R.G. Dennis. "Development of a novel bioreactor for the mechanical loading of tissue-engineered heart muscle." *Tissue Engineering* 13, no. 9 (2007): 2239-48.

Govoni, M., et al. "An innovative stand-alone bioreactor for the highly reproducible transfer of cyclic mechanical stretch to stem cells cultured in a 3D scaffold." *J Tissue Eng Regen Med* 8, no. 10 (2014): 787-93.

Kensah, G., et al. "A novel miniaturized multimodal bioreactor for continuous in situ assessment of bioartificial cardiac tissue during stimulation and maturation." *Tissue Eng Part C* 17, no. 4 (2011): 463-73.

Salazar, B.H., A.T. Cashion, R.G. Dennis, and R.K. Birla. "Development of a Cyclic Strain Bioreactor for Mechanical Enhancement and Assessment of Bioengineered Myocardial Constructs." *Cardiovasc Eng Technol.* 6, no. 4 (2015): 533-45.

Zimmermann, W.H. "Biomechanical regulation of in vitro cardiogenesis for tissue-engineered heart repair." *Stem Cell Research & Therapy* 4, no. 137 (2013).

Industrial Bioengineering Activity

In this section a selection of peer-reviewed articles, which resulted from the contribution of the author to the activity of the Industrial Bioengineering group, are reported. This activities were carried out during the entire duration of the PhD program.

Role of the sinuses of Valsalva on the opening of the aortic valve

Giuseppe Pisani, MS,[a] Raffaele Scaffa, MD,[b] Ornella Ieropoli, PhD,[c] Edoardo M. Dell'Amico, MS,[c] Daniele Maselli, MD,[b] Umberto Morbiducci, PhD,[a] and Ruggero De Paulis, MD[b]

Objective: The present in vitro study was designed to ascertain whether the presence of sinuses of Valsalva in the aortic root were able to regulate the valve effective orifice area and modulate the gradient across the valve independently from root compliance.

Methods: Four different root configurations were prepared. Of the 4, 2 were silicon configurations with the same compliance, 1 with and 1 without sinuses of Valsalva, in which a 25-mm Solo stentless aortic valve was sutured inside. The other 2 configurations were obtained by substituting the upper part of the root with a straight Dacron graft or with a Valsalva graft in a remodeling fashion to reproduce the surgical situation. All roots were mounted in a pulse duplicator to measure the pressure decrease across the valve and effective orifice area at different cardiac outputs.

Results: With increasing cardiac output up to 7 L/min, an increase in the pressure decrease across the valve was evident in both configurations without sinuses of Valsalva (7.90 $\pm$ 1.7 and 11 mm Hg $\pm$ 0.1 mm Hg, respectively) but not in those with sinuses (2.87 $\pm$ 0.5 and 2.42 mm Hg $\pm$ 0.5 mm Hg). Similarly, with increasing cardiac output, the effective orifice area increased significantly only in the roots with sinuses (5.13 $\pm$ 0.5 and 5.47 $\pm$ 0.5 vs 3.06 $\pm$ 0.3 and 2.50 cm^2 $\pm$ 0.02 cm^2, respectively).

Conclusions: When the cardiac output is increased to greater than the resting physiologic values, the presence of sinuses of Valsalva, independently of root compliance, prevents an increase in the pressure decrease across the valve by way of an increase of the effective orifice area. (J Thorac Cardiovasc Surg 2013;145:999-1003)

ACD

The role played by the sinuses of Valsalva in regulating smooth and progressive closure of the aortic valve is well known. Vortex structures forming in the sinuses soon after systole has begun are of paramount importance in modulating the leaflet movements, ensuring synchronous, homogeneous, and stress-free leaflet closure. Little is known whether the sinuses might also be important in regulating valve opening and therefore in optimizing ventricular ejection. Our studies,[1] as well as those of other groups,[2] using echocardiography have shown that in the absence of sinuses of Valsalva, the aortic valve opening velocity was altered, implying that the presence of sinuses is also important during systole. Furthermore, the importance of root compliance in ensuring normal leaflet movements is also known. In the presence of a stiff root, the dynamic of the leaflets is altered and somehow mimics that seen in the absence of sinuses.[3] The present study was designed to ascertain the role played by sinuses of Valsalva in regulating aortic valve opening independently from the root compliance.

METHODS

Two molds of sintered resin with a diameter of 25 mm, 1 with and 1 without sinuses of Valsalva, were prepared. The maximum diameter at the sinuses was 35 mm. Two silicon roots were then obtained by dipping the 2 molds into a liquid silicon solution. Each immersion left a thin layer of silicon on the mold. Usually, 30 immersions were required to obtain a wall thickness of 1.3 mm $\pm$ 0.3 mm with compliance of 3% to 4%. The computation of the compliance of the silicon roots was conducted according to the Food and Drug Administration "Replacement Heart Valve Guidance."[4] A Stentless Solo (Sorin Biomedica, Saluggia, Italy), 25-mm pericardial valve was sutured inside each 1 of the 2 roots with a technique similar to the standard surgical technique using 4-0 polyester sutures and taking care to obtain perfect valve geometry and smooth pericardial tissue apposition with the silicon wall. Thus, 2 silicon configurations were obtained: silicon-straight and silicon-Valsalva. The final configuration showed a perfect fit between the valve and root (Figure 1). Another 2 roots with and without sinuses were then prepared in a similar manner and 2 other Solo valves were sutured inside. Next, the upper part of the silicon root was cut, following the crescent shape of the valve and replaced by suturing in its place a straight or Valsalva (Terumo Vascutek, Renfrewshire, UK) Dacron graft using the classic remodeling technique to reproduce the typical surgical situation. Two hybrid configurations were therefore obtained: hybrid-straight and hybrid-Valsalva (Figure 2). All testing of the 4 roots, 2 silicon and 2 hybrid, both with and without sinuses of Valsalva, was conducted using a Vivitro System pulse duplicator (Vivitro System, Victoria, British Columbia, Canada).[5] The 4 assembled models of aortic root and valve were installed in the aortic position of the pulse duplicator for the hydrodynamic test. A complementary (nontest) valve, the CarboMedics Prosthetic Heart Valve (29 mm; CarboMedics, Austin, Tex), was installed in the mitral position. The simulation conditions included 4 different cardiac output (CO) values (ie, 2, 3.5, 5, and 7 L/min) at a pulse rate of 70 beats/min and a mean aortic pressure of 100 mm Hg. The test fluid used was saline (density, 1000 kg/m^3; dynamic viscosity, 10^{-3} Pa/s). The 4 configurations were tested in different conditions. Hydrodynamic tests on the silicon-Valsalva and silicon-straight configurations were performed by

From the Department of Mechanics,[a] Politecnico di Torino, Turin, Italy; Department of Cardiac Surgery,[b] European Hospital, Rome, Italy; and Sorin Biomedica,[c] Saluggia, Italy.

Disclosures: Authors have nothing to disclose with regard to commercial support.
Received for publication Jan 9, 2012; revisions received Feb 5, 2012; accepted for publication March 20, 2012; available ahead of print April 16, 2012.

Address for reprints: Ruggero De Paulis, MD, Department of Cardiac Surgery, European Hospital, Via Portuense 700, Rome 00149, Italy (E-mail: depauli@tin.it).

0022-5223/$36.00

doi:10.1016/j.jtcvs.2012.03.060

Abbreviations and Acronyms
CO = cardiac output
EOA = effective orifice area

partially filling the housing aortic chamber with saline solution, mimicking the physiologic-like compliance of the construct. This experimental setting aimed at investigating the behavior of the valve in the presence of the Valsalva sinuses when aortic compliance is ensured. In contrast, the hybrid-Valsalva and hybrid-straight configurations were tested without forcing compliant behavior on the constructs (by filling with saline solution the housing aortic chamber). The rationale for this second setting was to investigate the behavior of the valve in the presence of differently shaped commercial grafts. A dedicated software control system was used to drive and control the mock circulatory system (ViviTest, ViVitro Systems). This allowed us to obtain and analyze the physiologic flow and pressure waveforms within the in vitro simulator. Technically, the analog aortic, ventricular, and mitral pressure signals were acquired using 3 pressure transducers (Utah Medical Products, Salt Lake City, Utah). The volumetric flow rates in the aortic and mitral positions were acquired using an electromagnetic flow meter system incorporating Carolina Medical probes (Carolina Medical Electronics, East Bend, NC). A sample rate of 500 Hz was considered appropriate. Analog signals were acquired using a 12-bit analog I/O resolution A/D board (KPCI-3101; Keithley Instruments, Cleveland, Ohio). The hydrodynamic performance of the assembled models of aortic root and valve was evaluated in terms of the aortic transvalvular pressure decrease and the effective orifice area (EOA), calculated using the well-established Gorlin formula, where Q is the volumetric aortic flow rate. Data are presented as the mean ± standard deviation, as obtained, for each simulated flow rate, from 3 independent experimental sessions.

RESULTS

The pressure decrease across the valve and EOA at each CO value is shown in Figure 3 and 4 for the silicon and hybrid configurations, respectively.

Pressure Decrease

In both silicon root configurations (Figure 3, *Left*), the pressure decreases across the valve were comparable at a CO of 2, 3.5, and 5 L/min (2.57 ± 0.41, 2.05 ± 0.50, and 2.10 mm Hg ± 0.60 mm Hg vs 1.32 ± 0.34, 1.51 ± 0.68, and 2.65 mm Hg ± 0.44 mm Hg, respectively). However, when the CO was increased to 7 L/min, the pressure decrease markedly increased in the silicon roots without sinuses (7.90 mm Hg ± 1.77 mm Hg) but not in the roots with sinuses (2.87 mm Hg ± 0.53 mm Hg). Similarly, in both hybrid root configurations (Figure 3, *Right*) the pressure decreases were comparable at 2, 3.5, and 5 L/min (1.20 ± 0.47, 1.26 ± 0.21, and 1.83 mm Hg ± 0.15 mm Hg vs 1.09 ± 0.03, 1.63 ± 0.12, and 4.16 mm Hg ± 0.37 mm Hg, respectively). Also, for the hybrid root configurations, when the CO was increased to 7 L/min, the pressure decrease remained low in the presence of sinuses (2.42 mm Hg ± 0.5 mm Hg) but markedly increased in the absence of sinuses (11 mm Hg ± 0.1 mm Hg).

Effective Orifice Area

Paralleling the results in pressure decrease, the EOA was comparable in all 4 root configurations at lower CO, but they were significantly larger at 7 L/min only in both configurations with sinuses (5.13 ± 0.5 and 5.47 ± 0.5 for the silicon and hybrid root, respectively; Figure 4).

DISCUSSION

The 3 anatomic pouches located immediately above the aortic valve were described in the 17th century by the Italian anatomist Antonio Maria Pini, who termed them the "Valsalva," from the location of his grandfather's family castle. Although from that day onward, they have always been termed the "sinuses of Valsalva," it was Leonardo da Vinci, who many years before had described, depicted, and explained in detail their shape and function. The greatness of Leonardo da Vinci in understanding the anatomy of the aortic valve has been celebrated by Robicsek[6] in a historical article. Recently, we have also reported how much Leonardo da Vinci had understood the modern concepts of the function of the aortic valve—from the generation of vortices and their importance in smooth valve closure, to the cusp's surface of coaptation, to a stunning description of leaflet histology.[7] In the modern era, the experiments of Bellhouse and Bellhouse[8] in the early 1970s methodically demonstrated the role of the sinuses in generating vortices to prevent the leaflet from affecting the aortic wall and in regulating aortic valve closure. All subsequent studies have always focused on the role played by the sinuses during the diastolic phase[9] and even more so after various types of valve-sparing procedures entered the surgical arena. In the past 10 years, a large number of studies have demonstrated the problem related to a lack of sinuses of Valsalva or, in contrast, the benefit of their reconstruction during surgery of the aortic root.[10,11] All studies, whether in vitro[12] or with the use of transesophageal echocardiography[1,2] or contrast phase magnetic resonance imaging,[13] have invariably shown the positive effect of the sinuses in regulating leaflet dynamics during the cardiac cycle and even in modulating coronary flow.[14] However, very little has been reported on the role played by the sinuses, if any, during systole. Because the sinuses are located on the aortic side, very similar to an extension of the aortic leaflet into the aortic wall, their role has always been considered almost exclusively in diastole. The function of the sinuses in systole has always been considered marginal, and most studies considered the cusp motion during the cardiac cycle, just as an increase in valve opening velocity is reported every time the aortic root is reconstructed in the absence of the sinuses.[1,2] In this experimental setting, we were able to show how the sinuses of Valsalva are also important in modulating the relative obstruction of flow present in the outflow tract of the left ventricle every time an increase in CO is present.

FIGURE 1. The 2 root configurations with *(left)* and without *(right)* sinuses created out of silicon with the same compliance. The conduit diameter was 25 mm and the stentless valve size was 25 mm in both cases. The maximum diameter at the sinuses was 35 mm.

This is secondary to an increase in the opening of the aortic valve area (Figure 5) that is possible only in the presence of the sinuses. Thus, the presence of sinuses of Valsalva appears to guarantee a progressive increase in the valve area and therefore an absence of gradient every time the CO is greatly increased such as during intense physical exertion. In the absence of sinuses, the aortic valve appears to be progressively more obstructive to flow when the CO increases. Although this aspect might not be clinically relevant, it is undoubtedly evident that under conditions of maximal effort the presence of the sinuses helps the heart to be more efficient and reduce energy losses. It is also generally accepted that the normal compliance of the root is extremely important in ensuring normal leaflet dynamics. Root expansion during systole is particularly important in the leaflet-free margins remaining distended and flat during their opening. In the absence of compliance, the leaflets have less space when traveling from their close to their full opening position, and, as a consequence, their free margin will show wrinkles and folds that might potentially contribute to an accelerated rate of failure. The progressive loss of elasticity in the aortic wall with advancing age, even more evident in patients with hypertension or atherosclerosis, is considered a cause that contributes to progressive leaflet degeneration resulting in valve stenosis.[15] Furthermore, because the leaflet movements inside a rigid and stiff root are somehow similar to those recorded in the absence of sinuses, it is evident how reconstructing an aortic root using nonelastic material such as Dacron and without providing neosinuses, might double the causes of suboptimal leaflet function. However, the data from the present study have shown that the presence of sinuses, independently of root compliance, is important in augmenting the aortic valve area and minimizing flow obstruction when the CO increases. When the CO was increased from 5 L/min to 7 L/min in the 2 study groups without sinuses, the mean gradient significantly increased and the EOA did not change or decreased slightly. In contrast, when the sinuses were present, and the CO was increased, the mean gradient did not change and the EOA progressively increased in both groups. This finding indicates that the presence of sinuses is important in modulating hemodynamics during systole. This information is important, in particular because it indicates that in patients who have undergone aortic root reconstruction, for whom root compliance is, by definition, markedly reduced or lost, the presence of the sinuses maintains normal systolic performance. This aspect gives more strength to our conclusion that the presence of sinuses of normal shape and dimensions might eventually compensate for the lack of root compliance. Combining the results of the present study with the known effects of the root compliance on leaflet movements and stress, it is likely that the presence of compliance is important for normal leaflet dynamics, in term of smooth leaflet movement and wrinkle-free cusp opening. Also, the presence of sinuses guarantees hemodynamic efficiency, even in the presence of increased CO. Although the clinical relevance of this finding might not be very important, because the maximum mean gradient at 7 L/min of CO was 8 mm Hg to 10 mm Hg, it helps in

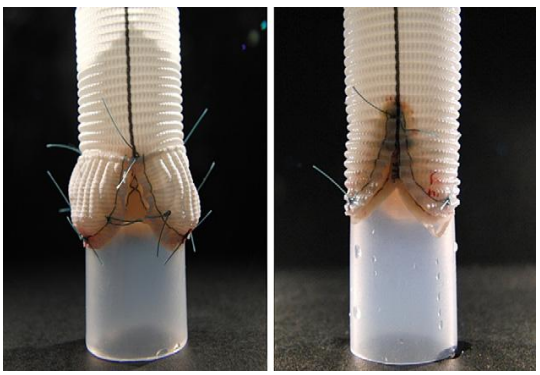

FIGURE 2. The 2 root hybrid configurations with *(left)* and without *(right)* sinuses created out of silicon in which the upper part was cut out following the valve contours and substituted with a straight graft or a Valsalva Dacron graft. Both conduit diameters were 26 mm.

ACD

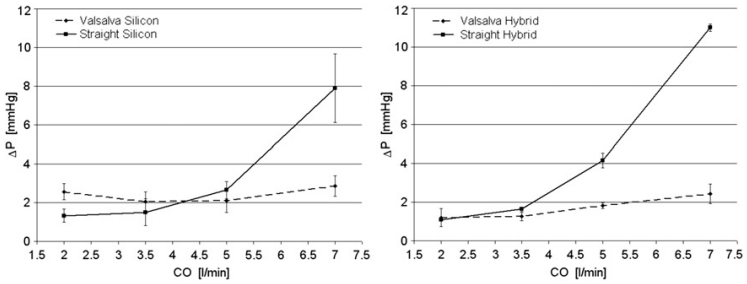

FIGURE 3. Diagram of pressure decrease across the valve in the Valsalva silicon and straight silicon configurations *(left)* and in the Valsalva-hybrid and straight-hybrid configurations *(right)*. When the cardiac output *(CO)* increased from 5 L/min to 7 L/min, an increase in the pressure decrease only occurred in the roots without sinuses. Note that no marked difference was present within each group with the same root configuration.

ACD

our understanding of how normal anatomy is functional to normal physiologic functions and another method by which the efficiency of the heart is maintained in conditions of an increased workload such as strenuous sport activity. In contrast to our findings, Sripathi and colleauges[16] with a numeric simulation using finite element analysis showed that the root compliance contributes to the ability of the normal valve to increase its EOA in response to increased physiologic demands. To obtain this finding, they had to apply a difference in pressure across the valve of 8 mm Hg before an increase in EOA became apparent. They concluded that such pressure was needed for obtaining backward leaflet bending against the root as the main contributor to the increase in EOA. However, by definition, finite element modeling uses static models and is usually used to measure stress. When more complex and dynamic condition are evaluated, such as when mimicking an increase in CO output, a fluid–structure interaction would be the minimum requirement to draw sound conclusions. Their experiment has simply demonstrated that by applying a greater pressure on its ventricular surface, the leaflet can bend backward and this is more evident in the presence of a compliant root. Therefore, the applied pressure is used as a surrogate for the gradient and the consequent deduction might not be accurate. Finally, the same simulation was not repeated in a straight root to rule out that it was the presence of sinuses that allowed a greater valve opening. In our experimental setting, the increase in pressure gradient generated by an increase in CO was inversely related to the EOA, just as in the actual clinical situation, and this was further confirmed by the direct recording of a larger anatomic area (Figure 5). In conclusion, although the root compliance is extremely important in the mechanism of valve opening through the well-known ''pull and release'' mechanism, and, again, it regulates the leaflets smooth opening by accommodating the excess of their free edge, it appears that the presence of sinuses plays an important and probably additive role in allowing a progressive increase in valve opening necessary to avoid an increase of gradient across the valve. Although it would require additional studies, this phenomenon could be explained by a progressive reduction of pressure inside the sinuses (induced by the vortices) by increased flow across the valve. This lower pressure beyond the leaflets explains how the leaflet can reach and maintain a wider opening area. In contrast, in the absence of sinuses and eddy currents, this mechanism cannot take place.

Study Limitations

Stentless pericardial valves were used for the present study; therefore, we could not determine whether the

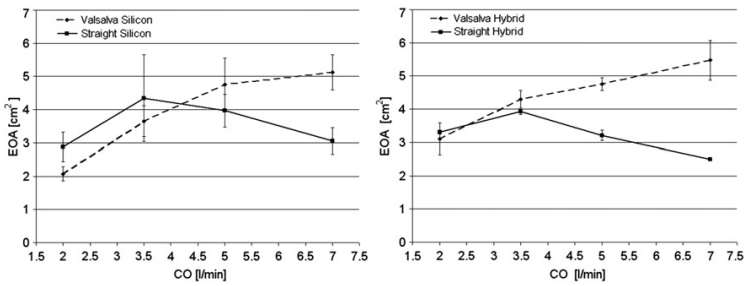

FIGURE 4. Diagram of effective orifice area *(EOA)* in the Valsalva-silicon and straight-silicon configurations *(left)* and in the Valsalva-hybrid and straight-hybrid configurations *(right)*. When the cardiac output *(CO)* increased from 5 to 7 L/min, an increase in the EOA was only present in the roots with sinuses. Note that no marked difference was present within each group with the same root configuration.

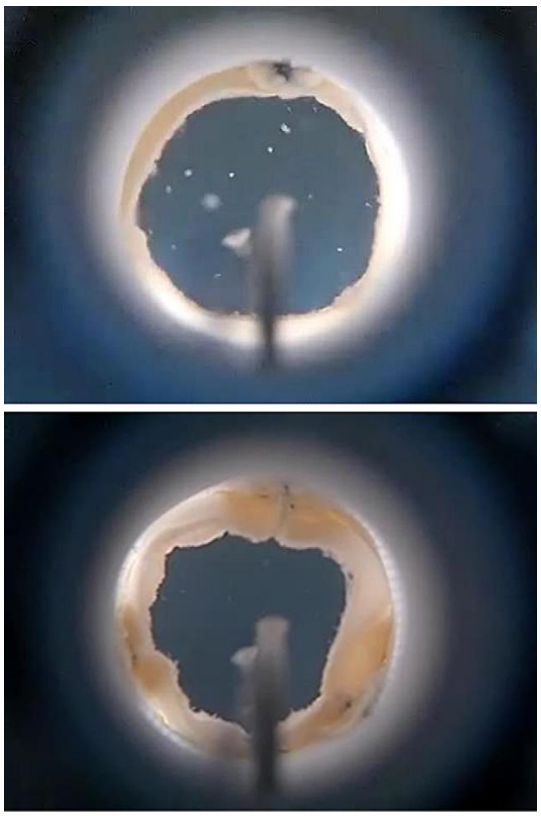

FIGURE 5. Direct visualization of valve operating condition inside a root with and without sinuses (hybrid configurations) at a cardiac output of 7 L/min. A larger opening area was evident in the valve inserted in a root with sinuses.

same findings would also apply to normal living valves. However, independently of the different manufacturing of pericardial valves that could influence better cusp movement, all pericardial valves have greater inertia than the natural living valve. Because the same valve type and size were used for all the experiments, we believe the valve material might have a small influence on the whole experiment and results. Similarly, the same experiment could have been performed using smaller valve sizes to verify whether the same results were also present at different diameters. However, because the roots were molded according to the valve size to a perfect fit, we would not have expected significant differences. Finally, because of the difficulties in constructing a hybrid configuration to a silicon-molded root using the reimplantation technique, we exclusively used the remodeling type of valve-sparing procedures. We therefore could not determine whether this finding would also apply to the reimplantation type of valve-sparing procedure in which stabilization of the annulus is present.

References

1. De Paulis R, de Matteis GM, Nardi P, Scaffa R, Bassano C, Chiariello L. Analysis of valve motion after the reimplantation type of valve-sparing procedure (David I) with a new aortic root conduit. *Ann Thorac Surg*. 2002;74:53-7.
2. Leyh RG, Schmidtke C, Sievers HH, Yacoub MH. Opening and closing characteristics of the aortic valve after different types of valve-preserving surgery. *Circulation*. 1999;100:2153-60.
3. Robicsek F, Thubrikar MJ. Are we implanting half valves? The role of sinus wall compliance in aortic valve function. *Ann Thorac Surg*. 1999;67:597.
4. Food and Drug Administration Replacement Heart Valve Guidance, version 4.1. October14, 1994.
5. Scotten LN, Walker DK, Dutton JW. Modified Gorlin equation for the diagnosis of mixed aortic valve pathology. *J Heart Valve Dis*. 2002;11:360-8.
6. Robicsek F. Leonardo da Vinci and the sinuses of Valsalva. *Ann Thorac Surg*. 1999;52:328-35.
7. Morea M, De Paulis R. "Il buso" (the orifice): how much did Leonardo know of the aortic valve? *J Cardiovasc Med*. 2007;8:399-403.
8. Bellhouse BJ, Bellhouse FH. Mechanism of closure of the aortic valve. *Nature*. 1968;217:86-7.
9. Thubrikar MJ, Nolan SP, Aouad J, Deck D. Stress sharing between the sinus and leaflets of canine aortic valve. *Ann Thorac Surg*. 1986;42:434-40.
10. Kunzelman KS, Grande KJ, David TE, Cochran RP, Verrier ED. Aortic root and valve relationships: impact on surgical repair. *J Thorac Cardiovasc Surg*. 1994; 107:162-70.
11. Miller DC. Valve-sparing aortic root replacement in patients with the Marfan syndrome. *J Thorac Cardiovasc Surg*. 2003;125:773-8.
12. Fries R, Graeter T, Aicher D, Reul H, Schmitz C, Böhm M, et al. In vitro comparison of aortic valve movement after valve-preserving aortic replacement. *J Thorac Cardiovasc Surg*. 2006;132:32-7.
13. Kvitting JPE, Ebbers T, Wigström L, Engvall J, Olin CL, Bolger AF. Flow patterns in the aortic root and the aorta studied with time-resolved, 3-dimensional, phase-contrast magnetic resonance imaging: implications for aortic valve-sparing surgery. *J Thorac Cardiovasc Surg*. 2004;127:1602-7.
14. De Paulis R, Tomai F, Bertoldo F, Ghini AS, Scaffa R, Nardi P, et al. Coronary flow characteristics after a Bentall procedure with and without sinuses of Valsalva. *Eur J Cardiothorac Surg*. 2004;26:66-72.
15. Robicsek F, Thubrikar MJ, Fokin AA. Cause of degenerative disease of the trileaflet aortic valve: review of subject and presentation of a new theory. *Ann Thorac Surg*. 2002;73:1346-54.
16. Sripathi VC, Kumar RK, Balakrishnan KR. Further insights into normal aortic valve function: role of a compliant aortic root on leaflet opening and valve orifice area. *Ann Thorac Surg*. 2004;77:844-51.

Research Highlight

Hemodynamics of the aortic valve and root: implications for surgery

Ruggero De Paulis, Andrea Salica, Giuseppe Pisani, Umberto Morbiducci, Luca Weltert, Daniele Maselli

Cardiac Surgery Department, European Hospital, Rome, Italy

Corresponding to: Ruggero De Paulis, MD. Cardiac Surgery, European Hospital, Via Portuense 700, 00149 Rome, Italy. Email: depauli@tin.it.

Submitted Oct 20, 2012. Accepted for publication Nov 30, 2012.
doi: 10.3978/j.issn.2225-319X.2012.11.16
Scan to your mobile device or view this article at: http://www.annalscts.com/comment/view/1398/

The aortic valve divides the left ventricular outflow tract (LVOT) from the ascending aorta and its normal or abnormal function has a great impact on regulating physiological hemodynamic parameters. It is well known that the presence of aortic valve stenosis or insufficiency results in impaired hemodynamics with direct and dire consequences on the left ventricle. On the other hand, when normal, the valve and the root have long been perceived as a type of passive gate dividing the left ventricle from the ascending aorta and preventing any reversal of flow, with minimal effect on valve hemodynamics. However, two points need to be stressed. First, the aortic valve has to be considered a complex unit along with the other components of the aortic root, the sinuses and the sino-tubular (ST) junction (1). Second, the particular shape of the aortic root, with its narrowing at the ST junction and the direct continuity of the sinus wall with the valve leaflets, makes perfect control of the closing mechanism of the aortic cusps possible. It is well known that the vortices forming inside the sinuses due to the narrowing of the ST junction are of paramount importance in regulating the closing mechanism of the valve leaflets (2). Although Leonardo da Vinci understood and illustrated these vortices long ago (3,4), only quite recently has the sophisticated relationship among the various components of the aortic root in controlling valve motion been demonstrated experimentally (5). During isovolumetric contraction of the left ventricle, pressure is transmitted through the inter-leaflet triangle up to the commissure in such a way that the valve starts to open even before forward flow has started. Next, as soon as the blood exits the ventricle, the regions of flow closer to the wall, being slower, curl down into the sinuses and already start closing the aortic valve. The main result of all these complex mechanisms is to keep the stress on the valve leaflet to a minimum (1), allowing a life-long valve durability.

Although almost everything with regard to the diastolic function of the aortic root is known, much less is clear about its systolic function or about the possibility that the aortic root, with its particular shape, might also regulate the opening of the aortic valve (6). This year our group was able to shed some light on the role of the aortic root in regulating the systolic function of the aortic valve (7). More specifically, we were able to show, for the first time, that the shape of the root, namely the presence of the sinuses, coupled with the pulsatility of the flow, was important in guaranteeing complete opening of the valve and thereby absence of a trans-valvular gradient. In this respect, root compliance seemed to be less important.

These *in-vitro* experiments were conducted by first creating two silicon roots with the same compliance, either with or without sinuses, containing the same biological stentless valve sutured inside following the remodeling technique (*Figure 1*, with permission). The two samples were then tested with simulated circulation to measure the pressure drop across the value, therefore calculating the effective orifice area at different cardiac outputs. The main finding of this simple experiment was that when the cardiac output was increased above 5 L/min the pressure drop significantly increased in the sample without sinuses of Valsalva. The results were identical when the portion of the aorta above the valve (the root) was replaced with either a straight Dacron graft (no sinuses) or with a Valsalva Dacron graft (with sinuses) (*Figure 2*, with permission): the pressure drop increased only in the sample without sinuses. This last finding appears to rule out compliance in having a role in modulating pressure drops across the valve. In fact, it was the shape, more than the compliance, which was responsible

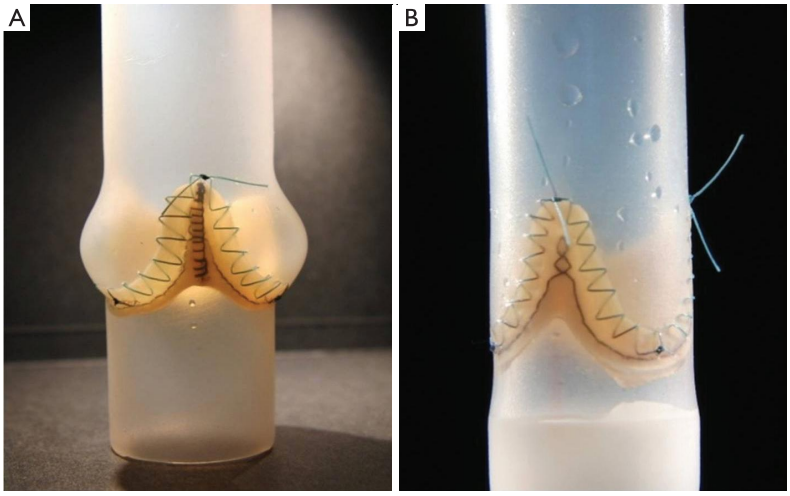

Figure 1 The two root silicon models with the same compliance, but either with or without sinuses. A stentless valve was sutured inside following the remodeling techniques. (Reprinted from J Thorac Cardiovasc Surg, Elsevier, with permission)

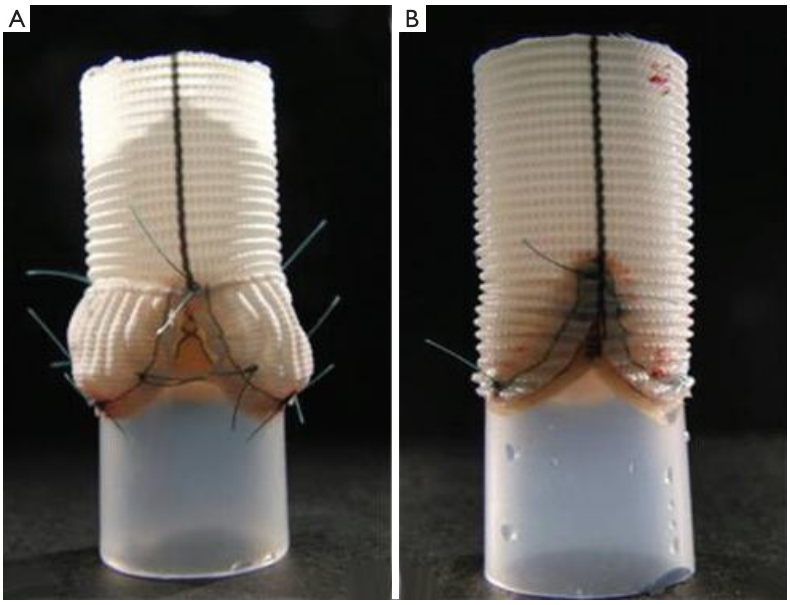

Figure 2 The silicon models where the upper part was substituted with a straight or a Valsalva Dacron graft to minimize the role played by root compliance. (Reprinted from J Thorac Cardiovasc Surg, Elsevier, with permission)

for the different findings (*Figure 3*, with permission). It was evident that in the presence of sinuses the valve was able to reach its full opening position; if the sinuses were absent complete opening was prevented.

To further elucidate this aspect and to find a reasonable explanation for this different behavior, a second series of experiments was planned (8). In this series we aimed to ascertain if the pulsatility of flow played a role in generating

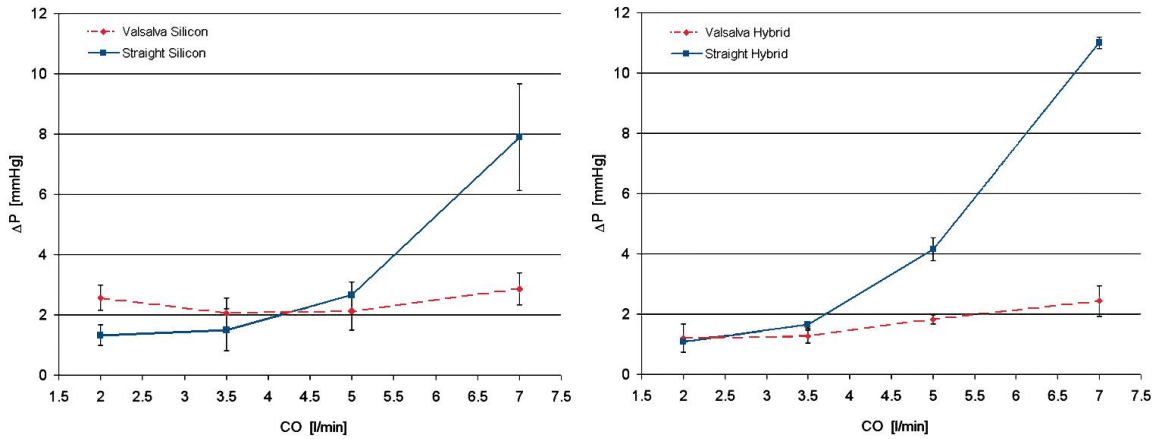

Figure 3 Pressure drop across the valve in both roots, with and without sinuses, either made out of silicon (standard compliance) or made out of Dacron (minimized compliance). Note that independent of root compliance, the absence of sinuses increased the pressure drop across the valve. (Reprinted from J Thorac Cardiovasc Surg, Elsevier, with permission)

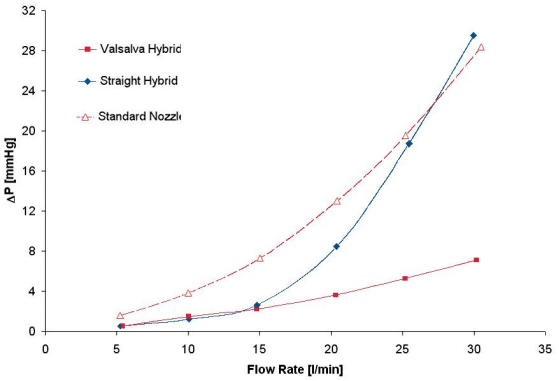

Figure 4 Pressure drop across the valve in both Dacron roots, with and without sinuses, compared with a standard nozzle. Note that when steady flow becomes turbulent (i.e., around 15 L/min) the presence of sinuses helps to maintain a low pressure drop across the valve

fluid dynamics that could explain the differences in terms of the aortic valve pressure drop between the two different root configurations. We hypothesized that the interaction between the particular characteristics of pulsatile flow and the sinuses of Valsalva could be responsible for the superior hydrodynamic performance of the aortic valve.

The same two Dacron roots and valve models were prepared as described above: one with and one without sinuses (*Figure 2*, with permission). The hydrodynamic performance of the two assembled models was investigated in pulsatile and in laminar steady state flow regimes by using two dedicated test benches. Pressure drop and effective orifice area were measured at different flow rates. During the laminar steady state flow regime, it was evident that the hydrodynamic performance of the aortic valve was not markedly affected by the presence or absence of the sinuses.

Interestingly, from a comparison of the hydrodynamic test performed using a standard reference nozzle, in steady state flow regime, no difference was found in terms of pressure drop, either in the presence or absence of the sinuses, up to a cardiac output of 15 L/min (*Figure 4*). This observation shows the absence of any interaction between aortic root geometry and low-turbulence steady state flow regimes on hydrodynamic performance of the aortic valve. On the contrary, as shown in the previous study, the results acquired in pulsatile flow regimes showed significantly different behavior between the two root models. This implies that only in the presence of pulsatile flow do the sinuses of Valsalva play a role in modulating the pressure drop across the valve.

More specifically, when comparing the results of the two aortic root configurations operating under different flow regimes, it can be seen that the hydrodynamic performance of the aortic valve is markedly affected by the presence of pulsatile flow conditions. In this setting it appears that the interaction between aortic root geometry and pulsatile flow influences the opening of the aortic valve. Pulsatile flow is, by definition, turbulent flow; it is therefore likely that in the straight graft model and in the presence of pulsatile flow, the turbulence acts as a functional obstruction preventing complete opening of the aortic leaflets. On the contrary, in

presence of appropriate space and architecture (represented by the sinuses of Valsalva), aortic leaflets are free to achieve complete valve opening with low-pressure drops, even in the presence of turbulent flow. This phenomenon could possibly be caused by the systolic vortices forming above the aortic valve. These vortices find a natural home in the sinuses expansion, which has an immediate effect both on the location and on the size of the vena contracta. The importance of flow turbulence in determining the effects described above was further confirmed by the finding that in steady conditions, when the flow was increased above 15 L/min (when it starts to become turbulent) (*Figure 4*) the same pressure drop across the valve started to build, but now in the absence of sinuses.

In conclusion, this series of experiments demonstrated that in the presence of turbulent flow (i.e., pulsatile flow), the particular shape of the aortic root and its sinuses are important in regulating proper opening of the aortic valve. In the absence of sinuses the turbulence of flow causes suboptimal opening of the valve with the consequent presence of a pressure drop and reduced effective orifice area.

How this finding might have implications for surgical technique is less clear. Although various techniques that do not provide sinuses reconstruction have proved to be equally effective in term of satisfactory valve function (9), it is already well established that in the absence of sinuses the valve closing mechanisms are impaired and reduced valve durability is to be expected (10). The observation that the presence of sinuses is also important in regulating valve opening, especially evident at higher cardiac output, contributes to the notion that in active, young and sportive patients the surgeon should strive to achieve an anatomical reconstruction of the aortic root.

Acknowledgements

Disclosure: The authors declare no conflict of interest.

Cite this article as: De Paulis R, Salica A, Pisani G, Morbiducci U, Weltert L, Maselli D. Hemodynamics of the aortic valve and root: implications for surgery. Ann Cardiothorac Surg 2013;2(1):40-43. DOI: 10.3978/j.issn.2225-319X.2012.11.16

References

1. Thubrikar MJ, Nolan SP, Aouad J, et al. Stress sharing between the sinus and leaflets of canine aortic valve. Ann Thorac Surg 1986;42:434-40.
2. De Paulis R, De Matteis GM, Nardi P, et al. Opening and closing characteristics of the aortic valve after valve-sparing procedures using a new aortic root conduit. Ann Thorac Surg 2001;72:487-94.
3. Robicsek F. Leonardo da Vinci and the sinuses of Valsalva. Ann Thorac Surg 1991;52:328-35.
4. Morea M, De Paulis R. 'Il buso. (the orifice). How much did Leonardo know of the aortic valve? J Cardiovasc Med (Hagerstown) 2007;8:399-403.
5. Bellhouse BJ, Bellhouse FH. Mechanism of closure of the aortic valve. Nature 1968;217:86-7.
6. Higashidate M, Tamiya K, Beppu T, et al. Regulation of the aortic valve opening. In vivo dynamic measurement of aortic valve orifice area. J Thorac Cardiovasc Surg 1995;110:496-503.
7. Pisani G, Scaffa R, Ieropoli O, et al. Role of the sinuses of Valsalva on the opening of the aortic valve. J Thorac Cardiovasc Surg 2012. [Epub ahead of print].
8. Salica A, Pisani G, Ieropoli O, et al. Straight versus Valsalva graft: importance of pulsatility and eddy currents during systole. An in vitro study. Eur J Cardio-Thor Surg 2012. [Epub ahead of print].
9. David TE, Feindel CM. An aortic valve-sparing operation for patients with aortic incompetence and aneurysm of the ascending aorta. J Thorac Cardiovasc Surg 1992;103:617-21; discussion 622.
10. Grande-Allen KJ, Cochran RP, Reinhall PG, et al. Re-creation of sinuses is important for sparing the aortic valve: a finite element study. J Thorac Cardiovasc Surg 2000;119:753-63.

European Journal of Cardio-Thoracic Surgery Advance Access published September 10, 2015

European Journal of Cardio-Thoracic Surgery (2015) 1–6
doi:10.1093/ejcts/ezv311

ORIGINAL ARTICLE

EXPERIMENTAL

Cite this article as: Salica A, Pisani G, Morbiducci U, Scaffa R, Massai D, Audenino A *et al*. The combined role of sinuses of Valsalva and flow pulsatility improves energy loss of the aortic valve. Eur J Cardiothorac Surg 2015; doi:10.1093/ejcts/ezv311.

The combined role of sinuses of Valsalva and flow pulsatility improves energy loss of the aortic valve

Andrea Salica[a], Giuseppe Pisani[b], Umberto Morbiducci[b], Raffaele Scaffa[a], Diana Massai[b], Alberto Audenino[b], Luca Weltert[a], Lorenzo Guerrieri Wolf[a] and Ruggero De Paulis[a,*]

[a] Division of Cardiac Surgery, European Hospital, Rome, Italy
[b] Department of Mechanical and Aerospace Engineering, Politecnico di Torino, Turin, Italy

* Corresponding author. Division of Cardiac Surgery, European Hospital, via Portuense, 700, 00149 Rome, Italy. Tel: +39-0665975224; fax: +39-0665975112; e-mail: depauli@tin.it (R. De Paulis).

Received 21 April 2015; received in revised form 16 July 2015; accepted 20 July 2015

Abstract

OBJECTIVES: Normal aortic valve opening and closing movement is a complex mechanism mainly regulated by the blood flow characteristics and the cyclic modifications of the aortic root. Our previous *in vitro* observations demonstrated that the presence of the Valsalva sinuses, independently from root compliance, is important in reducing systolic pressure drop across the aortic valve. This *in vitro* study was designed to ascertain if this effect is dependent on the flow characteristics.

METHODS: Stentless 21, 23 and 25 mm aortic prostheses were sutured inside Dacron graft with and without sinuses. Hydrodynamic performance of the root models was investigated in steady-state (continuous) and unsteady-state (pulsatile) flow regimes. Aortic transvalvular pressure drop and effective orifice area (EOA) were evaluated.

RESULTS: The continuous flow analysis revealed that no marked differences in pressure drop characterized the two root configurations at flow regimes lower than 15 l/min, independently of valve size. Conversely, at higher flow regimes (up to 30 l/min) a relatively low pressure drop continued to characterize grafts with sinuses, whereas marked increments in pressure drop were measured in straight grafts, especially in the smaller size (77.05 ± 4.58 vs 23.80 ± 2.44 mmHg; 18.40 ± 1.31 vs 7.66 ± 0.37 mmHg and 29.54 ± 0.17 vs 7.12 ± 0.07 mmHg, for 21, 23 and 25 mm valve, respectively). Under pulsatile conditions, the presence of sinuses clearly confirmed lower pressure drops also more evident in the smaller valve sizes (53.89 ± 1.06 vs 11.6 ± 0.24 mmHg at 7 l/min for 21 mm valve). EOA values were always lower in the absence of sinuses. In continuous flow regimes, at 30 l/min EOA of 25 mm valve size was 3.67 ± 0.02 cm^2 in the Valsalva model versus 1.79 ± 0.01 cm^2 for the Straight model. In pulsatile tests, at 7 l/min a 25-valve size demonstrated an EOA of 5.47 ± 0.60 in the Valsalva model versus 2.50 ± 0.02 cm^2 in the Straight model.

CONCLUSIONS: These findings (i) confirm the hypothesis that the sinuses of Valsalva play a key role in optimizing the aortic haemodynamics during systole, minimizing energy losses; (ii) suggest that the sinuses of Valsalva are needed because of the complex nature of blood flow during ejection.

Keywords: Sinuses of Valsalva • Aortic valve • Valve-sparing • Dacron graft • Haemodynamics

INTRODUCTION

The aortic root is a well-defined anatomical unit, which has been proved to play a major role in reducing stress on aortic valve cusps and in optimizing ejection to warrant haemodynamic efficiency without structural deterioration of the aortic leaflets throughout life [1, 2]. In recent years, several studies have attempted to clarify the synergistic role that blood flow and the surrounding structures, as the sinuses of Valsalva, have in the opening and closing movements of the aortic leaflets, and a complex interaction has been demonstrated [3–5]. In this regard, while a lot of evidence suggests the paramount importance of the interaction between vortices and sinuses of Valsalva in modulating leaflet movements at closure [6, 7], little is known whether sinuses are also important in the hydrodynamic performance of the aortic valve during the ejection phase of the cardiac cycle. In a very recent *in vitro* study [8], we investigated the impact that the sinuses of Valsalva have in regulating aortic valve opening during the cardiac output (CO), and our main finding was that, independently from the root compliance, the presence of sinuses of Valsalva was important in minimizing the systolic pressure drop across the aortic valve, highlighting the importance of the root geometry.

Here, we extend the study with the purpose of ascertaining if the observed role played by the sinuses of Valsalva on transvalvular

gradient and energy losses could be dependent on the interaction between root geometry and flow properties.

The results from this basic study, designed to probe deeper into the role of the sinuses of Valsalva, could also contribute to the debate on surgical techniques to be applied for disease treatment involving the aortic root. In the last decade for the treatment of aortic root aneurysms, valve-sparing procedures, remodelling and reimplantation have been preferred, whenever possible, over the classic Bentall procedure [9–12]. Advantages of the two main valve-sparing techniques, remodelling [10, 11] and reimplantation [12], have been largely studied. Although the remodelling technique demonstrated a close to normal aortic valve movement [13, 14], recreation of a sinus-like space is still a matter of controversy. In particular, for the reimplantation technique, different surgical options have been suggested to create some sort of pseudo-sinuses, which are recognized to be important not only for proper valve motion, but also for decreasing diastolic leaflet stress [15]. To this extent, a stentless aortic valve prosthesis was used to reproduce as much closer as possible the anatomical features that could be present in the aortic valve-sparing operation, with the use of a Straight or a Valsalva Dacron graft. An *in vitro*, fully controlled study on the impact that the presence of the sinuses could have on leaflet dynamics could then contribute to animate the debate.

MATERIALS AND METHODS

Study design

Three groups of aortic root and valve of different sizes, 21, 23 and 25 mm, were prepared. Each group was composed of two different root configurations, one with and one without sinuses of Valsalva, for a total of six models.

Experiments were conducted in continuous and pulsatile flow regimes by using two dedicated test benches. For the hydrodynamic performance under a continuous flow regime, aortic valve pressure drop of each assembled model was measured over a flow rate range of 5–30 l/min, 5 l/min increments (according to the requirements of the ISO 5840 and FDA Guidelines [16] for prosthetic valve testing). Five independent experimental sessions were conducted for each flow rate and for each valve size. Under pulsatile flow regime, the hydrodynamic performance of the assembled models was evaluated at four different flow regimes, i.e. 2, 3.5, 5 and 7 l/min of CO, at the pulse rate of 70 bpm, at the mean aortic pressure of 100 mmHg and a 35% systole/cycle ratio. The same saline solution (density, 1000 kg/m^3; dynamic viscosity 10^{-3} Pa s) was used as test fluid in all the tests. The hydrodynamic performance of the assembled models of aortic root and valve was evaluated in terms of aortic transvalvular pressure drop (Δp). Similarly to the continuous flow regime, five independent experimental sessions were conducted for each simulated flow rate and for each valve size. Effective orifice area (EOA) was also calculated in both continuous and pulsatile flow conditions, using the well-established Gorlin formula.

Molds preparation

Two different root configurations were prepared as described in a previous study [8]. Briefly, two molds of sintered resin, one with and one without sinuses of Valsalva of three different sizes (diameters 21, 23 and 25 mm) were fabricated to obtain a total of six models. Six silicon roots were prepared by multiple dipping of the molds into a liquid silicon solution until a wall thickness of about 1.3 mm was obtained. Three pericardial valves (Stentless Freedom Solo, Sorin Biomedica, Saluggia, Italy) of size 21, 23 and 25 mm were sutured inside silicon roots by 4/0 polyester running suture. Two root configurations, called Straight and Valsalva, were then obtained as follows: the upper part of each silicon root was cut following the crescent shape of the valve and replaced by suturing in its place a straight or a Valsalva™ Dacron graft of the corresponding diameter (Terumo Vascutek, Renfrewshire, UK) (Fig. 1).

Hydrodynamic experimental set-up

As reported by Yoganathan *et al.* [17], steady flow (continuous) studies can be helpful to characterize energy losses of prosthetic valves, especially at the flow phase corresponding to peak systole, where it has been demonstrated that quasi-stationary flow conditions might be assumed [18]. However, as such analyses neglect the effects of pulsatility, a more physiological unsteady-state (pulsatile) characterization is needed.

The hydrodynamic performance under continuous flow regime was investigated using a dedicated test bench, in accordance with

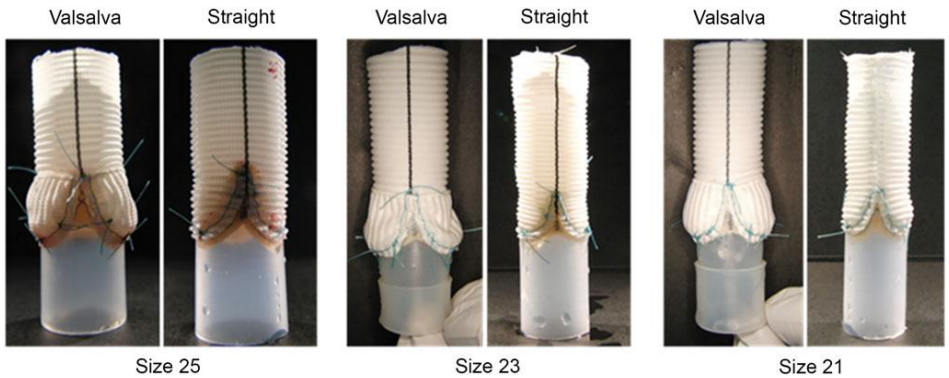

Figure 1: Experimental root configurations for valve size 25, 23 and 21 mm.

the requirements of the ISO 5840:2005 and FDA Guidelines [16] for prosthetic valve testing. The test bench consists of a centrifugal pump forcing the test fluid motion, two hydraulic resistances for regulating the flow and a sample chamber, where the configurations are housed, hold between two hydraulic tubes used as flow straightener in order to minimize flow disturbance. Two pressure sensor catheters and their dedicated acquisition boxes (Millar, MP-500) are used to measure pressure drop in valves, while a magnetic flowmeter allows for flow rate monitoring.

The hydrodynamic performances under pulsatile flow regimen were investigated, using a Vivitro System, Inc. (Victoria, Canada) mock loop. An exhaustive description of the test bench can be found in our previous study [8]. Briefly, the assembled models of aortic root and valve were installed in aortic position of the mock loop, using a complementary valve (Carbomedics CPHV, 29 mm; CarboMedics, Austin, TX, USA) in the mitral position. A dedicated software control system (ViviTest, ViVitro systems, Inc.) was used for obtaining, acquiring and analysing physiological flow and pressure waveforms within the *in vitro* simulator. More in detail, volumetric flow rates in aortic and mitral position were acquired using an electromagnetic flow meter (Carolina Medical Electronics, Inc., East Band, NC, USA) and aortic, ventricular and mitral pressure signals were acquired, using three pressure transducers (Utah Medical Products, Salt Lake City, Utah). Direct visualization of valve operating condition was performed, using an ultrafast speed camera (Casio Exlim Ex F1), mounted on top of the Vivitro system [19, 20]. The camera records 512 × 384 pixel images at a frequency of 300 frames per second.

Statistical methods

A Welch *t*-test for repeated measures was used to evaluate differences in pressure drop between the two root configurations during pulsatile or continuous flow. Data are presented as mean ± standard deviation. A *P*-value <0.05 was considered significant.

RESULTS

The continuous flow analysis highlighted that at flow regimes of 5, 10 and 15 l/min (i) no marked difference between the two root configurations can be observed and (ii) low pressure drop was maintained, independent of valve size (Fig 2). Conversely, differences between the two root configurations were more evident (Fig. 2) in the flow rate range of 20–30 l/min. Particularly, low pressure drop characterized the Valsalva graft configuration, independent of the valve size, whereas high pressure drops were measured in the presence of Straight roots. In detail, lower values were evidenced for the Valsalva grafts with 25 mm (up to 7.12 ± 0.07 mmHg) and 23 mm valve (up to 7.66 ± 0.37 mmHg) compared with the Straight configurations (29.54 ± 0.17 and 18.40 ± 1.31 mmHg at 30 l/min, respectively). This difference was clearly more evident in the 21 mm valve size where the pressure drop reached 77.05 ± 4.58 mmHg at 30 l/min in the Straight configuration whereas it was 23.80 ± 2.44 mmHg at 30 l/min in the Valsalva configuration.

Under pulsatile flow (Fig. 3), differences between the two root configurations were present during all tests, in particular for the smaller valve size. At a flow rate between 2 and 3, 5 l/min pressure drops were similar for both root configurations, being moderately lower in the Valsalva root models. At higher flow regimes (5 and 7 l/min), the differences become clearly evident (Fig. 3). In particular, in the smaller valve size, this difference was remarkable both at 5 l/min (27.4 ± 2.6 vs 4.5 ± 0.3 mmHg) and at 7 l/min (53.89 ± 1.06 vs 11.6 ± 0.24 mmHg) (Fig. 3).

EOA values (Table 1) were always lower in the absence of sinuses in both continuous and pulsatile flow tests. Conversely, the presence of the sinuses was functional in maintaining the EOA to

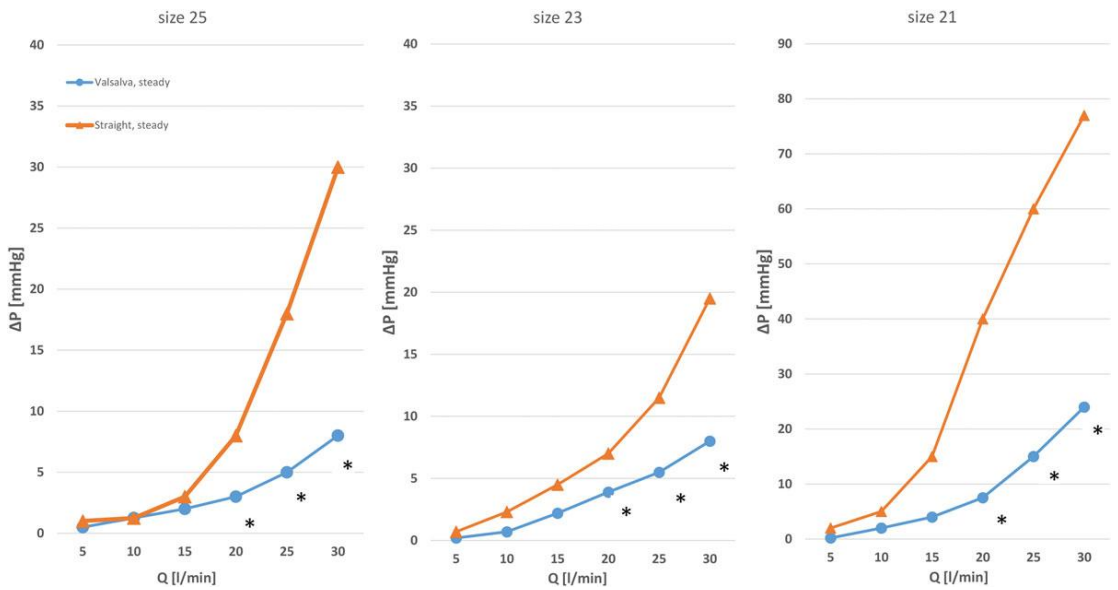

Figure 2: Pressure drops (Δ*p*, mmHg) as measured in the two aortic root configurations for the three valve size in continuous flow regimes at different cardiac outputs. *$P < 0.001$.

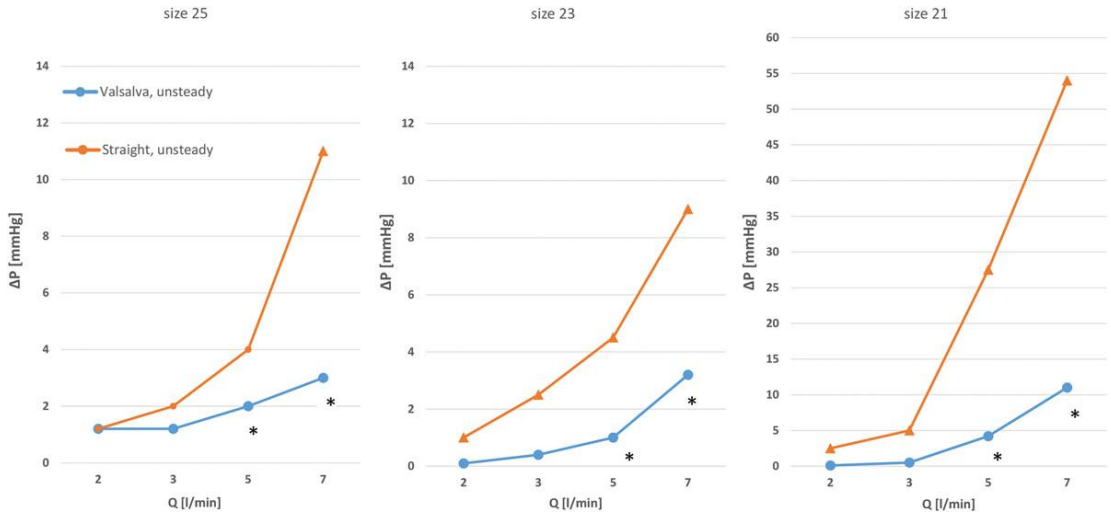

Figure 3: Pressure drops (Δp, mmHg) as measured in the two aortic root configurations for the three valve size in pulsatile flow regimes at different cardiac outputs. *$P < 0.001$.

Table 1: The EOAs (cm^2) as measured in the two aortic root configurations for the three valve sizes, 21, 23 and 25 mm, in continuous and pulsatile flow regime at different cardiac outputs

	EOA at pulsatile flow regimes				EOA at continuous flow regimes					
	2 l/min	3.5 l/min	5 l/min	7 l/min	5 l/min	10 l/min	15 l/min	20 l/min	25 l/min	30 l/min
Valve size 25										
Valsalva	3.30 ± 0.47	4.30 ± 0.27	4.76 ± 0.19	5.47 ± 0.60	2.53 ± 0.16	2.73 ± 0.06	3.23 ± 0.03	3.43 ± 0.02	3.55 ± 0.02	3.67 ± 0.02
Straight	3.11 ± 0.05	3.93 ± 0.08	3.21 ± 0.01	2.50 ± 0.02	1.75 ± 0.07	2.61 ± 0.03	2.82 ± 0.04	2.25 ± 0.01	1.90 ± 0.01	1.79 ± 0.01
Valve size 23										
Valsalva	1.78 ± 0.24	1.81 ± 0.03	2.02 ± 0.04	2.51 ± 0.01	2.96 ± 0.47	3.10 ± 0.10	3.22 ± 0.10	3.38 ± 0.12	3.44 ± 0.10	3.53 ± 0.08
Straight	1.67 ± 0.07	1.78 ± 0.01	1.91 ± 0.03	1.89 ± 0.03	1.98 ± 0.45	2.31 ± 0.34	2.38 ± 0.26	2.38 ± 0.09	2.43 ± 0.01	2.28 ± 0.09
Valve size 21										
Valsalva	1.20 ± 0.01	1.60 ± 0.03	1.77 ± 0.02	1.70 ± 0.02	2.33 ± 0.35	2.52 ± 0.14	2.54 ± 0.07	2.50 ± 0.05	2.11 ± 0.03	2.02 ± 0.11
Straight	1.31 ± 0.03	1.44 ± 0.03	0.98 ± 0.03	0.97 ± 0.00	1.35 ± 0.15	1.60 ± 0.07	1.37 ± 0.18	1.03 ± 0.01	1.06 ± 0.01	1.11 ± 0.04

Data are expressed as mean ± standard deviation.
EOA: effective orifice area.

significantly higher values. Notably, in continuous flow regimes, beyond 15 l/min when a 25 mm valve size was considered, the EOA was almost double when the sinuses were present (3.67 ± 0.02 vs 1.79 ± 0.01 cm^2 at 30 l/min).

Similarly, in pulsatile tests, when a 25 mm valve was considered, an increase up to 119% at 7 l/min was evident with respect to the Straight configuration (5.47 ± 0.60 vs 2.50 ± 0.02 cm^2) (Table 1).

The visualization of valve's operating condition inside a root with and without sinuses under pulsatile flow regime is presented in Fig. 4. In detail, visualizations refer to peak systole, i.e. when the valve is expected to be fully open, at a flow regime of 7 l/min. By visual inspection the presence of a larger opening area for all valve sizes inserted in a root with sinuses is evident. Snapshots in Fig. 4 qualitatively confirm the quantitative findings of Table 1. Interestingly enough, at 7 l/min of pulsatile flow the Valsalva configuration with a 23 mm valve exhibits an EOA value which is very close to a 25 mm valve into a Straight root configuration (2.51 ± 0.01 vs 2.50 ± 0.02 cm^2).

DISCUSSION

Normal aortic valve opening and closing movement is a complex mechanism mainly regulated by the blood flow and the cyclic modifications of the aortic root [21, 22]. Since 1970, the role of fluid structures (vortices) above the aortic valve in regulating closing movements of the aortic leaflets has been well documented [6, 7]. In fact, forward blood flow completely opens the aortic leaflets and, at the same time, curls down into the sinuses of Valsalva. In this manner, the vortices inside the sinuses prepare the leaflets to a smooth closure once the blood flow reverses in diastole [2, 7, 21].

Importance of sinuses of Valsalva in regulating aortic valve function has been evidenced even in surgical studies. Leyh *et al.*, comparing remodelling and reimplantation techniques with straight Dacron graft, concluded that the remodelling technique preserving the shape and the mobility of the sinuses of Valsalva achieves a near-normal opening and closing characteristics of the aortic valve

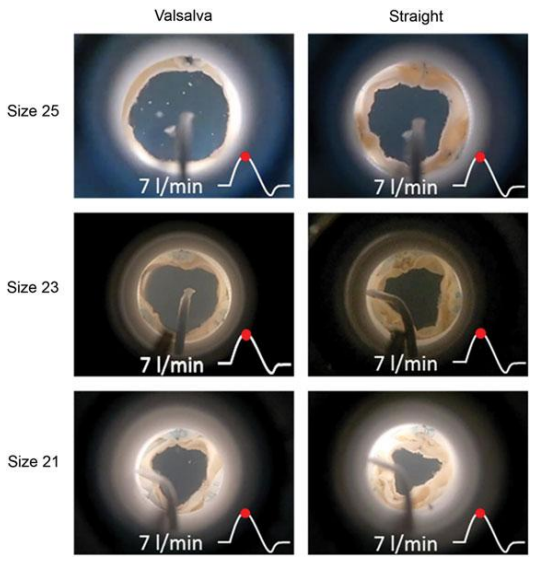

Figure 4: Direct visualization of valves operating condition at peak systole inside the two aortic root configurations for valve size 25, 23 and 21 mm at 7 l/min under pulsatile flow regime.

[13]. Kvitting, using magnetic resonance imaging, observed the absence of physiological vortices in patients undergoing aortic root replacement without reconstruction of sinuses. The authors concluded that this phenomenon might explain some of the changes in aortic valve motion that have been observed in patients undergoing valve-sparing surgery without reconstruction of sinuses [5]. Grande-Allen in a finite element study investigated the diastolic function of the sinuses of Valsalva and concluded that valve-sparing techniques that recreate the potential for space formation of sinuses bring leaflet stresses closer to normal [15]. In summary, the importance of the sinuses of Valsalva has been considered to achieve smooth opening and closing movements of the aortic valve.

Even if little has been reported about the role played by the sinuses of Valsalva in terms of haemodynamic performance of the aortic valve during the ejection phase of the systole, an increase in valve opening velocity has been reported every time the aortic root is reconstructed in the absence of sinuses [13, 23]. Recently, in a study *in vitro* that compared Straight and Valsalva root models, we demonstrated that when the CO raised above resting physiological values, the presence of the sinuses of Valsalva, independent of the root compliance, does prevent an increase of systolic pressure drop across the aortic valve, assuring a better hydrodynamic performance [8].

In the present study, we aimed at clarifying the interaction of the sinuses of Valsalva with the fluid structures of the flow field, which convinced that this interaction could explain the differences in terms of aortic valve pressure drop and consequent energy losses between the two root configurations evidenced in the previous study [8].

During the pulsatile flow experiment, the hydrodynamic performance of the aortic valve was positively influenced by the presence of the sinuses of Valsalva. In particular, this evidence was enhanced by both increasing the flow rates and reducing the valve size (e.g. 53 vs 11 mmHg, Straight vs Valsalva).

Interestingly, during continuous flow regimes, at flow rates of 20–25 and 30 l/min, marked differences in terms of pressure drop were observed. Paralleling the results in the pulsatile flow setting, the presence of sinuses of Valsalva maintained a significantly lower pressure drop every time the flow increased or the valve size was reduced (e.g. 23.8 ± 2.4 vs 77.05 ± 4.5 mmHg at 30 l/min for the 21 valve size). On the contrary, at flow rates of 5–10 and 15 l/min, hydrodynamic performance of the valve was not affected by the presence or the absence of the sinuses.

This observation suggests that although continuous flow presents different characteristics with respect to the pulsatile flow regimes, high flow rates (20–30 l/min) generate a fluid dynamics, similarly to the pulsatile flow, that impacts on aortic valve opening. In this setting, it could be interesting to evidence a similitude between the two different types of flow. Pulsatile flow regime is composed of many crescent and de-crescent flow velocities, for example, peak systolic velocity at 5 l/min during pulsatile flow regime rises up to an equivalent velocity during continuous flow of about 28 l/min, and at 7 l/min velocity of flow rises up to an equivalent continuous flow of about 37 l/min. Therefore, although 30 l/min are absolutely not a physiological flow rate, peak systolic velocity of a pulsatile flow at a physiological flow of 5–7 l/min rises up to 30 or more litres per minutes. Our interest in steady flow tests was in fact to magnify and better understand the interaction between flow field and root geometry at the peak systolic velocity of a physiological pulsatile flow regime.

Comparing the results of the two aortic root configurations operating at the two flow regimes, it can be observed that the hydrodynamic performance of the aortic valve is markedly affected by the onset of instabilities in the flow field as normally induced by pulsatile flow condition or by high flow rates in the continuous flow regimes [17]. This phenomenon is amplified for small size valves, in consequence of the extension of flow separation regions downstream of the valve, characterizing their flow field. In these conditions, the presence of sinuses appears to mitigate the action of these flow instability in generating the so-called vena contracta effect that creates a functional flow obstruction as evidenced from the pressure drop results.

The comparison of EOA between the two root configurations confirmed the evidence as visualized in Fig. 4. The EOA of the Straight root model was invariably smaller than the EOA of the Valsalva root, during the pulsatile flow tests.

Our results suggest that flow separation regions generated by the flow act as a functional obstruction in the absence of sinuses of Valsalva reducing (i) the complete opening of the aortic leaflets and (ii) the lumen available to forward flow, resulting in a pressure drop across the aortic valve that increases with the CO. On the contrary, in the presence of appropriate space and architecture (represented by sinuses of Valsalva), aortic leaflets are free to complete valve opening with low pressure drops, even when CO rises up to high flow rates. This phenomenon could possibly be caused by the flow recirculation regions (vortices) forming above the aortic valve. These vortices find a natural housing in the expansion of sinuses, which has an immediate effect both on the location and on the size of the vena contracta, and in more space available for leaflet expansion. Even if this hypothesis needs further investigation, its plausibility is supported by basic fluid mechanics.

Some limitations could weaken the finding of this study. In particular, Dacron grafts were sized on the corresponding valve prosthesis diameter, whereas in the clinical practice more complex formulas have been suggested, and the diameter is often larger than that of the effective valve orifice. In detail, in a large series of

reimplantation and remodelling techniques, graft sizes of 31 ± 4 and 28 ± 4 mm, respectively, were used [24, 25]. This is because, in surgical practice, some sort of pseudo-sinuses might be present independently from the type of graft, straight or 'Valsalva', that is, eventually used. On the other hand, the aim of these experiments is to improve the knowledge on the role of sinuses-like space in the haemodynamic of the aortic valve independently from the type of graft or the type of technique that is utilized. This work should therefore be seen as a step towards a better comprehension of the pathophysiology of the aortic complex more than an improvement of our approach to valve-sparing surgery.

Another limitation could be found in the fact that abnormal aortic roots and pericardial valves were used in the present study (i.e. Dacron grafts are stiff and not compliant). In this sense, the *in vitro* models proposed here do not mimic in all aspects the physiological changes of the natural aortic root (i.e. the opening of the sinotubular junction or the contraction of the ventriculo-arterial junction during systole). Moreover, pericardial aortic prostheses have a greater inertia than the natural aortic valves, and saline solution and flow regimes used in these experiments might have different characteristics than the normal human physiology. We could not determine whether the same findings in terms of absolute pressure drop values would also apply to the normal roots, but the results of these experiments show that the presence of a sinus-like space above the aortic leaflets interacts with the flow field, improving the hydrodynamic performance of the aortic valve. Furthermore, despite consistent different findings in pressure drop between the straight and the Valsalva configuration for each size, we unexpectedly found a better absolute performance of the 23 mm when compared with the 25 mm. Although this is definitely not important for the aim of our study, it is possible that a cusp of a 25 mm valve had higher inertia of the corresponding 23 mm valve. Finally, the use of a saline solution of a determined viscosity might not be totally assimilated to blood. However, it is generally accepted for *in vitro* studies to be conducted using a crystalloid solution.

In conclusion, the present study demonstrated the primary role played by the sinuses of Valsalva in optimizing the aortic haemodynamics and in minimizing the loss of energy. Sinus-like space promotes an instrumental interaction between the aortic leaflets opening and the flow instabilities present in the flow field. Finally, it suggests that the surgical reconstruction of the sinuses of Valsalva is instrumental in achieving the physiological hydrodynamic fluid–structure interaction between the aortic leaflets and the peculiar characteristics of the pulsatile flow.

Conflict of interest: As the inventor of the Valsalva graft, Dr. De Paulis receives royalties from Vascutek Terumo. No fundings were received to complete this study.

REFERENCES

[1] Thubrikar MJ, Bosher LP, Nolan SP. The mechanism of opening of the aortic valve. J Thorac Cardiovasc Surg 1979;77:863–70.
[2] Thubrikar MU, Nolan SP, Aoud J, Deck JD. Stress sharing between the sinuses and leaflets of canine aortic valve. Ann Thorac Surg 1986;42:434–40.
[3] De Hart J, Peters GWM, Shreurs PJG, Baaijens FTP. A three-dimensional computational analysis of fluid-structure interaction in the aortic valve. J Biomech 2003;36:103–12.
[4] Morbiducci U, Ponzini R, Rizzo G, Cadioli M, Esposito A, Montevecchi FM *et al.* Mechanistic insight into the physiological relevance of helical blood flow in the human aorta. An in vivo study. Biomech Model Mechanobiol 2011;10:339–55.
[5] Kvitting JPE, Ebbers T, Wingström L, Engvall J, Olin CL, Bolger AF. Flow patterns in the aortic root and the aorta studied with time-resolved, 3-dimensional, phase contrast magnetic resonance imaging: implication for aortic valve-sparing surgery. J Thorac Cardiovasc Surg 2004;127:1602–7.
[6] Bellhouse BJ, Bellhouse FH, Reid KG. Fluid mechanics of the aortic root with application to coronary flow. Nature 1968;219:1059–61.
[7] Bellhouse BJ, Bellhouse FH. Mechanism of closure of the aortic valve. Nature 1968;217:86–7.
[8] Pisani G, Scaffa R, Ieropoli O, Dell'Amico EM, Maselli D, Morbiducci U *et al.* Role of the sinuses of Valsalva on the opening of the aortic valve. J Thorac Cardiovasc Surg 2013;145:999–1003.
[9] Bentall HH, De Bono A. A technique for complete replacement of the ascending aorta. Thorax 1968;23:338–9.
[10] Yacoub MH, Fagan A, Stassano P, Radley-Smith R. Results of valve conserving operation for aortic regurgitation. Circulation 1983;68:III–321.
[11] Sarsam MA, Yacoub MH. Remodeling of the aortic valve annulus. J Thorac Cardiovasc Surg 1993;105:435–8.
[12] David TE, Feindel M. An aortic valve-sparing operation for patients with aortic incompetence and aneurysm of the ascending aorta. J Thorac Cardiovasc Surg 1992;103:617–22.
[13] Leyh RG, Schmidtke C, Sievers HH, Yacoub MH. Opening and closing characteristics of the aortic valve after different types of valve preserving surgery. Circulation 1999;100:2153–60.
[14] De Paulis R, De Matteis GM, Nardi P, Scaffa R, Buratta MM, Chiariello L. Opening and closing characteristics of the aortic valve after valve-sparing procedures using a new aortic root conduit. Ann Thorac Surg 2001;72:487–94.
[15] Grande-Allen KJ, Cochran RP, Reinhall PG, Kunzelmann KS. Re-creation of sinuses is important for sparing the aortic valve: a finite element study. J Thorac Cardiovasc Surg 2000;119:753–63.
[16] Po-Chien L, Jia-shing L, Baoshu I, Shawyan L, Jia W, Hwang NHC. On accelerated fatigue testing of prosthetic aortic valve. Frontiers in Biomedical Engineering. Topics in Biomedical Engineering International Book Series 2003;185–96.
[17] Yoganathan AP, Cape EG, Sung HW, Williams FP, Jimoh A. Review of hydrodynamic principles for the cardiologist: applications to the study of blood flow and jets by imaging techniques. JACC 1988;12:1344–53.
[18] Yellin EL, Peskin CS. Large amplitude pulsatile water flow across an orifice. J Dyn Sys Meas Control 1975;97:92–5.
[19] Redaelli A, Bothorel H, Votta E, Soncini M, Morbiducci U, Del Gaudio C *et al.* 3-D Simulation of the St. Jude medical bileaflet valve opening process: fluid-structure interaction study and experimental validation. J Heart Valve Dis 2004;13:804–13.
[20] Nobili M, Morbiducci U, Ponzini R, Del Gaudio C, Balducci A, Grigioni M *et al.* Numerical simulation of the dynamics of a bileaflet prosthetic heart valve using a fluid–structure interaction approach. J Biomech 2008;41:2539–50.
[21] Thubricar MJ, Heckman JL, Nolan SP. High speed cine-radiographic study of aortic valve leaflet motion. J Heart Valve Dis 1993;26:653–61.
[22] Higashidate M, Tamiya K, Beppu T, Imai Y. Regulation of the aortic valve opening. J Thorac Cardiovasc Surg 1995;110:496–503.
[23] De Paulis R, De Matteis GM, Nardi P, Scaffa R, Bassano C, Chiariello L. Analysis of valve motion after the reimplantation type of valve-sparing procedure (David I) with a new aortic root conduit. Ann Thorac Surg 2002;74:53–7.
[24] Morishita K, Murakami G, Koshino T, Fukada J, Fujisawa Y, Mawatari T *et al.* Aortic Root remodeling operation: how do we tailor a tube graft? Ann Thorac Surg 2002;73:1117–21.
[25] David TE, Feindel CM, David CM, Manlhiot C. A quarter of a century of experience with aortic valve-sparing operations. J Thorac Cardiovasc Surg 2014;148:872–80.